Detection of Gust Fronts Using the Doppler Velocity Derived Divergence Product

A Thesis Presented to the Faculty of the Graduate School at the University of Missouri

In Partial Fulfillment of the Requirements for the Degree of Masters of Science

by

RUSSELL J. CLEMINS

Dr. Neil Fox, Thesis Advisor

July 2018

The undersigned, appointed by the dean of the Graduate School, have examined the thesis entitled

Detection of Gust Fronts Using the Doppler Velocity Derived Divergence Product

Presented by Russell J. Clemins,

A candidate for the degree of master of science,

And hereby certify that, in their opinion, it is worthy of acceptance.

Associate Professor Neil Fox

Professor Patrick Market

Associate Professor Athanasios Micheas

Assistant Research Professor Jeffrey Wood

Acknowledgements

I would like to thank the professors of the Soil Environmental and Atmospheric Sciences (SEAS) for their teaching and guidance over the course of my two years in graduate school. I would like to thank my graduate advisor Dr. Neil Fox, as well as Dr. Patrick Market, Dr. Athanasios Micheas, and Dr. Jeffrey Wood for their positions on my thesis committee, and for their comments and input on this research. Next, I would like to thank Dr. Micheal Simpson, for his assistance with operating WDSS-II, without his help this research would likely still be struggling to work through radar data processing. I would like to thank Dr. John Sadler from the United States Department of Agriculture – Agricultural Research Service, for his permission to use data from the Centralia eddy-covariance sites during this research, as well as for his support with any questions I had with the sites. I would also like to thank Dr. Jeffrey Wood, and in turn AmeriFlux, for their permission to use data from the MOFLUX Missouri Ozarks Site.

I would also like to thank the NASA NSPIRES program, and Dr. Neil Fox for their roles in providing the funding for this research project. Without their assistance completing this research and master's degree would not have been possible.

Table of Contents

List of Tables

List of Figures

Abstract

Identifying gust fronts can be essential for situational awareness when developing nowcasts during convective events. In addition to bearing potentially damaging winds, gust fronts also act as forcing mechanisms; influencing storm initiation, development, and propagation. Using doppler radar, gust fronts are usually observed by the presence of a reflectivity thin line ahead of the parent storm. In the situation where a thin line is not visible on radar, there is a loss of situational awareness. This study aimed to determine if gust fronts can be observed through the doppler velocity derived divergence product by isolating contiguous areas of divergence (convergence) that form couplets or line features, relative to the leading edge or ahead of a storm. Radar data for the study was collected using the University of Missouri – Columbia's MZZU X-Band radar, as well as the WSR-88D from the NWS Saint Louis CFO. Data processing was performed through the Warning Decision Support System –Integrated Information (WDSS-II), and the data was analyzed using the MatLab software. Thresholds for minimum pixel area, as well as minimum and maximum divergence (convergence) were used to establish a range of interest. Data was then filtered through a process of dilation and erosion, to prune out noise and highlight larger features. Through multiple cases using MZZU and KLSX, suitable criteria were developed that allowed the identification of Div-Conv couplets and linear regions of convergence that suggest the presence of gust fronts. Eddy covariance towers near Columbia, MO were used for surface observations of vertical velocity (w) and

Turbulence Kinetic Energy (TKE). Good agreement was found between increases in w and TKE when gust fronts were detected and propagating through the region.

Chapter 1: Introduction

In unstable environments storms can appear seemingly out of nowhere. The rapid development of storms in these sensitive conditions receives forcing from mechanisms below the synoptic-scale flow. One group of sub-synoptic forcing mechanisms is convergence lines, the storm generated type of which is known as a Gust Front (or Outflow Boundary). Gust fronts are boundaries formed by the cold descending air from thunderstorms, propagating outward and displacing the environmental air (AMS glossary, 2018). The convergence of storm outflow and the environmental air generates upward motion along the boundary, which can lead to the development of new storms or intensification of existing convection. In addition to their influence on storm development and initiation gust fronts have also been attributed as a factor to storm motion, as well as potential source of damaging winds. Gaining an awareness of environmental conditions, forcing mechanisms, and hazards can make the difference for developing a successful nowcast.

Operational forecasters gain situational awareness by using the multitude of remote sensing instruments at their disposal to gather data of their forecast area. Weather radars can also be used to detect gust fronts. This is done by the radar analyzing the motion of scanned hydrometeors and other scatterers in the environment. The United States National Weather Service (NWS) utilizes an array of WSR-88D radars across 122 Weather Forecast Offices (WFOs) to monitor weather conditions, from calm

sunny days to the most intense severe weather. Expanding the tools for operators in situ for use to detect gust fronts and the potential influences they bring will enhance the ability for forecasters to protect life and property.

1.1 Statement of Thesis

For this study, WSR-88D and the MZZU Radar data will be used to study gust fronts in a collection of cases to determine if the features can be consistently observed and tracked over time using derived radar divergence products. The aim is to develop an additional method for the tracking of these features. This additional tool can be used to increase situational awareness in nowcasting of thunderstorm initiation, development, and movement during convective events. Gust fronts from thunderstorm outflow are a form of convergent wind phenomena related to convergence lines. These features can be identified with a couplet of convergence and divergence or a linear convergence signature. To detect the gust fronts, the study will use the Doppler velocity derived convergence (divergence) product. In addition, radar reflectivity will be used to give spatial context for the suspected fronts relative to their parent storm, and vertical velocity data from eddy covariance towers will act as a ground truth when suspected fronts pass over them.

The objectives of this study are:

- To determine if the derived divergence product can be used to detect and observe gust fronts.

- Determine if the signatures of suspected gust fronts can be correlated with vertical velocity data from eddy covariance towers that features pass over.
- Determine the parameters (settings) that generate the gust front signatures.

Chapter Two: Literature Review

To accomplish the goal of this research project, an analysis of studies with similar objectives was performed. No previous studies involving the experimental use of the derived divergence product in the study of gust fronts exist, given the purpose of this current study. The literature review will analyze other topics related to radar and gust fronts that can be of use in this study. Section one is an overview of gust fronts, consisting of the current definition, common characteristics, and discussion of vertical structure. Section two discusses techniques used in doppler radar observation of gust fronts, as well as the role of gust fronts in nowcasting. Section three will discuss sources of error and uncertainty expected in this study.

2.1 Overview of Gust Fronts

2.1.1 Overview– Defining Gust Fronts

The definition of a gust front has been rather variable across multiple studies since the 1940s. Multiple components of the thunderstorm outflow have been examined and determined to be a part of what defines a gust front in nature. The most recent definition, as seen in Wakimoto (1982) and the AMS glossary state: a gust front is "the leading edge of a mesoscale pressure dome followed by a surge of gusty winds on or near the ground. A gust front is often associated with a pressure jump, a temperature drop, and or heavy precipitation" (Wakimoto, 1982; AMS Glossary, 2018).

Gust fronts have been referred to in previous studies as the “cold-air dome”, “pseudo-cold front”, and “gravity current” (Charba, 1974; Goff 1976; Weaver and Nelson, 1982). These terms refer to the interaction of airmasses that come from the thunderstorm outflow at the leading edge or out ahead a head of the storm’s precipitation. Interactions such as the sharp shifts in wind direction and speed, along with a pressure rise and drop in temperature, similar to the passage of a cold front. However, Goff (1976) reports that “there appear to be important differences among these phenomena in terms of scale, life cycle, intensity, and forcing mechanisms” (Goff 1976). Between gust fronts and cold fronts, cold fronts are much larger both in spatial and temporal scale due to being synoptic scale features. In contrast, gust fronts are on the mesoscale. Their size, intensity, and lifecycle are dependent on the parent thunderstorm from which the boundary originates.

2.1.2 Overview – Common Characteristics of Gust Fronts

Gust fronts share a few common physical characteristics that have been documented in studies such as Goff (1976), Klingle et al. (1987); and Wakimoto (1982). The typical height of a gust front is around 2 km above the surface, with maximum heights able to reach up to 4 km, and minimum heights observed as low as 300 meters (Klingle et al., 1987; Wakimoto,1982). Klingle et al. (1987) reported on the variability of gust front length. Noting that length of the front is the length of the line pattern (signature) observed through doppler radar that could be identified as a gust front

(Klingle et al., 1987). Where lengths can range from only a few to hundreds of kilometers. Gust fronts feature a region of high turbulence behind the frontal boundary, which has often been a danger for aviation operations (Hwang et al., 2017).

2.1.3 Overview-Gust Front Vertical Structure

The vertical structure of gust fronts was first studied in-depth by Charba (1974) and was later expanded on by Goff (1976) and Wakimoto (1982). These studies aimed to map out the components within gust fronts in three-dimensional space. Charba (1974) and Goff (1976) accomplished this by using a combination of the National Severe Storms Laboratory (NSSL) sensor network and with large meteorological instrument towers to observe the lowest 500m, while Wakimoto (1982) used the NIMROD system and rawinsonde data to extend to the entire vertical scope.

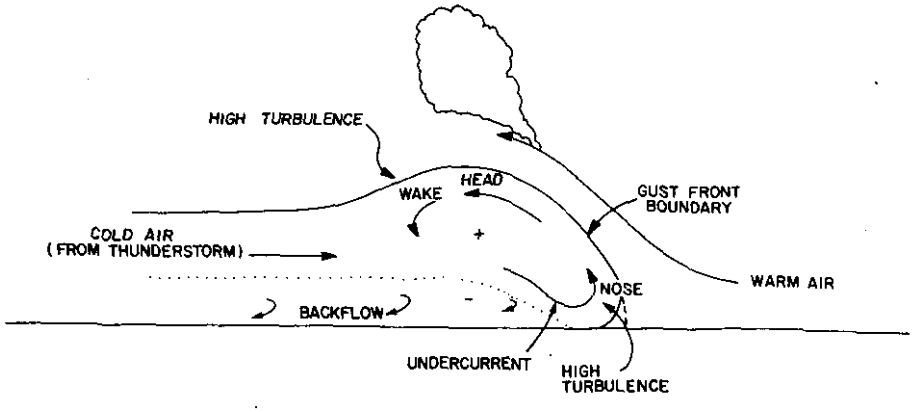

Figure 2.1: Schematic diagram of a gust front's vertical adapted from Charba (1974). Reproduced from Goff (1976).

Goff (1976) presented a schematic model of the common vertical structure of a gust front, derived from the schematic seen in Charba (1974). This schematic can be seen in Figure 2.1. The model of a gust front's leading-edge features includes: the nose and head of the front, undercurrent, backflow, wake, and the pre-frontal updraft. The nose of the gust front is the leading edge of the outflow which extends towards the warm air and rolls back into the parent storm (Charba, 1974; Goff, 1976). The nose acts as the lifting surface as the warmer air is displaced by the colder outflow air within the gust front. The head is the main body of the leading edge, at its back is the wake (Charba, 1974; Klingle et al., 1987). Charba (1974) found that while the nose of the gust front is the lifting surface, it is supported by the direct thermal circulation within the head. The wake at the back of the head is the downward component of the direct circulation and is a source of turbulent mixing and high wind gustiness within the region behind the boundary (Charba, 1974; Klingle et al., 1987). The Undercurrent refers to the high speed low-level flow in the cold air just behind the front (Charba, 1974; Goff, 1976). The backflow is the drag-induced, surface layer flow away from the front (Goff, 1976). Last, the prefrontal updraft, or gust front updraft, is the region at and ahead of the front where the environmental air is displaced through vertical motion. The frontal updraft is the result of the interaction of the nose and circulation within the head with the warmer environmental air. Vertical motion is highest within the frontal updraft as the interaction of airmasses allows for parcels to be lifted and more easily reach their level of free convection (Goff, 1976). Goff (1976) also notes that within the core of the updraft vertical velocity commonly exceeds 1 m s^{-1}.

The vertical structure of a gust front contains variations depending on the stage of the outflow's life cycle. The slope of the gust front is variable based on the stage of evolution: the steepest slopes occur during the mature stage, shallow slopes are seen during formative and dissipating-transforming stages (Goff, 1976) (Fig 2.2). Other structural features display unique variations based on the stage of the outflow, such as the structure of the nose. The nose of the front first appears in the formative stage close to the ground and little backflow is present. In contrast, the mature stage features a well-defined backflow, and the front is bent backwards below the nose. During the late-mature and dissipating stages of a gust front's life cycle the gust front continues to become shallower over time due to its continued spreading out ahead of the parent thunderstorm (Goff, 1976).

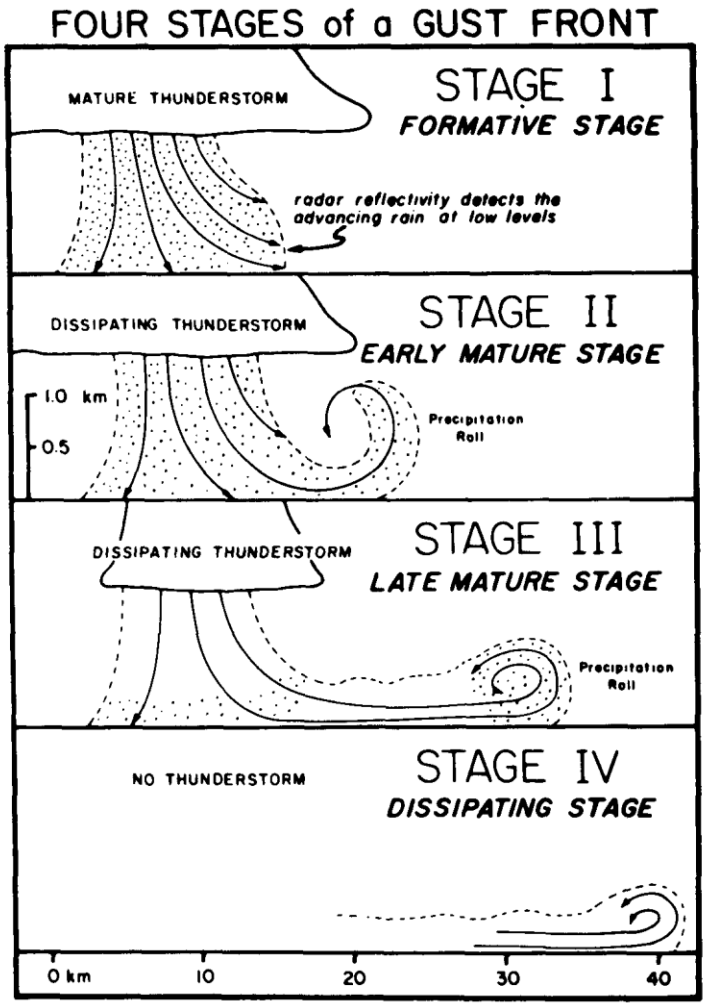

Figure 2.2: The four stages of a gust front lifecycle. Reproduced from Klingle et al (1987).

As previously mentioned, Wakimoto (1982) further expanded on the vertical structure and life cycle of gust fronts by moving beyond the limits of Charba (1974) and Goff (1976) using doppler radar, the NIMROD network, and rawinsonde data. Wakimoto (1982) did not make any major additions to the vertical structure of gust fronts seen in the schematic developed by Charba (1974) and adapted by Goff (1976) despite realizing the structure and life cycle in observation (Fig 2.3). However,

Wakimoto (1982) found that during the middle stages of the gust front's life cycle (mature, and late-mature), a precipitation roll could be observed as a gust front moves farther away from the thunderstorm and some precipitation is carried by the circulation within the head of the gust front.

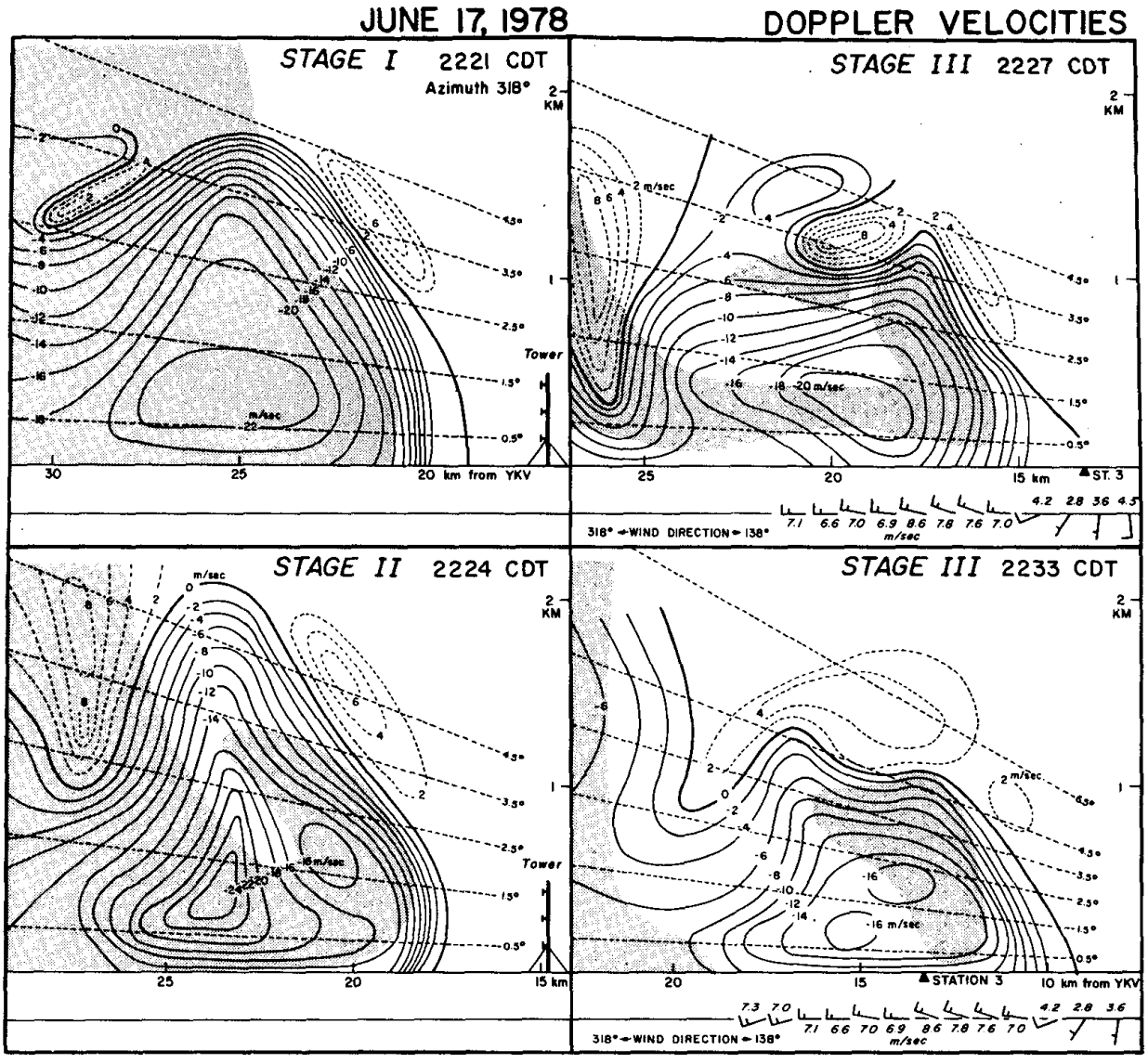

Figure 2.3: Observed structure of the stages of a gust front lifecycle using rawinsonde and Doppler velocity data from June 17, 1978. Reproduced from Wakimoto (1982).

2.2 Radar Detection and Nowcasting

2.2.1 Radar Detection of Gust Fronts

Doppler radars have been instrumental in the observation of gust fronts, with three methods that have been previously explored to observe these features. The most common method of radar detection is using reflectivity to identify a "thin-line" of enhanced reflectivity in the clear air (Fig 2.4). Reflectivity values for the thin line associated with out-of-storm gust fronts range from around 5-30 dBZ (Hwang et al., 2017; Klingle et al, 1987; Wilson and Mueller 1993), with a mean reflectivity value of 9-10 dBZ (Hwang et al., 2017). The thin line is produced when the gust front has moved out ahead of the parent thunderstorm and has suspended scatterers within the leading updraft and or turbulent region. These scattering particles have commonly been attributed to insects (Wilson and Mueller, 1993; Wilson et al., 1994), or displaced hydrometers such as those found within a precipitation roll (Wakimoto, 1982). It is possible for gust fronts to never separate from the parent thunderstorm and not produce a reflectivity thin line, as seen in Klingle et al. (1987) (Fig 2.5). An "in storm" gust front can be detected using two more radar products, Doppler velocity and Doppler spectrum width.

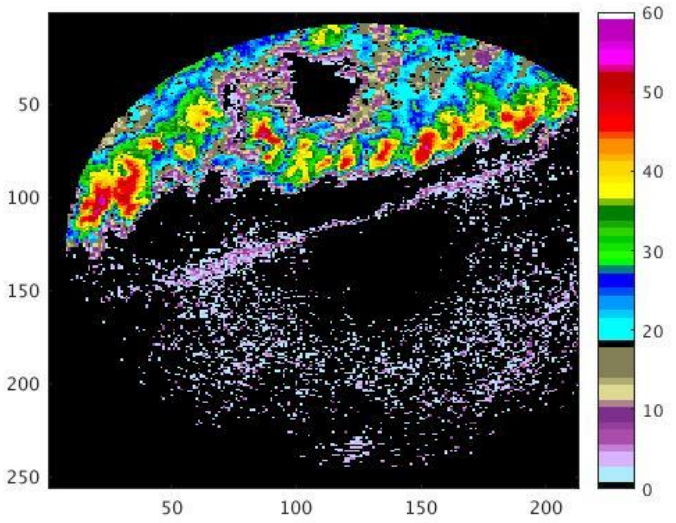

Figure 2.4: Example of a gust front on reflectivity, identified by a "thin-line" ahead of the storms. Radar imagery from 2017 03 01 (KLSX).

The Doppler velocity product is used to observe the motion of scattering particles across multiple radar scans. The signals on doppler velocity identify the direction particles are moving towards and away from the radar. Convergence lines and gust fronts can be identified by the presence of a linear pattern of convergence (radial shear) (Klingle et al., 1987; Schreiber, 1986; Wilson and Mueller, 1982). Klingle et al. (1987) explains this by giving an example: if a gust front is oriented perpendicular to the radar beam, regions within the outflow will display a strong inward component on velocity. Where also, the environmental winds have a general outbound component observed on radar. Moving from the radar across the environmental air into the outflow air there is a steep gradient in doppler velocity as the gust front is encountered, marking the site of radial convergence (Klingle et al., 1987; Wilson et al 1980) (Fig 2.5). Since Doppler velocity can observe these motions within the precipitation of a

thunderstorm and in clear air, it is regarded as a more reliable method for observing gust fronts than reflectivity (Klingle et al., 1987).

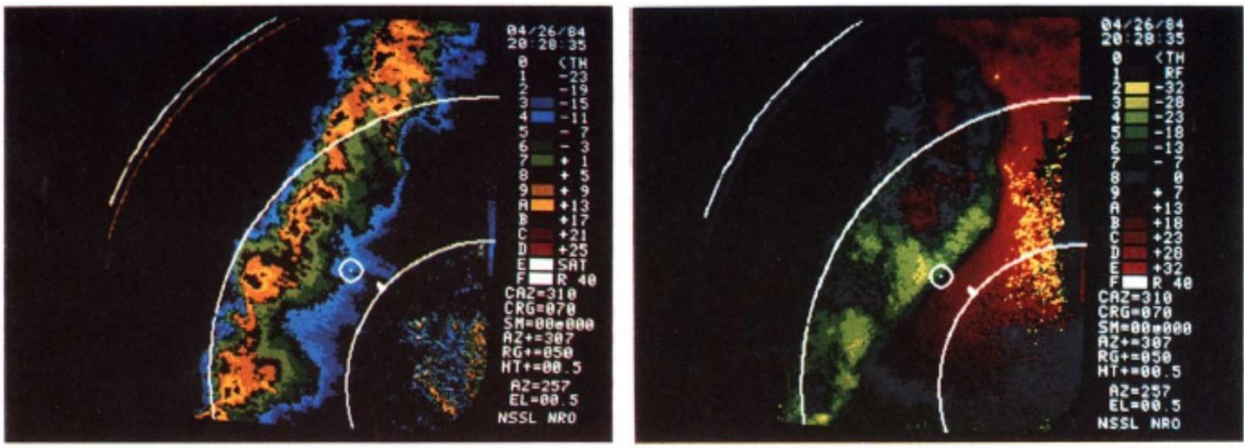

Figure 2.5: Example of a gust front with no thin line on reflectivity (left). The gust front is still visible using the Doppler velocity (right) as the center of the gradient of inbound (green) and outbound (red) velocities. Reproduced from Klingle et al. (1987).

Gust fronts can also appear as linear patterns on the Doppler spectrum width field. Spectrum width is a radar field that detects variations in the Doppler velocity spectrum, caused by changes in speed and direction (shear). The leading edge, and within the head, of a gust front are regions that have been identified as regions of turbulence and mixing, which can be observed as linear regions of wide velocity spectra (Klingle et al., 1987) (Fig 2.6). However, gust fronts are not the only cause of these broad signatures on spectrum width. Klingle et al. (1987) states that some other causes such as the weak echo regions at the edges of storm cells, areas of range aliasing or folding. Also, other sources of turbulence due to the mixing of drier and moist air surrounding thunderstorms or even artifacts of radar processing techniques.

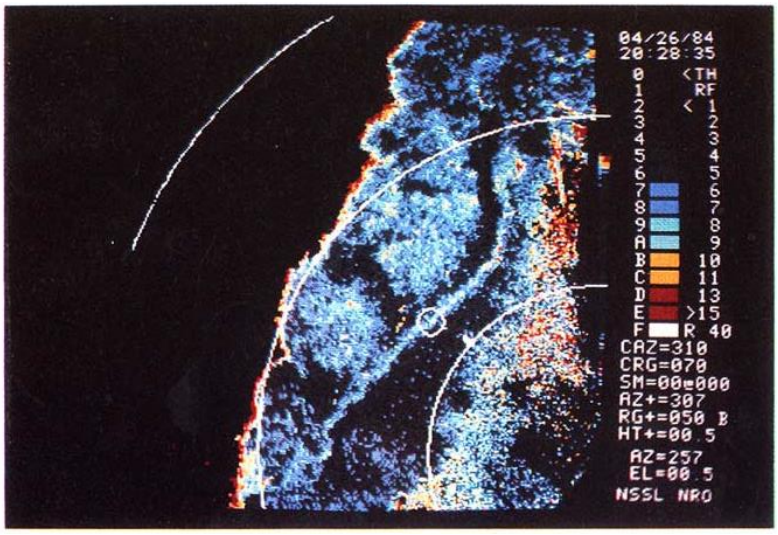

Figure 2.6: An example of a gust front on Spectrum Width. Reproduced from Klingle et al. (1987).

2.2.2 Role of Gust Fronts in Nowcasting

Due to their potential as a forcing mechanism, gust fronts (and other convergence lines) play a prominent role in nowcasting operations. The effect of gust fronts and other convergent phenomena as a source for convective initiation in unstable environments, as well as propagation, has been extentensively studied and documented over the years (Purdom, 1976; Goff, 1976; Weaver and Nelson, 1982; Klingle et al., 1986; Wilson and Schreiber, 1986; Schreiber, 1986; Wilson and Mueller, 1993; Wilson and Megenhardt, 1997; Roberts and Rutledge, 2003; Hwang et al., 2017). The studies out of the Convection Initiation Project highlighted the frequency of thunderstorm

initiation with moving and colliding boundaries within the Denver, Colorado area. Noting that most of the thunderstorms initiated during the project, 79% of 418 storms, were in close proximity to observable boundaries (Wilson and Schreiber, 1986; Schreiber, 1986). This result of the project suggested that boundaries being a source of initiation for convection is a rule rather than an exception for nowcasting, especially given how readily the boundaries could be identified using surface stations and Doppler radar (Schreiber, 1986).

Weaver and Nelson (1982) expanded the understanding of the influences that gust fronts have on thunderstorms and their development. They found that in addition to role gust fronts can play in convective initiation, they can have an impact on all aspects of a thunderstorm life cycle. Notably that thunderstorm intensification and tornadic development can be caused by gust fronts supplementing the vertical motion already present in the primary updraft of the thunderstorm. The only tornadic development observed during their study occurred at the point of a thunderstorm near the intersection of two outflow boundaries, rather than with the mesocyclone as is typical for supercells (Weaver and Nelson, 1982; Sills et al., 2004). In addition, they found that the discrete motion and propagation of thunderstorms (supercells in their case) can influenced by gust fronts (Weaver and Nelson, 1983).

Wilson and Mueller (1993) used these ideas in their study to conduct a nowcasting experiment with real time operators, as well as using extrapolation and persistence forecast methods. They found that forecasters using observations of radar observed boundaries along with visual cloud observations were effective in developing

successful nowcasts of thunderstorm initiation. Operator forecasts were found to be more successful than persistence and extrapolation methods when dealing with new convection but had some difficulties with accuracy in forecasting dissipation and intensification of existing cells. But, the operators had difficulty in precisely timing and the identifying the correct position of initiation (Wilson and Mueller, 1993). Noting that one reason for the error was due to the manual intensity of boundary identification by operators.

2.3 Sources of Error and Uncertainty

2.3.1 Attenuation

Attenuation is a common source of error and uncertainty within operational and research use of weather radars, particularly shorter wavelength radars. Attenuation, as defined by the American Meteorological society, is a term used to denote the loss of signal strength in radar transmission from one point to another. As the electromagnetic waves emitted by radar travel through a medium, scattering and absorption of the wave occurs as it comes in contact with various scatterers like hydrometeors. High concentrations of scatterers can result in a greater loss in returning signal to the radar, in situations with a band of heavier precipitation ahead of lighter and steadier precipitation, the heavy cells act to block the radar transmission from reaching the lighter sections.

Attenuation can also be a direct hindrance to the radar itself, especially in the form of radome wetness attenuation. When heavy precipitation moves over a radar, consistent heavy precipitation can cause water to build up and flow over the radome. This constant flow of water will block out transmissions in all directions as the radar waves interact with the water on the radome. Frasier et al. (2013) notes that wetness attenuation is a common problem for X-band radars during these situations, due to their higher frequency radiation. While this is normally more of a problem for studying rainfall rates or distribution, wetness attenuation can also be a problem for the observation of gust fronts. In particular, signal blockage during these periods will obscure the thunderstorm that is under observation for producing a gust front, as well as obscuring the velocity needed to observe the convergence and divergence of hydrometeors.

2.3.2 Ground Clutter

Another source of uncertainty comes in the form of ground clutter. Ground clutter is a blanket term for potential non-weather scattering targets on the ground that the radar beam can interact with, sometimes paired with particulate noise. These targets can come in the form of trees, buildings, powerlines and radio towers, as well as particulates and biological targets (Rinehart, 2010). Normally the presence of ground clutter on the lowest scanning angles can be a reassurance that the radar is working properly, during weather events these signals can obscure other low return signals that

are targets for observation. In the case of gust fronts, the thin lines on reflectivity can be potentially obscured by particulates and other ground clutter when the boundaries are in close proximity to the radar, as they are all sources of clear air echoes. This can also translate to the obscurity in the velocity field, ground targets that can be influenced into motion, such as trees in the wind or particulates, would potentially become visible on the velocity field within those close ranges, and in turn display convergence-divergence signals near the radar.

2.3.3 Gust Front Movement

The last major expected source of uncertainty is based in the movement of gust fronts with respect to the radar. As mentioned previously, gust fronts are observed within the velocity field by observing the radial convergence produced by the interaction of the thunderstorm outflow and the environmental air. Radial convergence is best observed when the boundary is moving directly towards or away from the radar, or "perpendicular to the radial". However, when a gust front, or sections of a gust front, move parallel to the radial (tangential to the radar beam) the radial convergence signatures are not detectable (Uyeda and Zrnic, 1986; Klingle et al., 1987; Wilson et al., 1980). These signals are azimuthal (rotational) in nature and require additional methods to display the proper signal methods to detect boundary signatures. Gust fronts aligned parallel to the radial will experience a loss (or change) in signal that will

make identification more difficult, as this study does not implement products for detecting azimuthal shears.

Chapter 3: Instruments and Methodology

3.1 Vertical Velocity Data

Vertical velocity data used in this study was collected (by request) from three eddy covariance towers within the region of central Missouri. The first of these sites is the Missouri Ozarks AmeriFlux Site (MOFLUX; AmeriFlux site ID US-MOz) located within the University of Missouri Baskett Wildlife Research Area. The other two towers are located near Centralia, MO operated by the United States Department of Agriculture – Agricultural Research Service (USDA-ARS). Data was collected for all MZZU case days where a suspected gust front signature was identified in radar divergence and or reflectivity imagery. Cases occur mainly within the standard convective season (March through October), and in the years since the installation of the MZZU radar (2015). The data was also collected based on the conversion from local time (CST/CDT) to Universal Coordinated Time (UTC), where case events between 00:00 to 06:00 UTC would require the previous day's vertical velocity data.

The high resolution vertical velocity data acquired was recorded in timesteps of a tenth of a second, so the data was brought in to MatLab for processing. Data was organized using a simple set of commands that divided the data set into groups of 600, the number of points in one minute. Groups were then averaged over the one-minute intervals to create the average vertical motion per-minute ($\overline{w}$). These one-minute steps were chosen to bring the data closer to the five-minute intervals for radar scans, while

also retaining a higher temporal resolution to fill in the gaps between scans. The $\overline{w}$ data was analyzed for peaks in upward motion at the time of gust front passage, as the peak in upward motion is found in the frontal updraft. This rise is expected to be followed by a decreasing trend in the vertical motion as the front passes and the sensor enters the turbulent region following the boundary, and eventually the onset of precipitation from the thunderstorm.

To supplement the coarse resolution of $\overline{w}$ used for analysis, Turbulence Kinetic Energy (TKE) was also calculated. Since gust fronts are turbulent features in the atmosphere, it can be expected that the TKE would be on the rise or peaking along with the rise-fall trend in $\overline{w}$ with the passing of the frontal updraft, as well as with sensor sampling the turbulent region behind the frontal boundary. Increasing TKE with gust front passage can be seen in Jarvi et al. (2007), which was the base for implementing TKE into this study. TKE was calculated using the equation:

$$TKE = \frac{\left(\overline{u'^2}\right) + \left(\overline{v'^2}\right) + \left(\overline{w'^2}\right)}{2} \qquad (1)$$

3.1.1 MOFLUX Sensor: CSAT3 Sonic Anemometer

Wind velocity measurements at the MOFLUX site were sampled at 10 Hz using a CSAT3 model sonic anemometers-thermometers (Campbell Scientific Inc., Logan UT). Wind velocity is inferred by the travel time of acoustic pulses between the transduces of the sensor suite, which is then transformed into the orthogonal wind components (u, v,

w) (Campbell Scientific, 2017). Wind velocity data resolution measured by the CSAT3 is 1 mm s^{-1} in the u and v components, with a vertical resolution of 0.5 mm s^{-1} (Campbell Scientific, 2017). Offset error for velocity measurements by the CSAT3 are less than +/- 8 cm s^{-1} for u and v components, and a vertical (w) offset error of less than +/- 4 cm s^{-1}.

There have been several studies that have investigated the accuracy of the CSAT3 for measuring wind speed in the horizontal and vertical components. Mauder et al. (2007) compared several models of sonic anemometers with participants consisting of both orthogonal and non-orthogonal types. Three of the participants, including the reference sensor, for this study were the Campbell Scientific CSAT3. The study found that the CSAT3s had good agreement with most of the sensors across multiple parameters measured by sonic anemometers, such as: horizontal velocity, vertical velocity, and sonic temperature. They concluded that the CSAT3s can be classified as well-qualified instruments for research if operated properly (Mauder et al., 2007). Also, that sonic anemometers can be used to measure absolute wind velocities in addition for using the components for purely calculation in the eddy-covariance method.

While Mauder et al. (2007) found that the CSAT3 was overall a capable instrument for research, there are some uncertainties to be aware of when using the CSAT3. Kochendorfer et al. (2012) notes that that non-orthogonal sonic anemometers have generally underestimated energy flux calculations when compared to orthogonal sensors. They found that when comparing the CSAT3 with orthogonal sensors, that the non-orthogonal type is prone to w errors based on the physical design of the sensor (Kochendorfer et al., 2012). Stating that the design is primarily used to measure wind

velocity when the vertical component is negligible, suggesting that future studies should use sonics designed to minimize the effects the sensor structure has on flow, rather than implementing more corrections into the eddy-covariance method to compensate for errors. Frank et al. (2012) agrees with the findings of w underestimation found in Kochendorfer et al. (2012). This study compared the orthogonal ATI sonic anemometer to the CSAT3 to determine how much error there was in the non-orthogonal sensor, and the cause of the errors. They found that either the ATI would overestimate w, or that the CSAT3 underestimated w. Further, when they compared their results to Kochendorfer and other comparison studies, they found that the CSAT3 underestimated w by around 10% compared to the ATI sensor (Frank et al., 2012). They proposed that the errors in w could be caused by the design of non-orthogonal sonic anemometers like the CSAT3, as the errors in w cause the later flux calculations to also be underestimated. While this problem with the CSAT3 underestimating the vertical velocity component is notable, it does not severely impact the role of vertical velocity measurements in this study. The vertical velocity data is being used to observe the trends in $\overline{w}$ as a gust front crosses an instrument site rather than relying on the absolute value of wind speed to compare to other observations of w in frontal updrafts. While the absolute value of the wind speed does help illustrate the trend during the discrete time intervals, it is not the primary focus in the analysis.

3.1.2 Centralia Sensors: Campbell Scientific IRGASON

The instrument used to measure wind velocities (at 10Hz) at the two sites near Centralia, MO (ASP and BAU) was the IRGASON (Campbell Scientific Inc., Logan UT). The IRGASON is an Integrated CO2 and H2O Open-Path Gas Analyzer combined with a 3-D sonic anemometer. The model of sonic anemometer integrated within the IRGASON platform is a CSAT3 model, which is the same model of instrument used at the MOFLUX site, but is an updated version of the instrument. The integrated CSAT3 has the same wind measurement capabilities as the standard CSAT3. Documentation about the accuracy of the integrated CSAT3 model sonic anemometer, or the working order of the instrument sites for Centralia ASP or BAU, were unavailable at the time of this study. It was assumed that the IRGASON – CSAT3 was as capable as the standard CSAT3, as well as sharing the same uncertainties in measurement.

3.2 Radar Data

Radar data used in this study was obtained using the University of Missouri – Columbia's MZZU X-band radar, as well as the KLSX S-band radar from the NWS Saint Louis Weather Forecast Office. KLSX data was obtained by request through the National Centers for Environmental Information (NCEI) Next Generation Weather Radar (NEXRAD) data archive. Data acquired through NCEI was centered around time of precipitation events on a desired case day to cut down on later processing time. Precipitation events were selected based on what available archived data had

interesting convective activity that could have produced a gust front. Data was processed through the Warning Decision Support System-Integrated Information suite before being unzipped and analyzed within MatLab. The radar products analyzed were the merged divergence (convergence) product and reflectivity, both at the lowest available levels.

3.2.1 The Warning Decision Support System – Integrated Information

The Warning Decision Support System- Integrated Information, also known as WDSS-II, is a system of tools designed for the analysis, diagnosis, and visualization of remotely sensed weather data. It was developed in cooperation between the National Severe Storms Laboratory (NSSL) and the Cooperative Institute of Mesoscale Meteorological Studies (CIMMS), out of the University of Oklahoma. The purpose of this system is to provide radar information with a greater spatial and temporal resolution using data from multiple radars. In addition to taking in data from multiple sources to create a single grid, the system also can merge data in the vertical into distinct levels of the atmosphere, knowns as Constant-Altitude Plan Position Indicators (CAPPIs). This is advantageous since it removes the need to switch between radar scanning angles to track and observe key meteorological features at a particular elevation. WDSS-II also provides applications to generate derived products for post analysis and real time use. Specific details on development of data merging and WDSS-II applications can be found in Lakshmanan et al. (2006,2007).

The two applications from the WDSS-II system used in this study are w2circ and w2merger. w2circ is an application for calculating circulation products, such as azimuthal shear or divergence. The application uses a linear least squares method to minimize the large variances in calculating rotational and divergent shears that come from more traditional calculation methods (Lakshmanan et al., 2006). This method within the application also removes radar dependencies that are involved with the detection of rotation and divergence, allowing these derivatives of velocity to be viewed in three-dimensional space. While this study focuses on the lowest available level of radar imagery this can be advantageous in observing the slope of a gust front or other circulation features. The advantage that comes with w2circ in relation to cleaning up velocity data, is that it makes identifying the divergence (convergence) signatures that can be attributed to boundaries less difficult than with the initial radial velocity field. Products made from the w2circ application have seen prior use in research, such as the use of rotation tracks derived from azimuthal shear by Miller et al. (2013) to develop an automated mesocyclone tracking algorithm.

w2merger, as stated earlier in this section, is an application that merges radar from multiple sources into a single three-dimensional grid. Algorithms within the tool take into account differences in radar beam geometry, gaps in vertical scans, time synchronizations, various beam resolutions, terrain blockage, differences in radar calibration, time stamp inaccuracies, and storm motion from multiple sources when creating the grid. While this application is usually used for multiple radar operations, this study will be using it with single radars for the cases studied. The application

outputs the merged products in netCDF files, which can then be used within MatLab for analysis. The two data sources used in this study are treated differently, KLSX data is merged to a 256 x 256 1 km resolution grid, and MZZU data is on a 384 x 384 0.5 km resolution grid (effectively 192 x 192 km). This is based off the shorter effective range but higher resolution for MZZU data.

3.3 MatLab Analysis

Following WDSS processing into the respective cartesian grids, the data was then moved into the MatLab software for analysis. To discuss the cases chosen in chapter four, further processing was performed on the chosen radar imagery for all case days. The reflectivity data was simply read in and displayed for the lowest available level for a given event. The primary function of the reflectivity field in this study is to serve as a spatial reference for the divergence data, to determine whether or not the target gust front was with the heaviest precipitation, or out ahead of the storm.

For analysis of the divergence product, the goal was to isolate divergence (convergence) signatures that were suspected to be gust fronts. To accomplish this task a system of data filtering was performed. This procedure used is similar to the process for cell identification featured in Lack and Fox (2012) and Micheas et al. (2007), except modified. The process is used in this study to isolate the gust front signatures with coherent areas of divergence (convergence) has four filtering stages. These stages consist of:

- Applying Divergence/Convergence threshold
- Applying Area threshold
- Dilation
- Erosion

An example of the complete four stage process can be found in Figure 3.1.

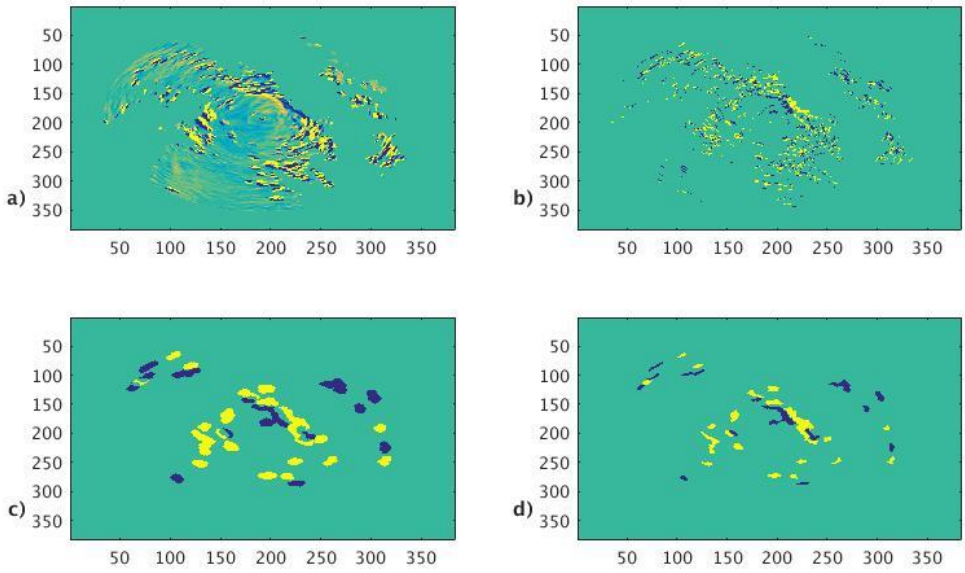

Figure 3.1: Example of the data filtering process starting with a) the WDSS processed data, b) Div-Conv thresholds applied, c) Area threshold and Dilation, and d) Erosion. The example uses data from MZZU 2016 07 06 1606 UTC.

The filtering process begins with the "raw" data from the WDSS-II processing being fed into the program. Raw data shows the doppler velocity field of the given storm in terms of convergence and divergence. Positive values indicate divergence, and negative values indicate convergence (or "negative divergence"). This can be seen in

Figure 3.1a. There are features of interest located within the noise and extremes that are useful for locating the potential gust front. Since these features are on neither of the extremes in terms of value, a range of interest can be established to begin isolating the signature.

Next the initial divergence and convergence thresholds are applied to the WDSS data. The threshold for divergence and convergence assigned to the example seen in figure 3.2 are 7.5×10^{-4} to 2.0×10^{-3} s^{-1} for divergence, and -7.5×10^{-4} to -4.0×10^{-3} s^{-1} for convergence. Any signatures of divergence (convenrgence) with values that fall outside of the thresholds are assigned to zero. Values that fall inside the thresholds are assigned to 1 or -1 for convergence and divergence respectively. The designation of the divergence and convergence is flipped during initial threshold application and the following processing stages due how the code was written to display both convergence and divergence together without running separate programs. The lines of code responsible for the shift can be found within the program code listed in the appendix, but the relevant lines are also listed below for convenience:

dcell# = div<divthresh2 & div>divthresh1

ccell# = div>convthresh2 & div<convthresh1

imagesc(ccell#-dcell#)

Where ccell is the convergence, dcell is the divergence, and # is a placeholder for the processing stage (no number for Div-Conv threshold stage, 3 for Dilation, 4 for erosion). Another use for subtracting the divergence and convergence from one

another is to prevent the overlapping of data during the later stages of dilation and erosion.

The results from the application of the div-conv thresholds can be seen in the Figure 3.1a and b, and more clearly within Figure 3.2. It is clear, that while a fair amount of the extrema has been removed from the div-conv field, there are still plenty of extraneous features that are of little interest in this study. This leads in to the next stage of filtering by applying the area threshold. The area threshold allows for the removal of any Contiguous Divergence Areas (CDAs) whose area falls below a number of pixels in size given by the user. The area threshold used for this example and within one of the settings discussed in chapter 4 is 15 pixels. The resulting filtration after applying the area threshold can be seen in Figure 3.3.

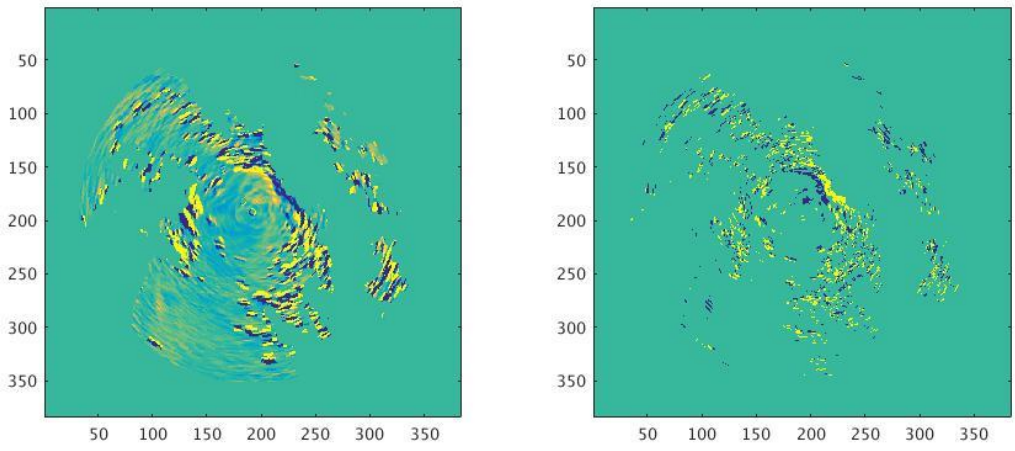

Figure 3.2: MZZU 2016 07 06 1606 UTC following the application of the divergence-convergence thresholds. Left: Raw WDSS data, Right: Div-Conv thresholds applied. Following threshold application convergence is yellow and divergence is blue.

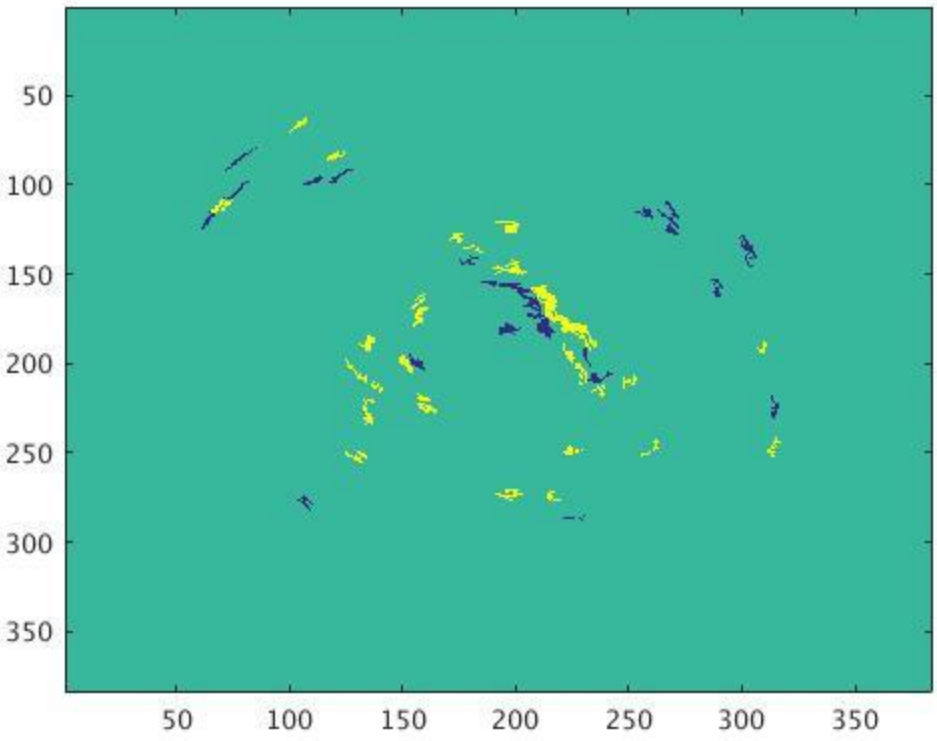

Figure 3.3: Results from applying the area threshold for MZZU 2016 07 06 1606 UTC following Figure 3.2.

After the area threshold is applied there are several CDAs in close proximity to each other. It can be inferred that these CDAs can be parts of the same feature and need to be connected. There are also some extra CDAs remaining that are not the target that still need to be removed. This leads into the final two stages of the modified cell identification image processing used, which makes use of the techniques of dilation and erosion. These techniques focus on the concept of adding or removing pixels to the CDAs seen in the images being processed. Dilation, for example, applies a mask to the image and expands the radius of the CDAs by a number of pixels given by the user.

Erosion is the same process but in reverse, removing pixels. The CDAs following the dilation phase have grown larger, and now there are fewer individuals (Fig 3.1c, Fig 3.4). Gaps between CDAs during this stage are caused by the program to prevent overlap, as mentioned earlier. Following the erosion phase the CDAs are trimmed down to close to their original size. But, as seen with the dilation, the new number of individual CDAs remains. The results of the erosion stage can be seen in Figure 3.1d and more clearly in Figure 3.5.

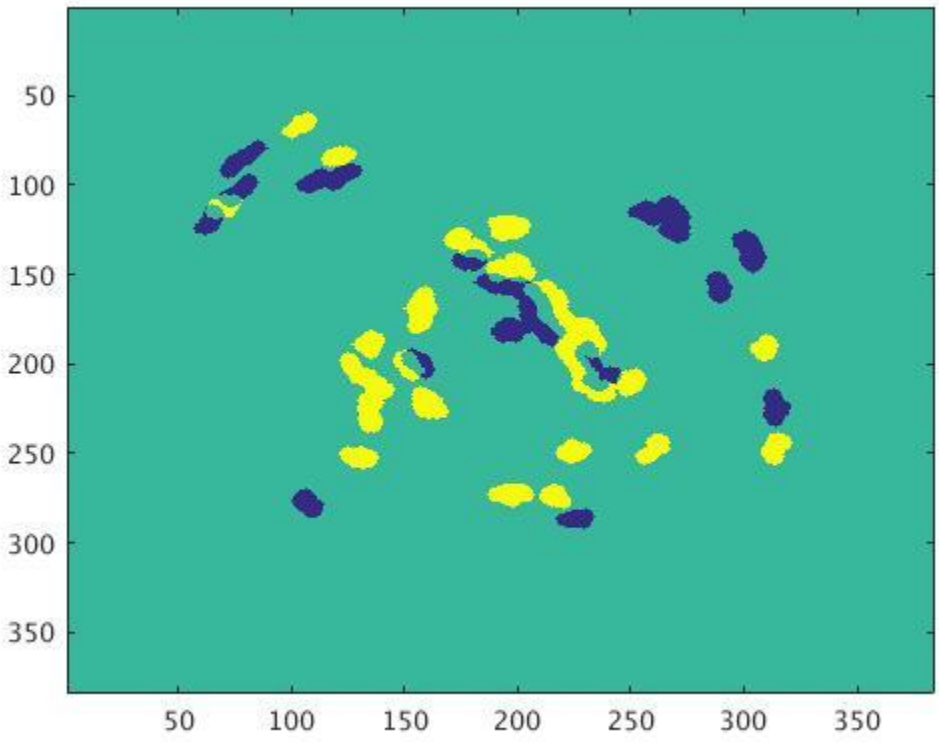

Figure 3.4: MZZU 2016 07 06 1606 UTC during the dilation phase.

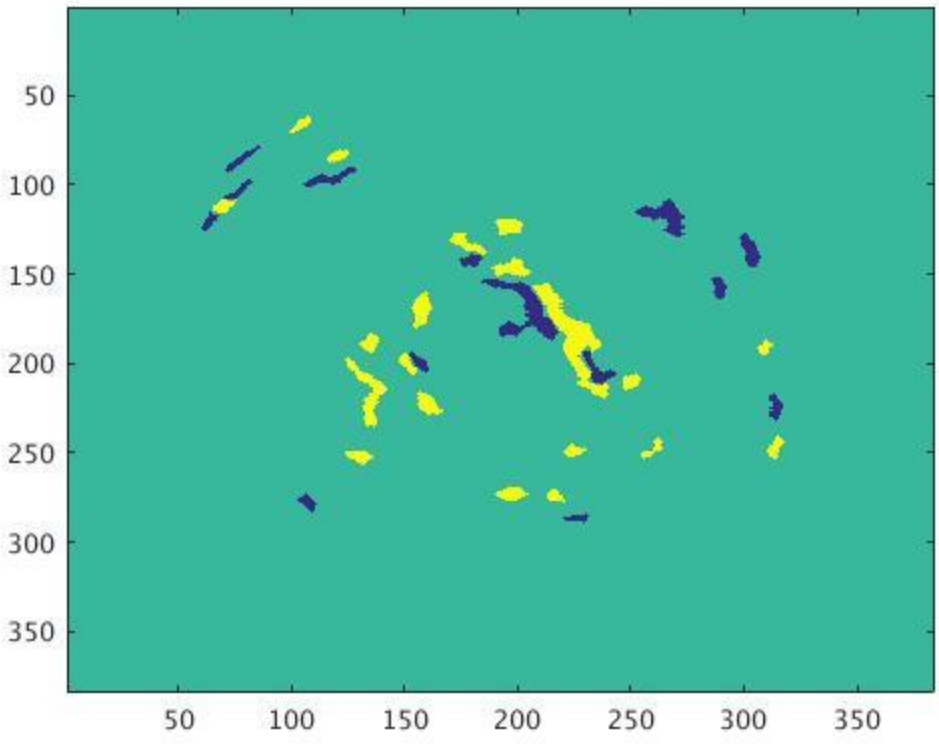

Figure 3.5: MZZU 2016 07 06 1606 UTC following the erosion phase.

While it would prune out more of the noise and other unwanted CDAs present following the erosion stage, no continued or repeating processing stages were included in this study. This was done for ease of use in adjusting the processing settings while examining cases. As adjusting one phase to compare various settings, such as the effects of different area thresholds or dilations, would require adjusting the later stages as well. The procedure described above was then applied to multiple time steps to generate an event series for the cases covered within this study. The testing of thresholds for parameter sets will be discussed in later in this chapter.

3.4 Determining the Gust Front Signature

Establishing what constituted a potential gust front signature on the divergence product was imperative for this study. As previously discussed, it is known that boundaries exhibit notable signatures which can be observed in the WDSS derived product (Lakshmannan et al., 2007; Smith and Elmore, 2004). The optimal signal aimed for in this study is the convergence-divergence (divergence-convergence) pair. Gust fronts, as convergent wind phenomena, exhibit convergence at and ahead of the frontal boundary due to the interaction of airmasses. Divergence in these pairs can be attributed to the outflow air behind the boundary that forces frontal movement, as well as the downdraft associated with the precipitation in the parent thunderstorm (Klingle et al., 1986). An example of this pair can be seen in the theory application used in Smith and Elmore (2004) (Fig 3.6). In addition, lone linear convergence features (convergence lines) can also be attributed to the boundaries, especially when observing gust fronts that have moved ahead of the precipitation. A primary cause for the lack of divergence at the boundary in these situations is due to poor sampling and estimation of divergence at lower levels, as mentioned in Ray (1976). In addition, it is possible that larger singular convergence lines could also be due to the gust front updraft being in close proximity to the precipitation updrafts within the parent thunderstorm (Goff ,1976). This study will consider both div-conv pairs as well as linear convergence features (convergence lines) as signatures to indicate possible gust fronts, with reference to radar reflectivity. Meaning that signatures must be located at the leading

edge of the precipitation, or out ahead of the storm in cases with a detached front, to be considered gust front signatures.

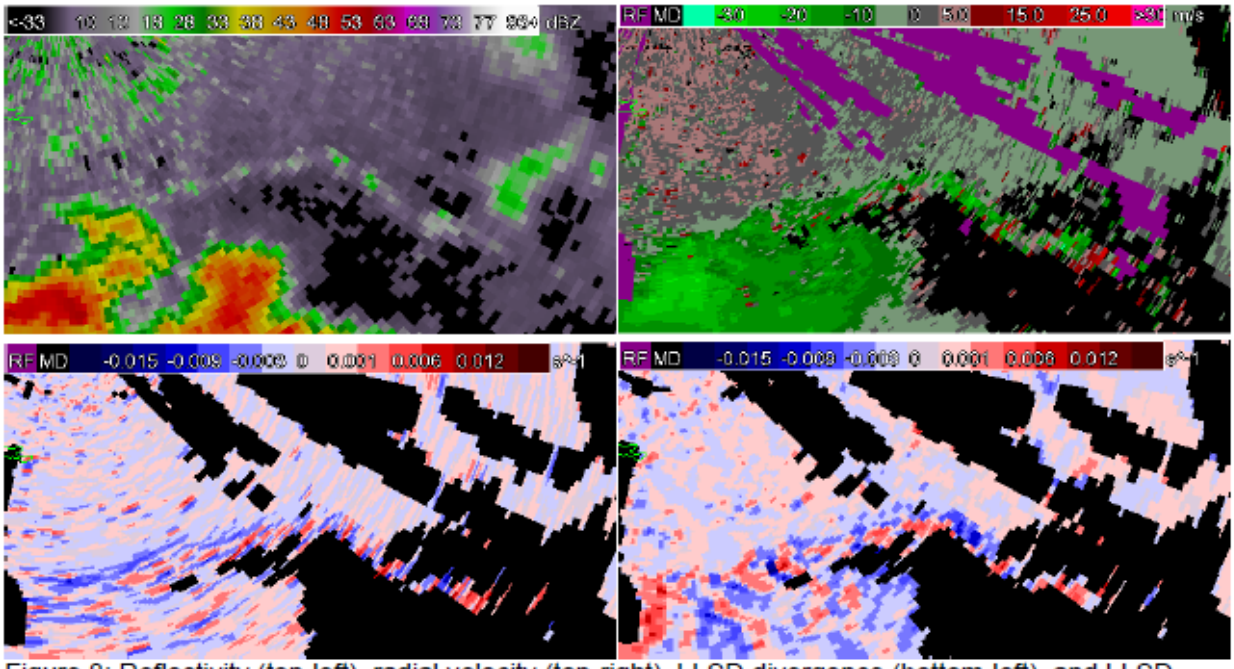

Figure 8: Reflectivity (top-left), radial velocity (top-right), LLSD divergence (bottom-left), and LLSD rotation (bottom-right) for depicting gust front.

Figure 3. 6: An example of the divergence and convergence signals that can be attributed to a gust front (Bottom Left panel). Test application of LLSD divergence. Reproduced from Smith and Elmore (2004).

3.5 Generation Parameters

One of the objectives of this study was to determine the parameters that generated gust front signatures within the derived divergence field in image processing. One set of parameters was determined to be insufficient for detecting gust fronts of different types depending on the radar used. It was also found in this study that one set of parameters would not be interchangeable across different radar types, due to differences in radar power but also in how the data is processed. The three parameter sets (settings) that were developed in this study are seen in Table 3.1:

Table 3.1: The settings used to generate the gust front signatures seen during the cases in Chapter 4.

	MZZU In-Storm	**MZZU Thin-Line**	**KLSX**
Area Threshold	15 Pixels	2-4 Pixels	1-4 Pixels
Convergence Threshold	-7.5×10^{-4} to -2.0×10^{-3} s^{-1}	-7.5×10^{-4} to -2.0×10^{-3} s^{-1}	-7.5×10^{-4} to -2.0×10^{-3} s^{-1}
Divergence Threshold	7.5×10^{-4} to 4.0×10^{-3} s^{-1}	7.5×10^{-4} to 4.0×10^{-3} s^{-1}	7.5×10^{-4} to 4.0×10^{-3} s^{-1}
Dilation	4 Pixels	4 Pixels	4 Pixels
Erosion	3 Pixels	3 Pixels	3 Pixels

The MZZU in-storm set was the base group of settings developed for use in this study. They were developed for use for detecting gust fronts that remain within the precipitation of a thunderstorm. Why these settings were chosen is due to how they resolved these features, which was discussed with the image processing earlier in Chapter 3. Many of the settings that were used in this set (div-conv thresholds, dilation and erosion) transferred well between different gust front types and radar data in this

study, so these parts of the settings remain unchanged. The primary difference between each set is the area threshold. As mentioned in Section 3.3, the area threshold of 15 pixels was chosen due to how it would remove a large amount of extraneous signals that were found in the divergence within a thunderstorm. Additionally, 15 pixels was chosen instead of higher thresholds such as 20 pixels or higher since it allowed for some of the variation that comes with divergence (and Doppler velocity) over time that would be lost if the area threshold removed these features before dilation. Finally, 15 pixels was chosen to accommodate MZZU radar data having a resolution of 0.5 km.

Thin line-related gust-fronts ahead of thunderstorms have a significantly smaller area compared to their in-storm counterparts. To account for the difference in the size of features, the area threshold was lowered to allow these smaller features to make it past the area filtering stage, so they can be made more visible through dilation and erosion. This would not be possible with the in-storm area threshold of 15 pixels. A range of thresholds was allowed for this set, once again to account for variations in the divergence field, since not all thin lines share a uniform area or thickness. A comparison of the area thresholds for thin lines can be seen with the raw data in Figure 3.7 and Figure 3.8.

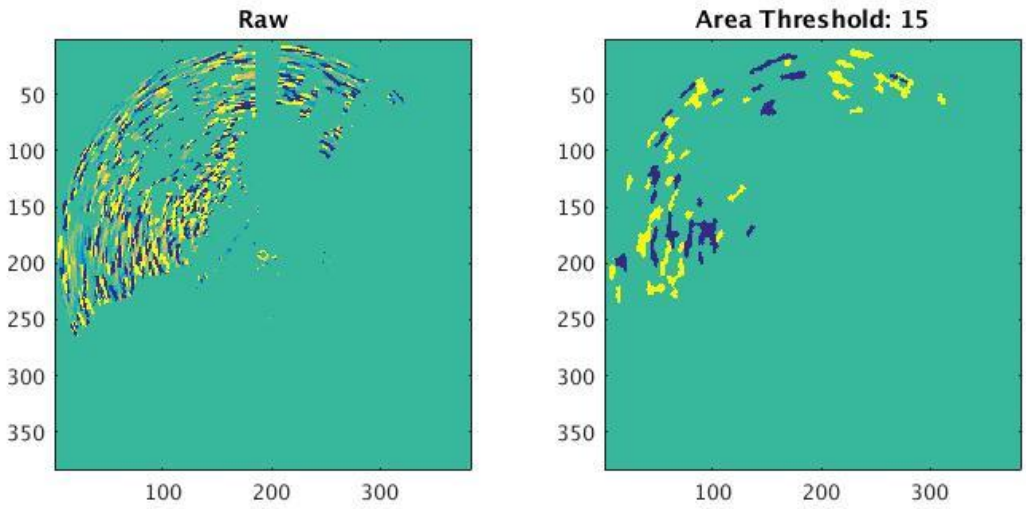

Figure 3.7: 2017 05 19 0647 UTC - Example of area thresholds for thin-line scenarios. Comparing raw to the "Standard" area threshold of 15 pixels.

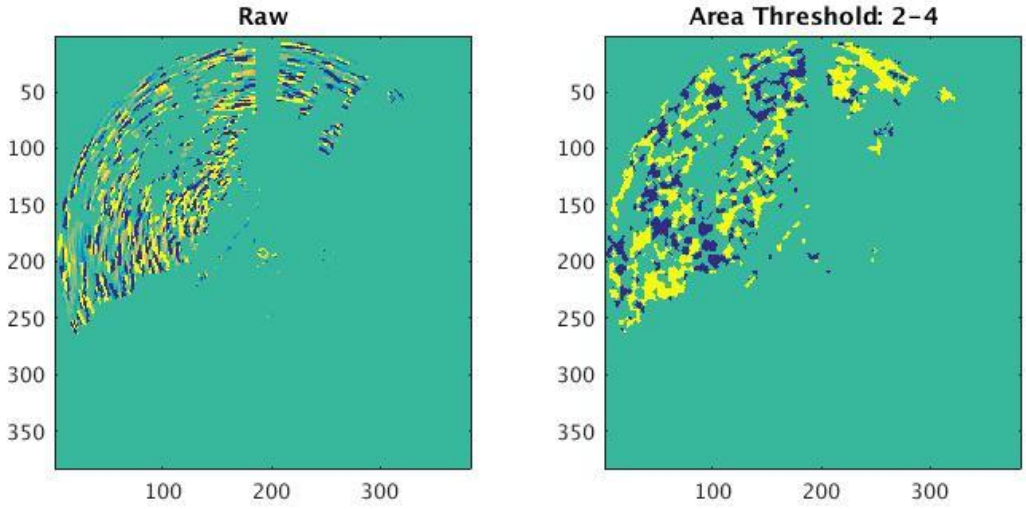

Figure 3.8: 2017 05 19 0647 UTC - Example of area thresholds for thin-line scenarios. Comparing raw to an area threshold within the range of 2-4 pixels.

The Saint Louis (KLSX) data also required adjustments to area threshold to generate gust front signatures. When translating the "default" MZZU settings to the

KLSX data, most if not all of the features were removed due to being smaller than the 15-pixel area threshold from the MZZU in-storm settings. This was due to the processing differences between for the two radars. As mentioned previously in this section, MZZU data has a grid size of 0.5km for its radar data, while KLSX has 1 km grid resolution. Since the MZZU in-storm threshold was made for a grid resolution of half the size compared to KLSX the area threshold needed to be adjusted down to at least half the size to work with the coarser resolution. The area threshold range for KLSX was made to be 1-4 as it allowed for observation of both in-storm gust fronts as well as thin lines for the cases in this study. A Comparison of the area thresholds and the raw data can be seen in Figure 3.9 and Figure 3.10 below.

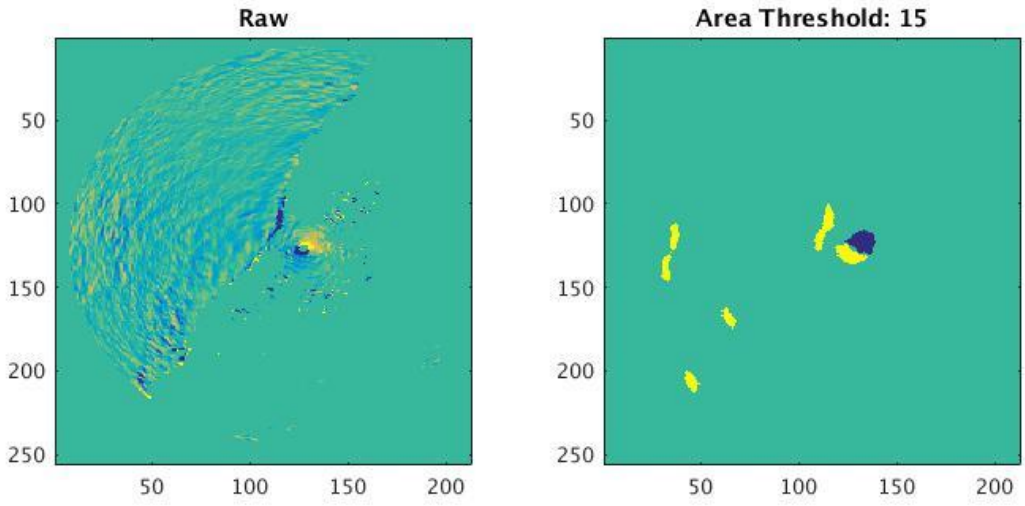

Figure 3.9: 2017 03 07 0554 UTC- Example of area thresholds on KLSX. Comparing the raw data to the "standard" area threshold of 15 pixels.

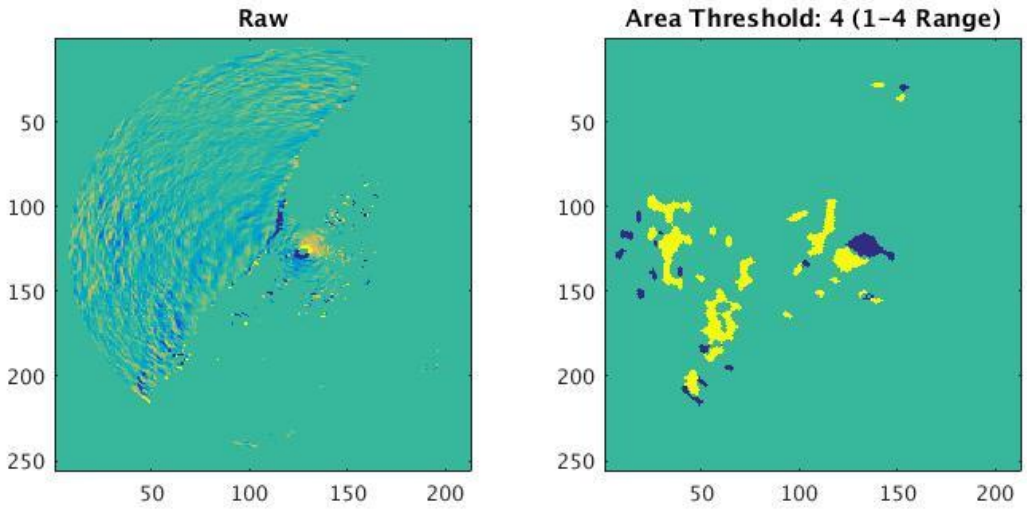

Figure 3.10: 2017 03 07 0554 UTC- Example of area thresholds for gust fronts on KLSX using a range of 1-4 pixels.

Dilation and erosion settings were kept constant across all parameter sets developed in this study. The dilation was made 1 pixel greater than the erosion stage to keep the final blobs larger and easier to keep track of with user observation for analysis. Higher values of dilation and erosion were tested, but they yielded the same results as the final dilations and erosions chosen, as long as the dilation was 1 greater than the erosion. Setting the erosion to be greater than the dilation would shave features down smaller than pre-dilation sizes. While this did clean out more unwanted signals from processing, it risked making the target signals more difficult to observe over time, which was a concern given the variability in the wind field and divergence.

Chapter 4: Results

In this chapter, the gust front detection results for the case days chosen will be discussed. Twelve cases that feature potential gust fronts were chosen, with nine cases from the MZZU operating area, and three within KLSX. Each case will begin with a brief description of the storms present during the event. Describing the convective mode of the storms present, as well as any additional details. Most notably however, will be the designation of whether or not an observable thin line was present during the event, and what generation settings (parameters) were used. While the primary use of the divergence product in this study was for detecting "non-visible" or in-storm gust fronts, thin line cases were also included to demonstrate that the product can also be applied to situations where one is visible on reflectivity. Radar imagery is presented with reflectivity on the top row of the images, the divergence field is on the bottom row with yellow representing convergence and blue representing divergence.

When data from an eddy covariance site is referenced it will be presented in two mediums. First, line pots for $\overline{w}$ and TKE will be presented for a given site. Following the line plots will be tables presenting numerical $\overline{w}$ data for the key interval of suspected gust front passage for the given site.

4.1 MZZU Gust Front Cases

4.1.1 06 July 2016

During the morning of July 6th, 2016 a Quasi-Linear Convective System (QLCS) moved through the Columbia, Missouri area as part of an active day of severe weather in the Midwestern CONUS. The system brought high winds to the area, prompting several severe wind reports in the state of Missouri, as well as a couple of tornado reports. This QLCS was a prime candidate for producing a gust front. No visible reflectivity thin line was observed on radar ahead of the storms as observed by the MZZU radar. So, it can be inferred that the potential gust front generated from this storm remained within the precipitation echoes at the leading edge of the heaviest precipitation. The settings used for this case were the MZZU in-storm settings. The lowest available level of radar data from this event was the 01.00 km level on divergence, and 00.00 km on reflectivity.

The line moves into the area from the east-southeast and moves to the northeast over the course of the event period. The target for the potential in storm gust front can be first clearly seen on the divergence product during the 1556 UTC scan, as the QLCS crosses over MZZU. The signature can be seen in Figure 4.1 as a couplet of convergence and divergence, with the convergence on the leading or outbound side of the pair. This div-conv signature is located at the leading edge of the thunderstorm which can be seen by comparing it to the reflectivity scan at that time (Fig 4.1). The convergence is positioned in the lower reflectivities at the forward flank, and the

divergence is located relative to the heavier precipitation, which would be in line with the downdrafts that would feed the thunderstorm outflow.

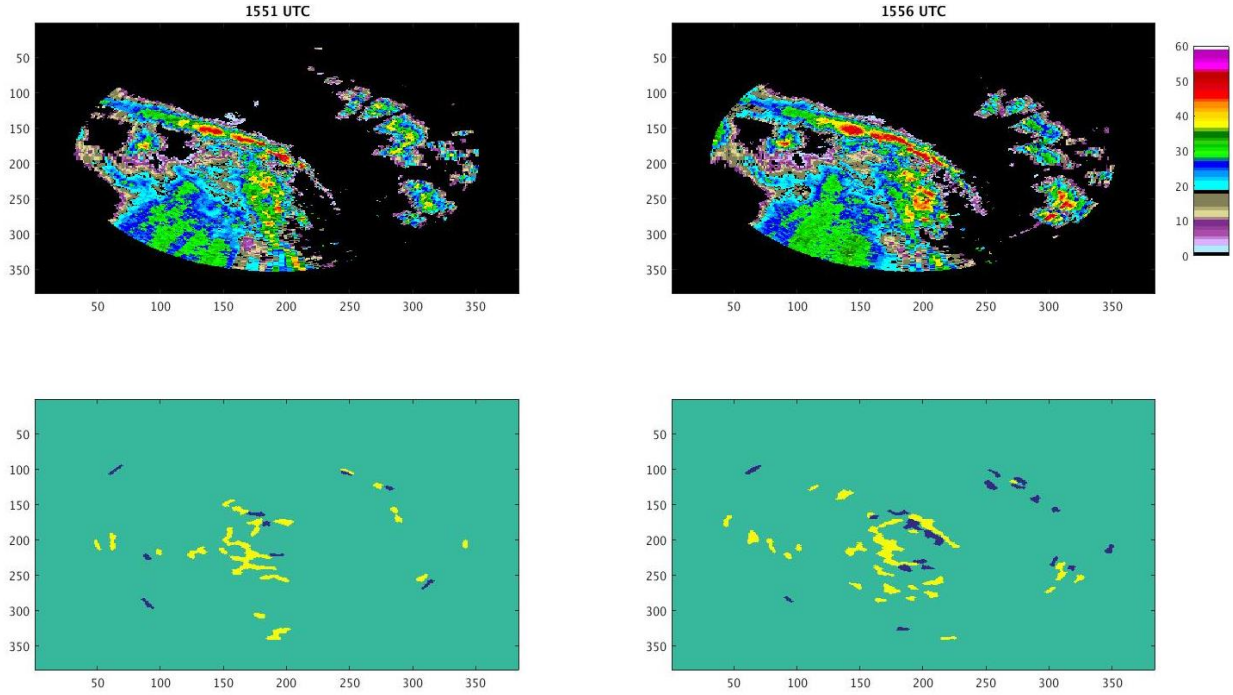

Figure 4.1: MZZU reflectivity and divergence on 2016 07 06 from 1551 to 1556 UTC.

Moving forward through the next few scans the div-conv pair remains relatively consistent spatially (Fig 4.2). Some variation with the overall size and distribution of the blobs is present between the scans, but the couplet maintains a linear region of convergence ahead of its paired divergence. The signals become increasingly inconsistent as the system moves farther away from the radar (Fig 4.3). But, the position of the couplet remains consistent with the leading edge of the QLCS similar to the initial time steps covered.

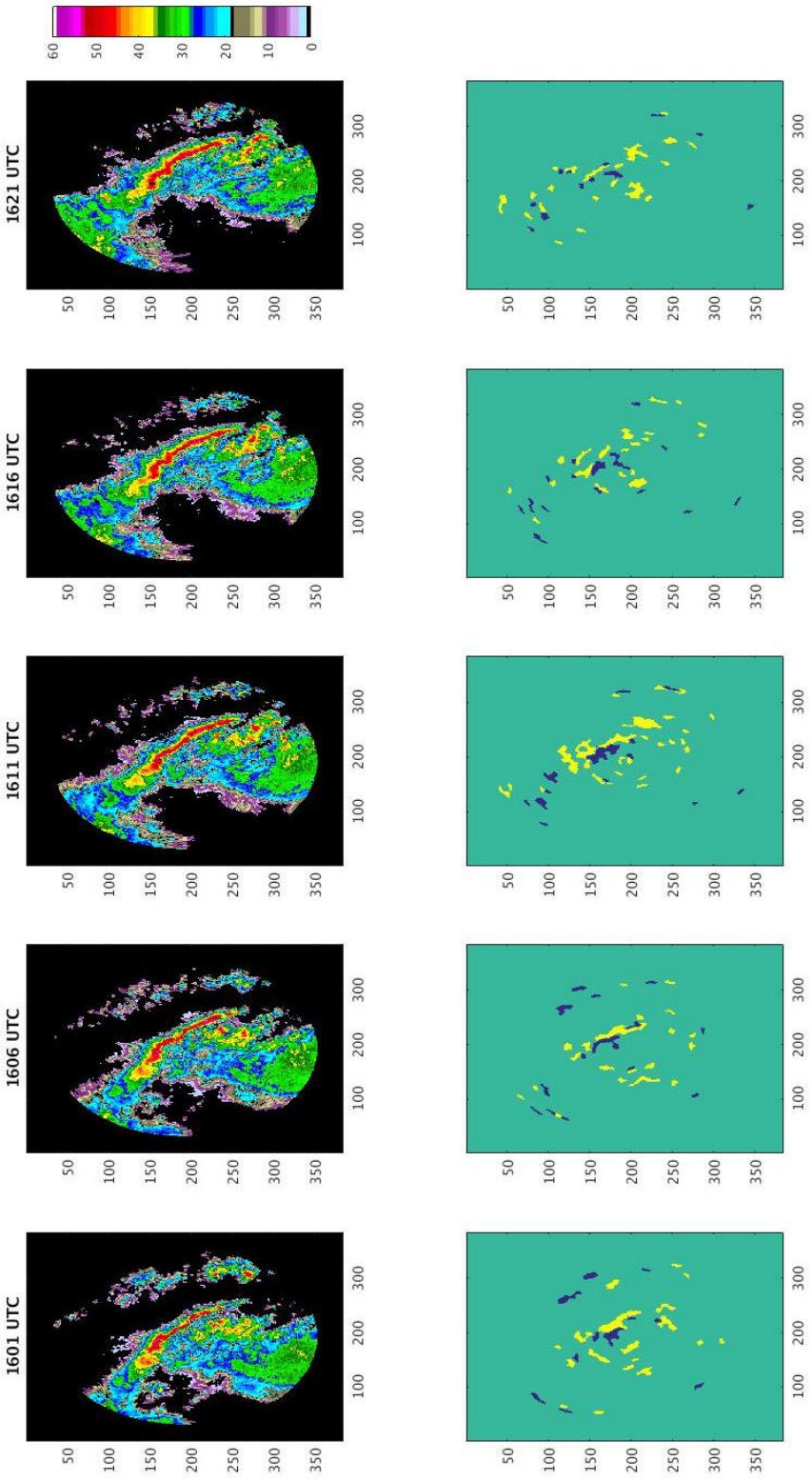

Figure 4.2: MZZU reflectivity and divergence on 2016 07 06 from 1601 to 1621 UTC.

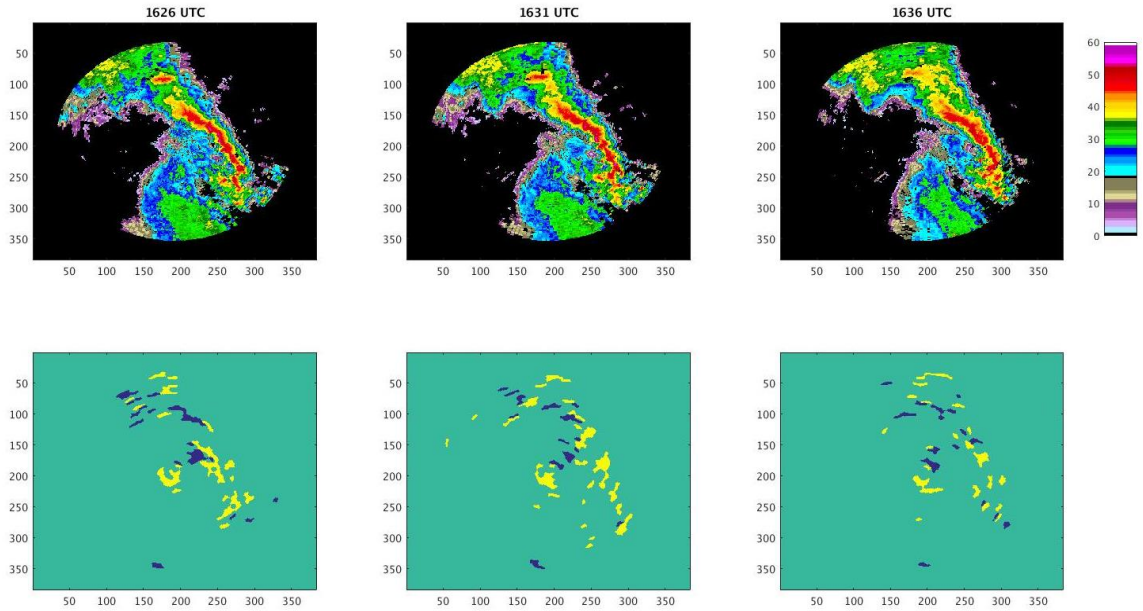

Figure 4.3: MZZU reflectivity and divergence on 2016 07 06 from 1626 to 1636 UTC.

The target div-conv pair did not move directly over the MOFLUX tower as that section of the storm passed by from 1535-1545UTC (Fig 4.4). The $\overline{w}$ data from the MOFLUX tower at the time shows a primarily negative scheme at the time (Table 4.1). This suggests that there was primarily downward motion at the time. Few recordings of weak positive $\overline{w}$ may suggest that some influence of possible outflow was detected by the sensors at MOFLUX. But, the target signature did not cross over the tower, as it was not observed yet, so it is not likely to be the gust front causing this rise.

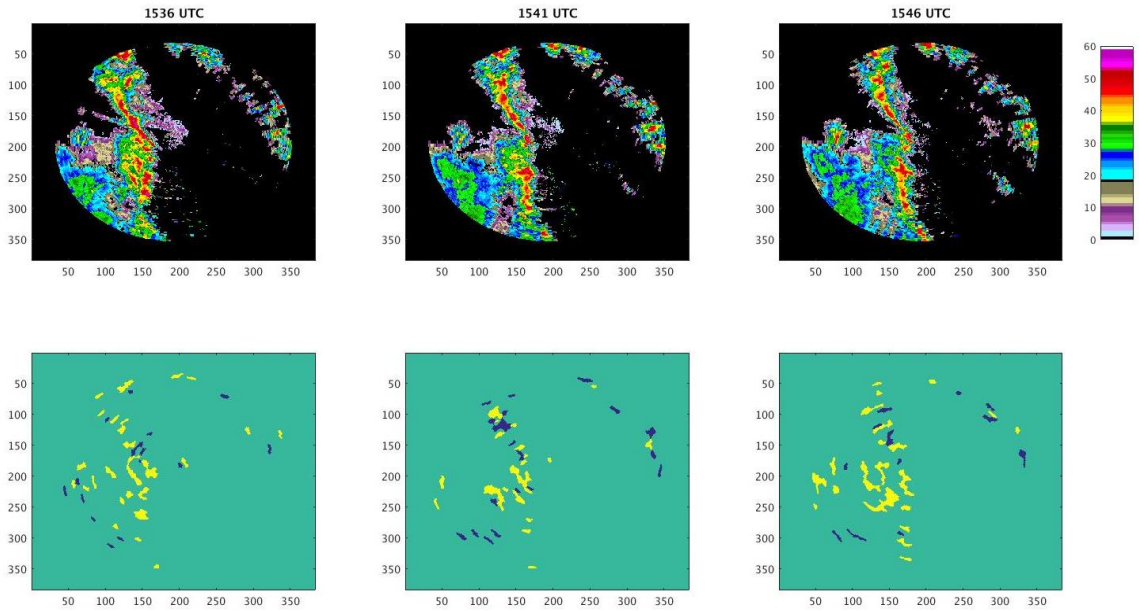

Figure 4.4: MZZU reflectivity and divergence on 2016 07 06 from 1536 to 1546 UTC.

Table 4.1: Numerical $\overline{w}$ data from MOFLUX on 2016 07 06 from 1533 to 1538 UTC.

	Time (UTC)	**1533**	**1534**	**1535**	**1536**	**1537**	**1538**
MOFLUX Primary	$\overline{w}$ (m/s)	-0.1049	-0.2918	-0.0086	0.0097	-0.0272	0.0166
MOFLUX Secondary	$\overline{w}$ (m/s)	0.0681	-0.3676	0.0160	-0.0687	-0.1726	0.0990

The target gust front signature did cross over the Centralia sensors during the time period of 1610 to 1620 UTC, seen in Figure 4.2. $\overline{w}$ data from the ASP and BAU sensors each suggest that the signal passing over was a gust front. Both present the suspected vertical motion trend, with a local maximum followed by a decreasing trend. The peaks on the sensors match up with the signature on the 1616 UTC scan. The $\overline{w}$

plots can be seen for Centralia ASP and BAU on Figure 4.5, TKE can be found on Figure 4.6, and numerical $\overline{w}$ data on Table 4.2. The $\overline{w}$ plots suggest the updraft portion of the boundary was passing through at around 1613-1624 for ASP and 1615 for BAU. With the available divergence data using the 01.00 km it makes sense that the surface portion of the front would pass through earlier due to the front sloping back with height. There is also a rising trend in TKE around this time. However, there is a more well-defined rise-fall trend at around 1500 UTC (10:00 CDT) seen on both the $\overline{w}$ and TKE plots. It is likely that this earlier peak was caused by outflow from the thunderstorm well before it's arrival at 1615 UTC, but since there was no gust front signature in the general area of Centralia prior, it cannot be confirmed that it was a gust front at that time. But the trends on $\overline{w}$ and TKE are more favorable than the time of suspected passage.

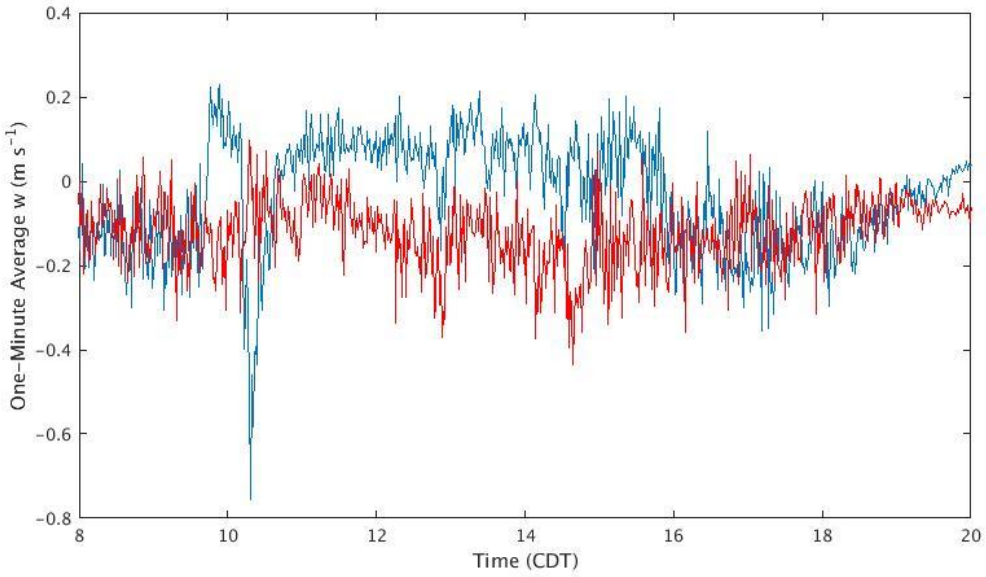

Figure 4.5: $\overline{w}$ data plot for Centralia ASP (red) and BAU (Blue) on 2016 07 06. Suspected crossing occurred at around 1613-1615 UTC (11:13-11:15 CDT).

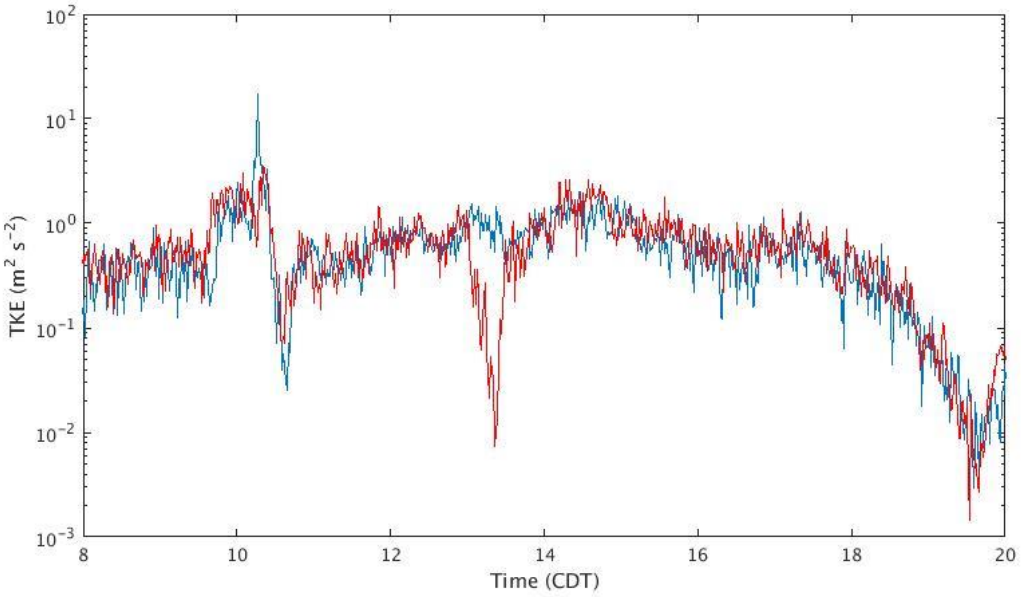

Figure 4.6: TKE plot for Centralia ASP (Red) and BAU (Blue) on 2016 07 06. As with Figure 4.5 the suspected gust front passage occurs at around 1615 UTC (11:15 CDT).

Table 4.2: Numerical $\overline{w}$ data for Centralia ASP and BAU on 2016 07 06 from 1611 to 1617 UTC.

	Time (UTC)	**1611**	**1612**	**1613**	**1614**	**1615**	**1616**	**1617**
Centralia ASP	$\overline{w}$ (m/s)	-0.0955	0.0069	0.0248	0.0418	-0.0209	-0.0360	0.0170
Centralia BAU	$\overline{w}$ (m/s)	0.0657	0.0875	0.0847	0.0723	0.1583	0.0727	0.0248

4.1.2 28 July 2016

On July 28th, 2016, a cluster of thunderstorms developed in northern Missouri. This cluster originally developed as part of a line of storms that developed in the upper Mississippi valley region. The group entered the MZZU operating range by 2030 UTC. The storms approached from the north and reached the Columbia city limits by 2110 UTC. A reflectivity thin line is first seen on MZZU at 2143 UTC as the reflectivity signature emerges from the cluster of thunderstorms. Due to the observation of the thin line, the out of storm (thin line) settings were used during this case. The lowest level of radar data available was 01.00 km for the divergence product.

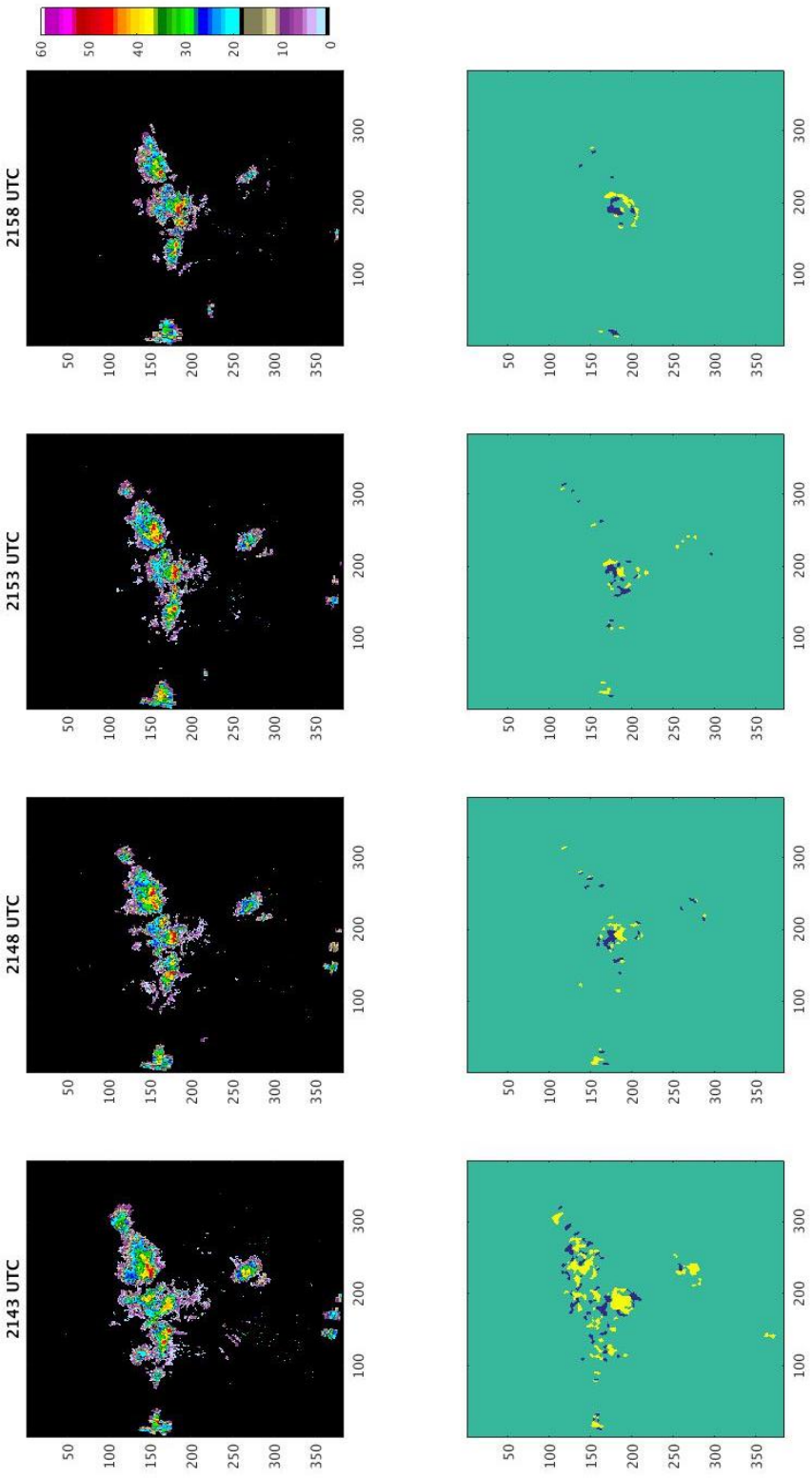

Figure 4.7: MZZU reflectivity and divergence on 2016 07 28 from 2143 to 2158 UTC.

Initially the gust front signature from the thin line is obscured by the noisy signal around MZZU. But a couplet of div-conv can be inferred on the northern side of the noise during the 2143 UTC divergence scan (Fig 4.7). As the signal crosses over the radar from 2148 UTC to 2158 UTC the signal changes from the div-conv pair into a purely linear convergence signal (Fig 4.7). This convergence line is fairly consistent temporally, as it keeps its general shape over the next three scans covering the period of 2158 to 2208 UTC (Fig 4.7 and 4.8). The convergence line across the signal remains spatially consistent with the thin line and the leading edge on the southeast side of the main thunderstorm on reflectivity, which can also be seen in Figure 4.7. Moving on to 2208 UTC, the convergence line begins to break apart as the thin line moves farther out ahead of the thunderstorm cluster (Fig 4.8). The signal is last seen during the 2214 UTC scan and is lost on the following scan at 2219 UTC for both reflectivity and divergence fields (Fig 4.8). There are two possible explanations for the loss of signal following the 2219 UTC scan. First, it is possible that the signal of the gust front is lost due to its height dropping below the lowest level as it enters the later stages of the gust front life cycle. The other possible cause is that the signal was lost due to the reflectivity falling below the display thresholds set by the WDSS processing. It's likely the later reason, as the feature can be inferred to still be present at the same level later in time, as there is the initiation of a new storm cell just ahead of the primary cluster at 2234-2239 UTC (Fig 4.9).

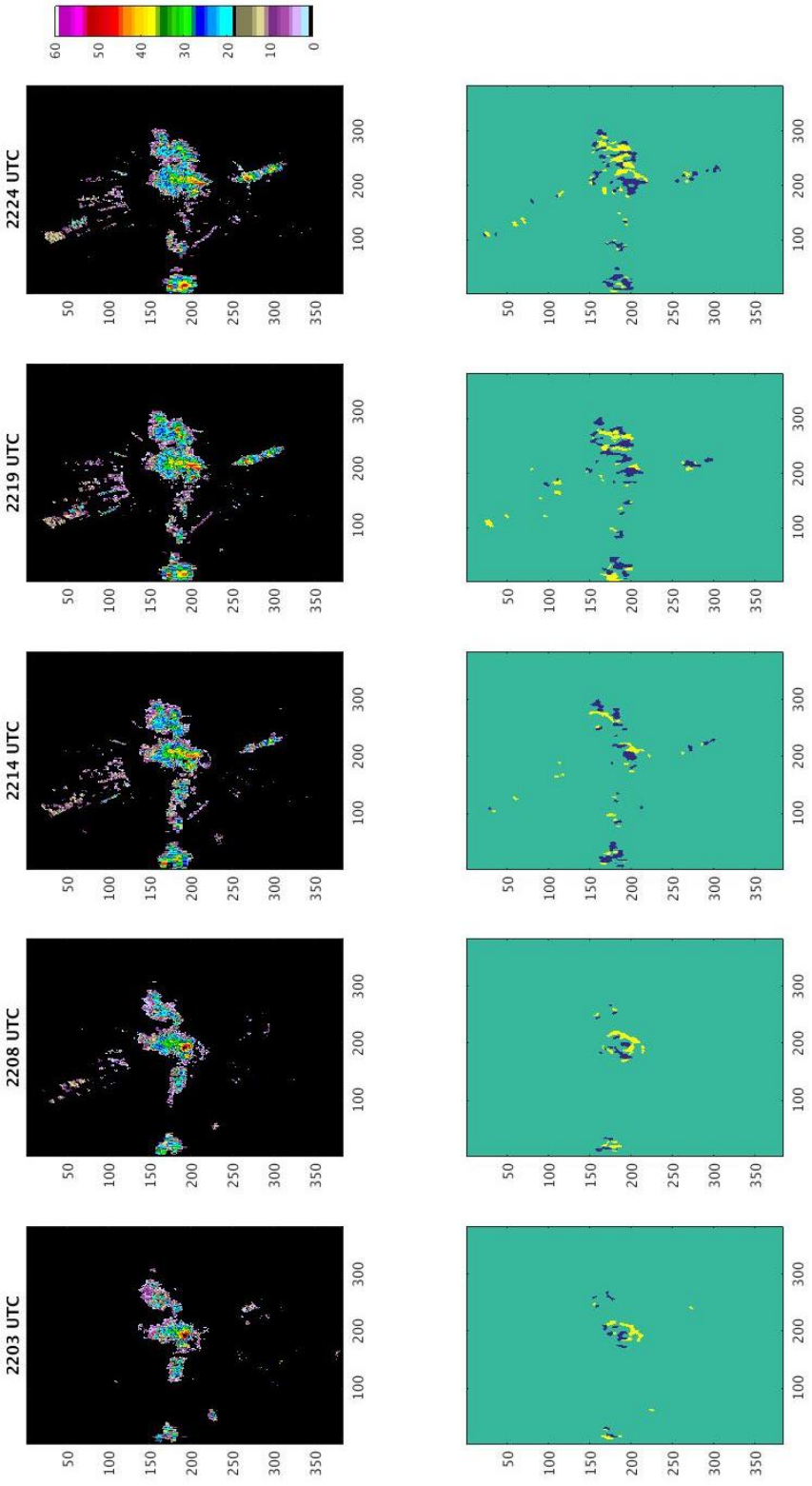

Figure 4.8: MZZU reflectivity and divergence on 2016 07 28 from 2203 to 2224 UTC.

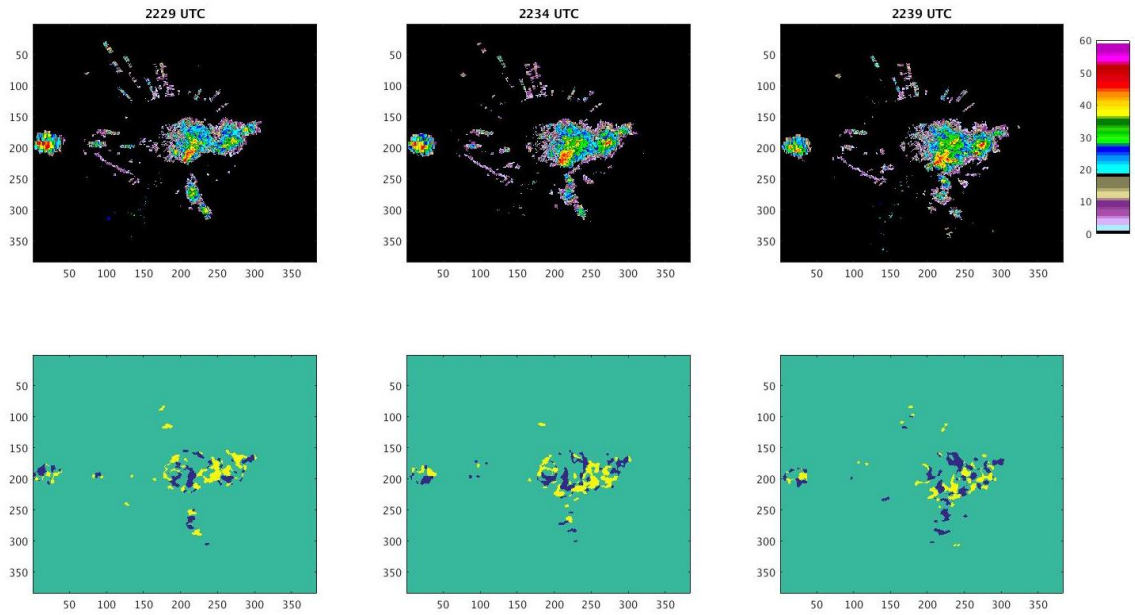

Figure 4.9: MZZU reflectivity and divergence on 2016 07 28 from 2229 to 2239 UTC.

The target thin line passed over the MOFLUX tower between 2214UTC and 2217 UTC, which can be seen in Figure 4.7. Primary and secondary $\overline{w}$ for MOFLUX shows a local peak in positive $\overline{w}$ followed by the expected decreasing trend (Fig 4.10, Table 4.3). The two data sets suggest that the gust front crossed over the site at around 2215 UTC with the peak in $\overline{w}$ followed by the expected decreasing trend following. There are other peaks in $\overline{w}$ before the target gust front signal crosses over. But, since there were no convergence signals that could be correlated with these peaks its likely that they were caused by other environmental effects such as local circulations from differential heating or thermals. The TKE plot (Fig 4.11) suggest that at the same time (2215 UTC) the TKE is on a secondary peak, where the maximum occurred during the period of 2100-2130 UTC, suggesting that the gust front crossed MOFLUX earlier. However, similar to the $\overline{w}$ data, since these peaks do not correlate to an earlier gust front

signature, it is not certain that these peaks in TKE were caused by an earlier gust front, or another source of turbulence during the daytime hours.

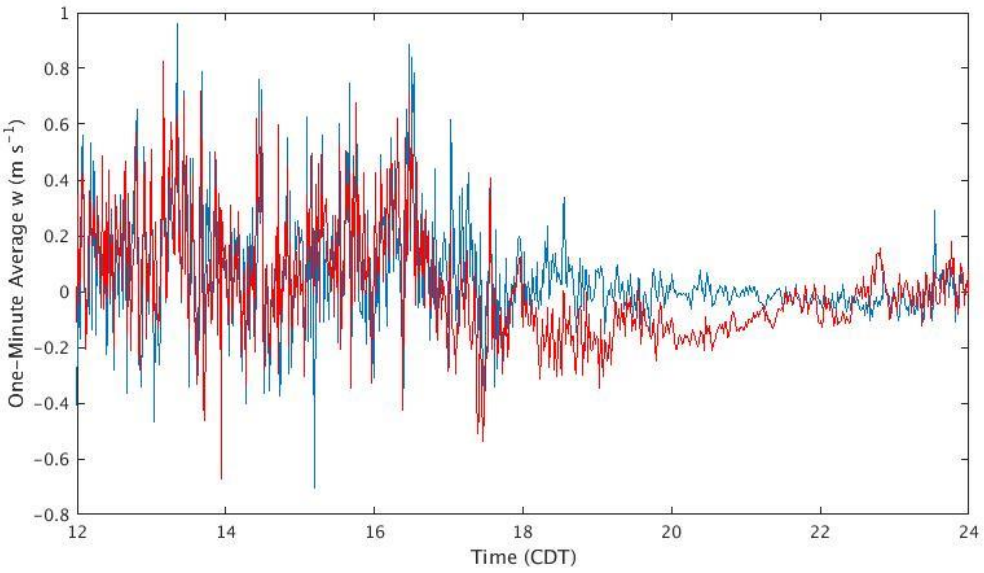

Figure 4.10: $\overline{w}$ data plot from MOFLUX Primary (Red) and Secondary (Blue) on 2016 07 28. Suspected gust front passage occurred at around 2215 UTC (17:15 CDT).

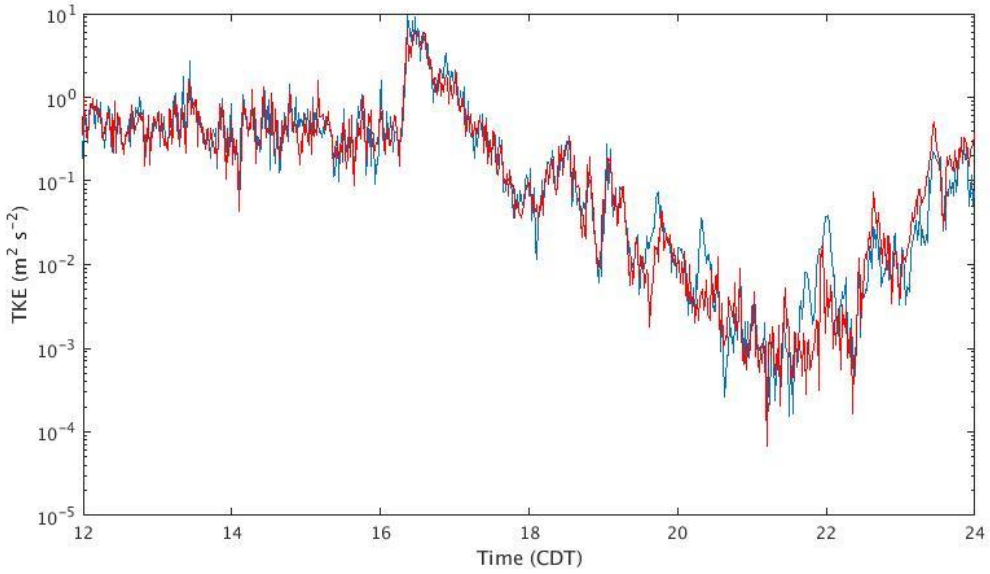

Figure 4.11: TKE plot for MOFLUX Primary (Red) and Secondary (Blue) on 2016 07 28. As with Figure 4.10 the suspected gust front passage occurs at around 2215 UTC (17:15 CDT).

Table 4.3: Numerical $\overline{w}$ data for MOFLUX on 2016 07 28 from 2212 to 2218 UTC.

	Time (UTC)	**2212**	**2213**	**2214**	**2215**	**2216**	**2217**	**2218**
MOFLUX Primary	$\overline{w}$ (m/s)	-0.0050	-0.1301	0.0785	0.1488	-0.0944	-0.1451	-0.2060
MOFLUX Secondary	$\overline{w}$ (m/s)	0.0296	-0.0296	0.2429	0.3461	0.4290	0.0554	0.2423

4.1.3 10 August 2016

During the afternoon of August 10th, 2016, another cluster of thunderstorms developed and moved into the region. These storms brought a burst of heavy rain to the area by spurring the development of pulse thunderstorms in the highly unstable atmosphere of the day. During this event a gust front was observed at MZZU by visualizing a reflectivity thin line prior to the rapid initiation of the heavily precipitating thunderstorm. Even though a thin line was observed ahead of the storms on reflectivity the in-storm settings were used during this case, as they were able to resolve the gust front signature. The lowest altitude available radar data was the 01.00 km data for both the reflectivity and divergence products.

Before the thin line was observed the suspected parent storms showed some interesting signals during the period from 2033 to 2100 UTC. While the blobs are not very consistent in their shape over time, they do exhibit some notable divergence-convergence pairs as they evolve over time (Fig 4.12). Three scans in particular can be seen with the storms just east-northeast of the radar at 2038 to 2048 UTC, seen in Figure 4.12.

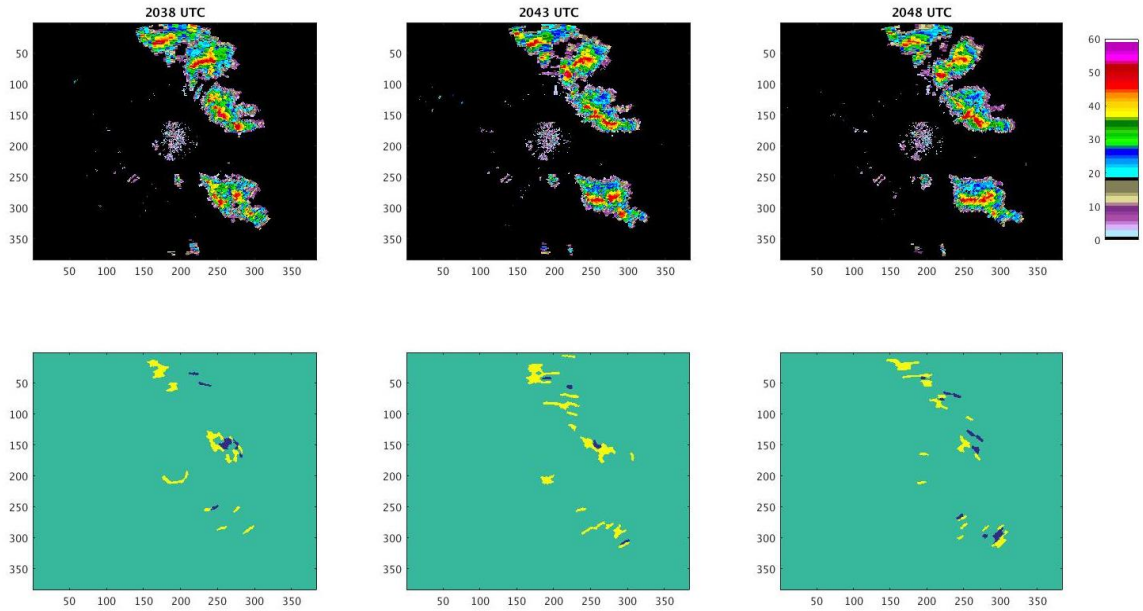

Figure 4.12: MZZU reflectivity and divergence on 2016 08 10 from 2038 UTC to 2048 UTC.

The Centralia ASP and BAU sensors both display a peak in $\overline{w}$ during the period between the scans. 2040 UTC for ASP and 2044 UTC for BAU (Fig 4.13, Table 4.4). These peaks are followed by the decreasing trend that would be expected with the passage of a gust front. Which suggests that an in-storm gust front is present at these times, possibly the source of the reflectivity thin line observed later in the event, prior to it moving out ahead of the thunderstorm. At 2040 UTC on the TKE plot for Centralia (Fig 4.14) there is a small peak just ahead of a decrease trend that lasts until approximately 2100 UTC, which would be caused by the precipitation following behind the possible gust front.

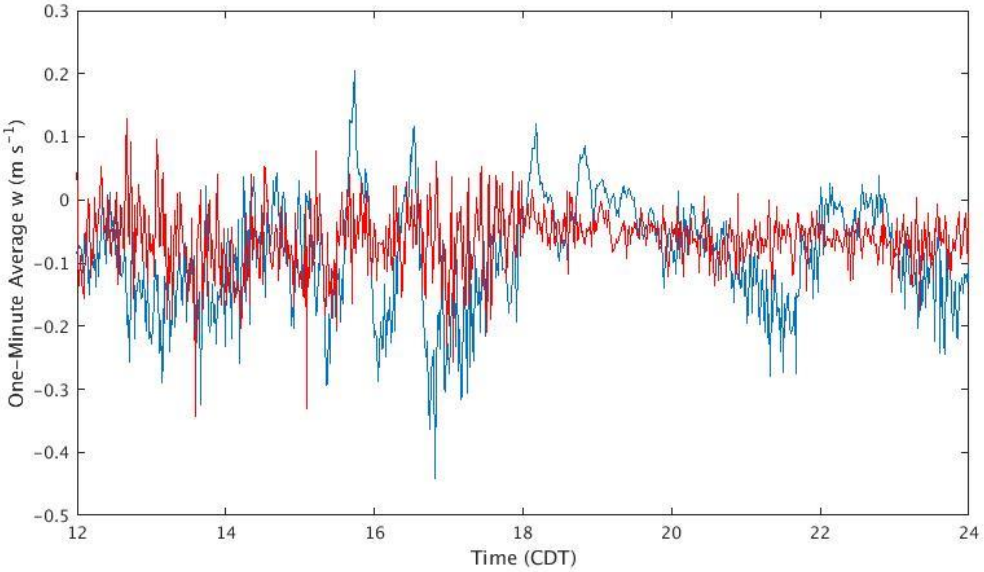

Figure 4.13: $\overline{w}$ data plot for Centralia ASP (red) and BAU (blue) on 2016 08 10. The suspected gust front within parent storm is associated with the peak in $\overline{w}$ at 2040 UTC (15:40 CDT).

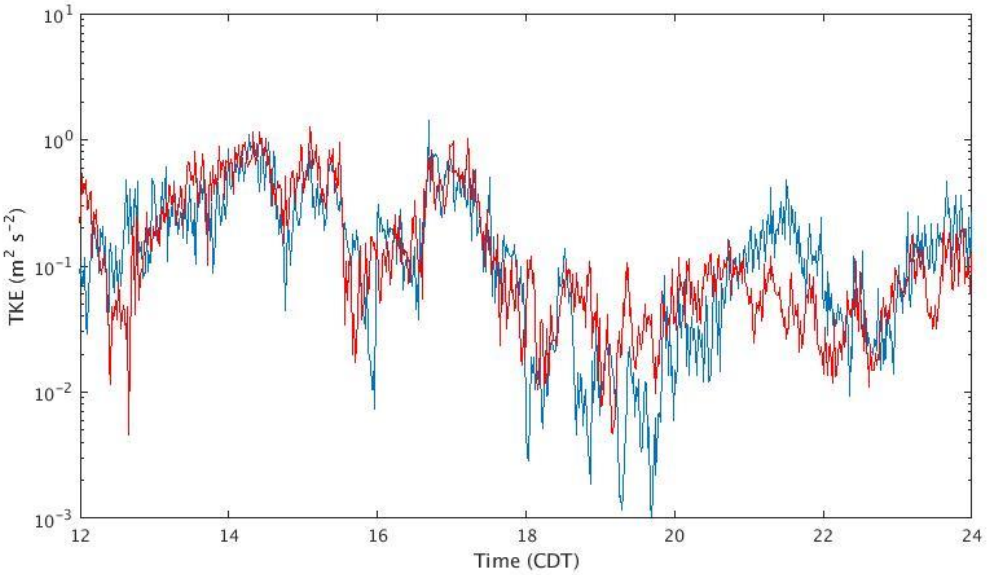

Figure 4.14: TKE plot for Centralia ASP (red) and BAU (blue) on 2016 08 10. As with Figure 4.13 the suspected gust front crossing occurs at 2040 UTC (15:40 CDT).

Table 4.4: Numerical $\overline{w}$ data for Centralia ASP and BAU on 2016 08 10 from 2038 to 2047 UTC. The times are staggered and separated to give a better look at the trends for each sensor.

	Time (UTC)	**2038**	**2039**	**2040**	**2041**	**2042**	**2043**	**2044**
Centralia ASP	$\overline{w}$ (m/s)	0.0154	-0.0575	0.0412	-0.0383	-0.1650	0.0105	-0.0697
	Time (UTC)	**2041**	**2042**	**2043**	**2044**	**2045**	**2046**	**2047**
Centralia BAU	$\overline{w}$ (m/s)	0.1232	0.1235	0.1705	0.2054	0.0995	0.0572	0.0397

As the thunderstorms move closer to MZZU and merge together, the target thin line can be seen on the reflectivity at 2117 UTC. Comparing to the divergence scans at 2118 UTC show a linear blob of convergence locate at the same position ahead of the storm (Fig. 4.15). As the thin line moves closer to the radar the linear convergence blob maintains spatial consistency until the radar scans at 2139-2158 UTC. The thin line is obscured on both reflectivity and divergence products due to the clutter around the radar, and the newly initiating convection (Fig 4.16). The thin line is visible again on the 2200 UTC scans (Fig 4.17). The linear convergence blob is spatially consistent with the thin line until the signals are lost again the 2225-2230 UTC scans. It is likely that the signal is lost again due to display thresholds from WDSS processing, or by being lower that the radar beam at the lowest level.

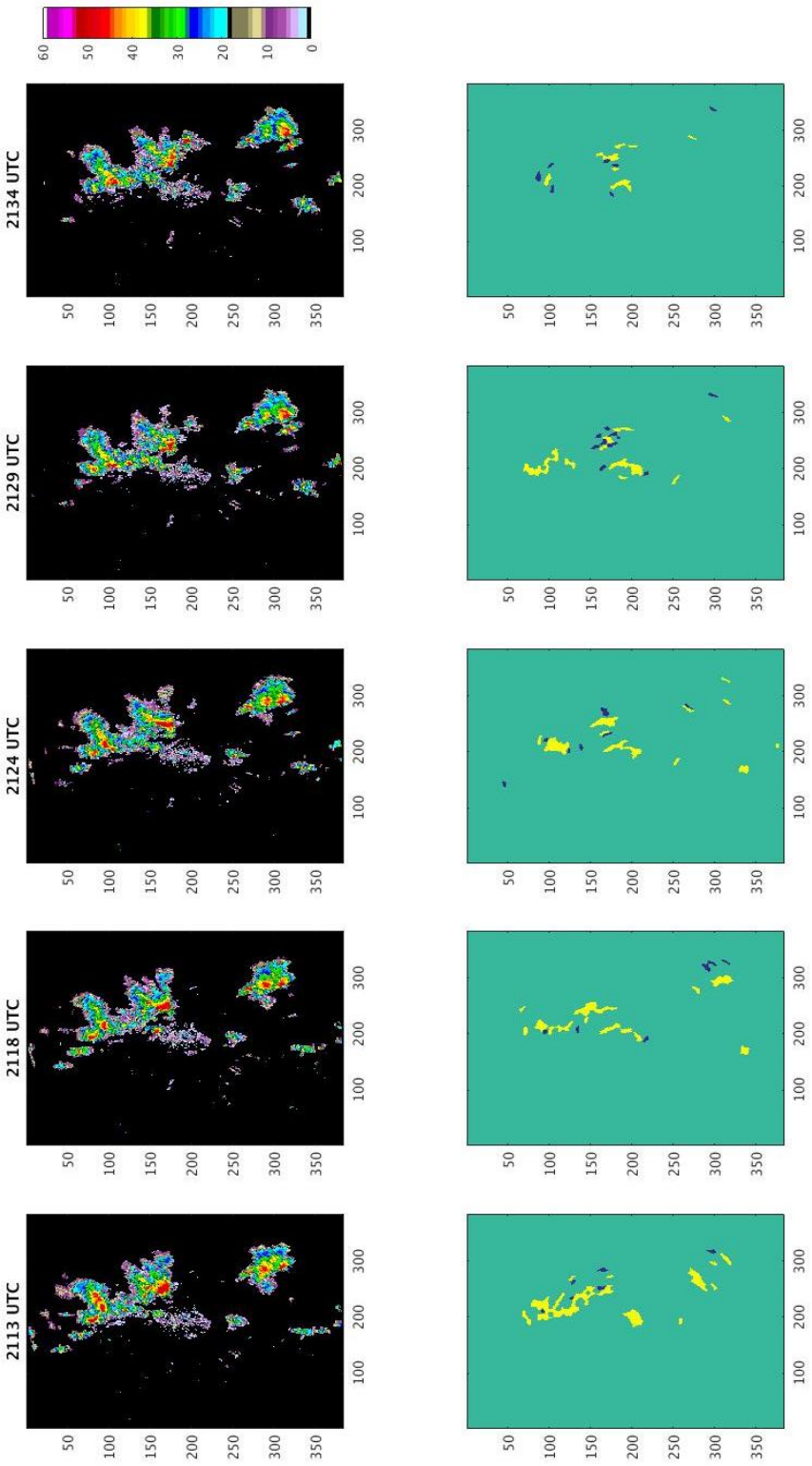

Figure 4.15: MZZU reflectivity and divergence on 2016 08 10 from 2113 to 2134 UTC.

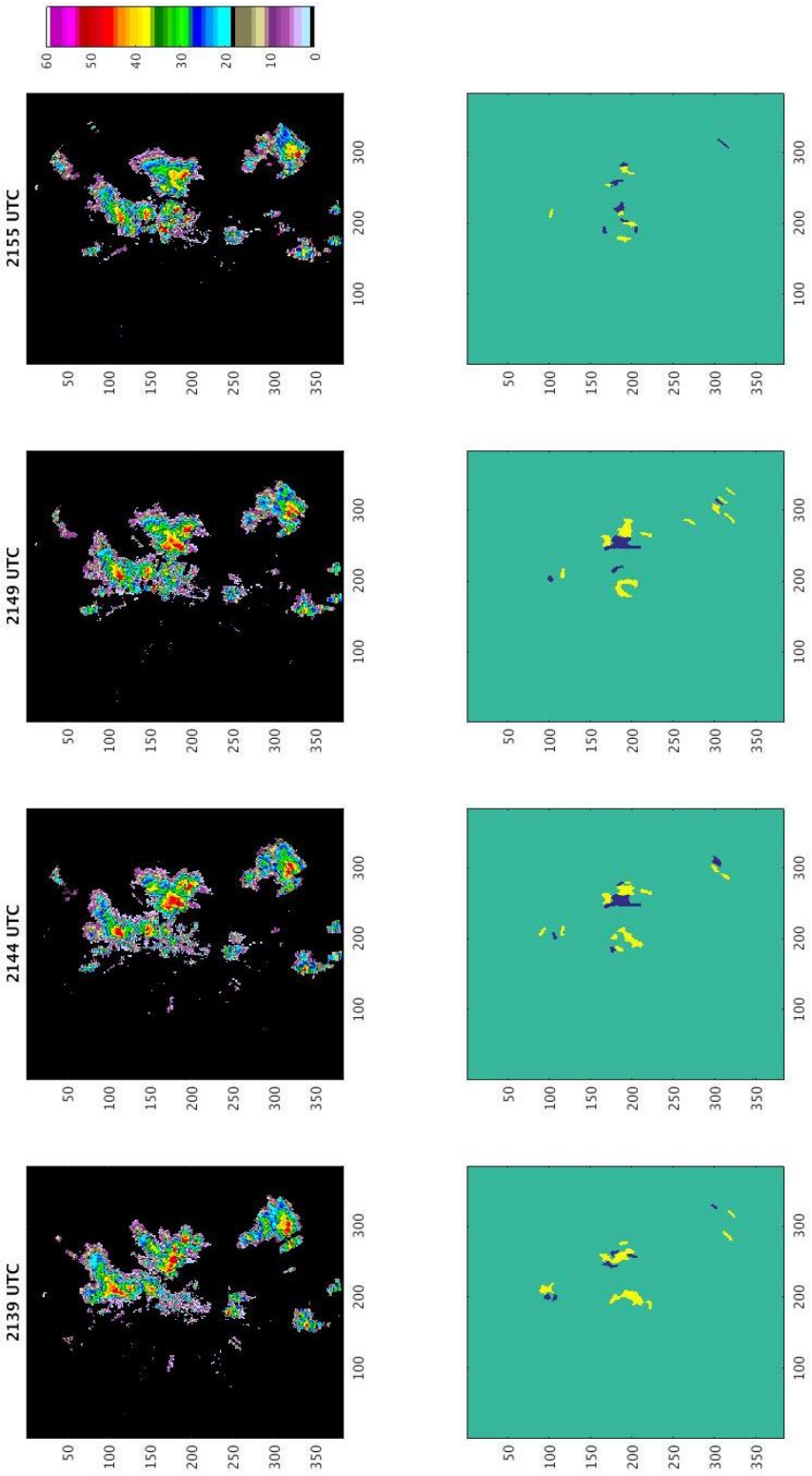

Figure 4.16: MZZU reflectivity and divergence on 2016 08 10 from 2139 to 2155 UTC.

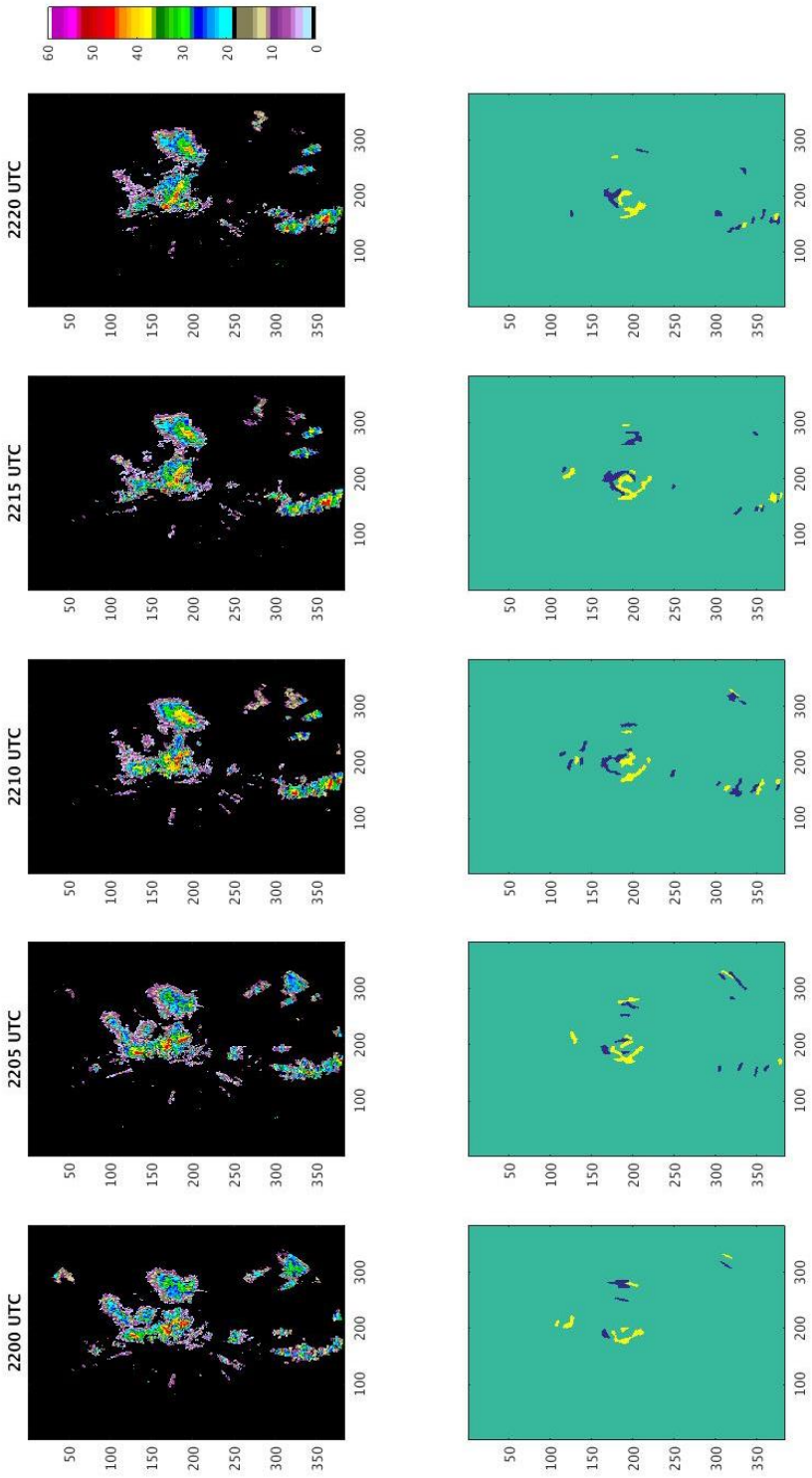

Figure 4.17: MZZU reflectivity and divergence on 2016 08 10 from 2200 to 2220 UTC.

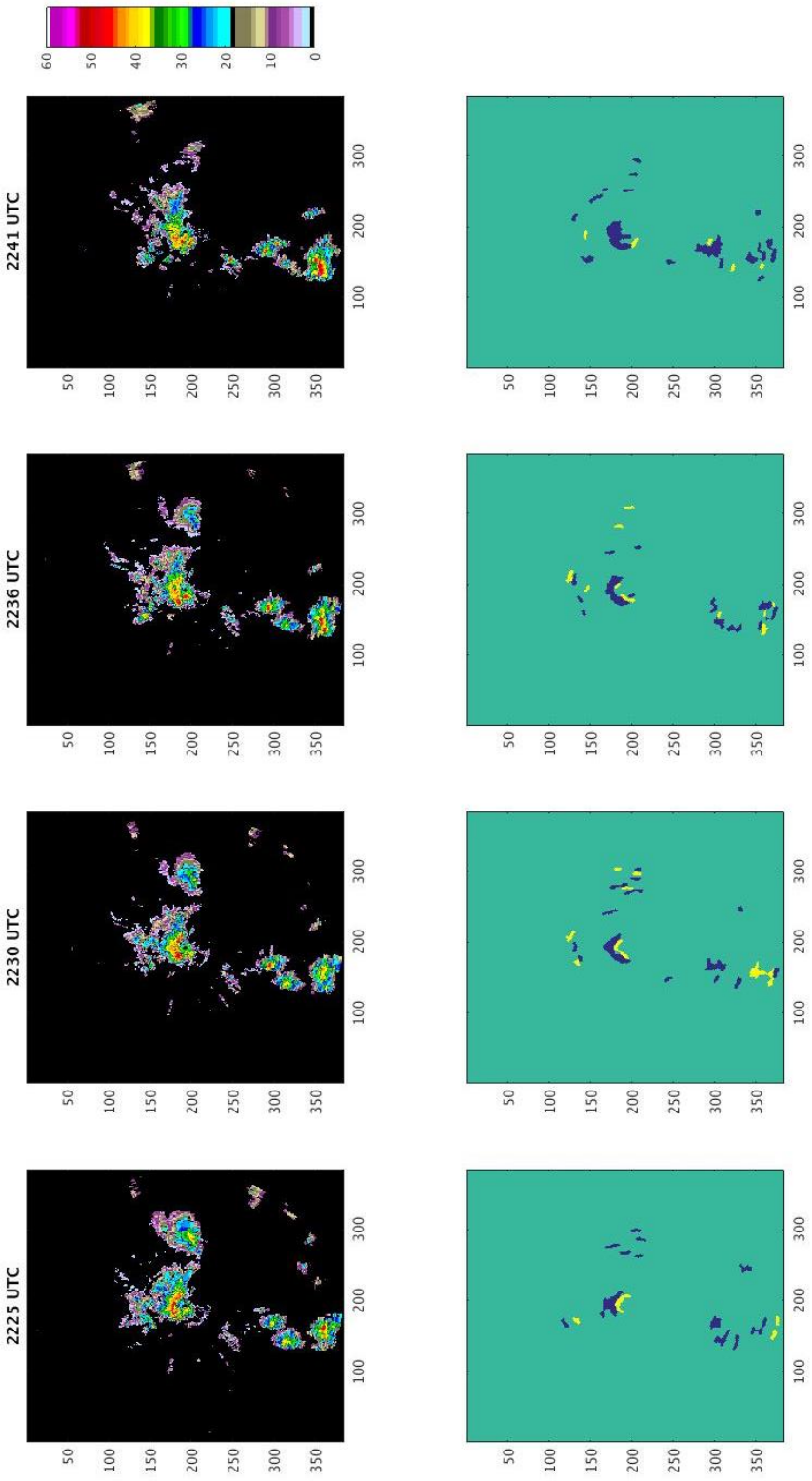

Figure 4.18: MZZU reflectivity and divergence on 2016 08 10 from 2225 to 2241 UTC.

The target thin line (gust front) crossed over the MOFLUX tower just before the signal loss during the 2225 UTC scan. Both primary and secondary data display a peak in positive $\overline{w}$ at around 2223 UTC, followed by a decreasing trend (Fig 4.19, Table 4.5). Which is around the same time as the arrival and passage of the gust front signature on the divergence product and the thin line on reflectivity. The peak associated with the convergence line is obscured on the $\overline{w}$ plot by other peaks likely caused by diabatic effects. This is also consistent on TKE plot for MOFLUX (Fig 4.20), where the TKE at around 2225 UTC displays a small peak just ahead of a decreasing trend. This peak is also on the downward side of the maximum TKE seen earlier around 2100 UTC (16:00 CDT), which was well before the target gust front signature approached MOFLUX. It is possible that there could have been earlier outflows that are the source of the turbulence. But, without convergence lines or divergence-convergence couplets, these influences cannot be confirmed with certainty to be additional outflow boundaries beyond the target at 2225 UTC.

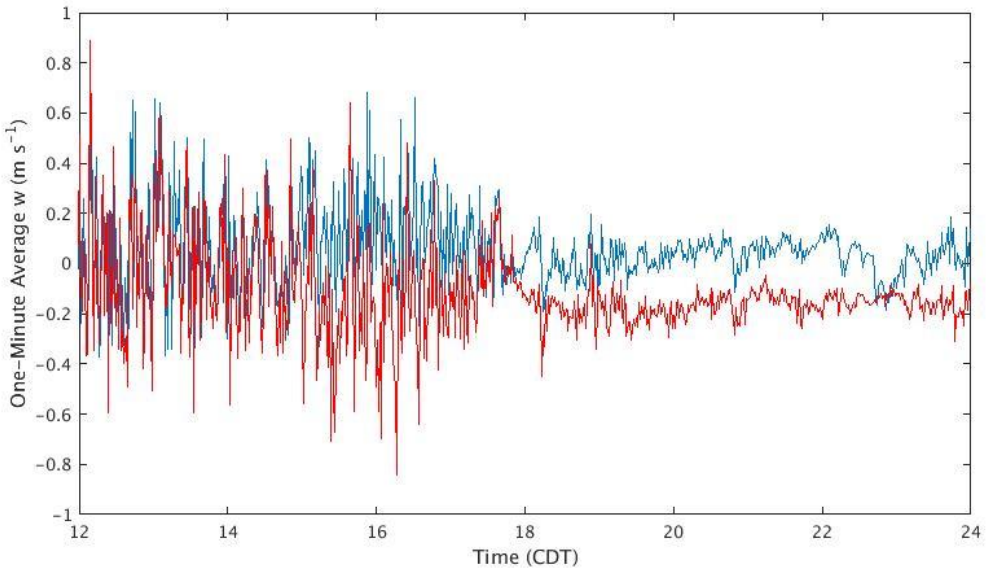

Figure 4.19: $\overline{w}$ plot for MOFLUX primary (red) and secondary (blue) on 2016 08 10. Suspected gust front crosses over by 2225 UTC (17:25 CDT).

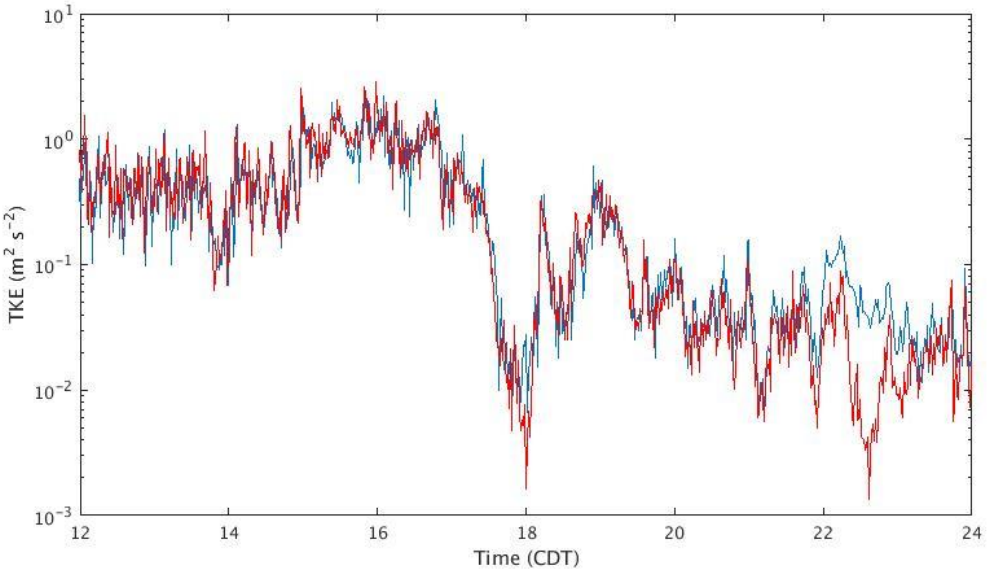

Figure 4.20: TKE plot for MOFLUX primary (red) and secondary (blue) on 2016 08 10. As with Figure 4.19 the suspected gust front crossing occurred by 2225 UTC (17:25 CDT).

Table 4.5: Numerical $\overline{w}$ data for MOFLUX on 2016 08 10 from 2221 to 2225 UTC.

	Time (UTC)	**2221**	**2222**	**2223**	**2224**	**2225**
MOFLUX Primary	$\overline{w}$ (m/s)	-0.2086	-0.0102	0.0720	-0.0940	-0.0975
MOFLUX Secondary	$\overline{w}$ (m/s)	-0.1376	-0.0318	0.3080	-0.0906	-0.0132

4.1.4 19 October 2016

The thunderstorms observed by MZZU on October 19th, 2016 were initiated by a stalled frontal boundary over southern Missouri. The system prompted severe weather warnings and reports in southern MO. North of the stationary front, storms did not prompt any reports of severe weather hazards. The convective mode of the storms during this event were single or multi-cell thunderstorms, moving in a system-wide line. The system movement was to the east-northeast, while individual cells followed their own discrete paths along the system. There were no thin lines observed on MZZU's reflectivity during the course of this event, so the MZZU in-storm settings were chosen for the analysis of this case. The lowest available levels for radar data were the 00.00 km level for both reflectivity and divergence fields.

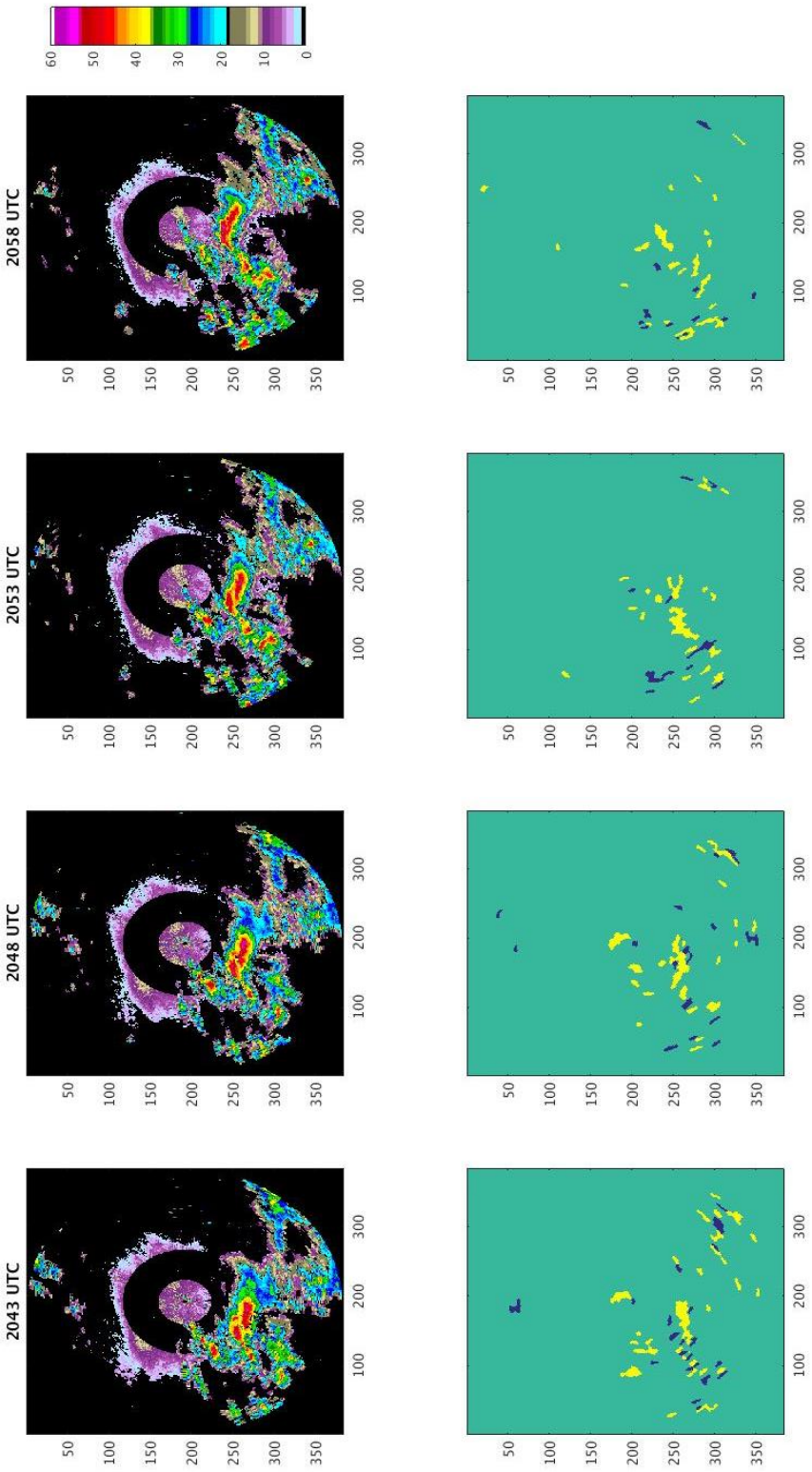

Figure 4.21: MZZU reflectivity and divergence on 2016 10 19 from 2043 to 2058 UTC.

The gust front signature that is the target for this case is suspected to be associated with the larger cell to the south of MZZU, roughly over Ashland, Missouri, starting at 2043 UTC (Fig 4.21). There is plenty of unwanted signal from the surrounding showers and storms at the time, but it's not difficult for user tracking while using the reflectivity as a reference. Moving to the next time steps the signal is the most temporally/spatially consistent between 2048 to 2058 UTC, but the signal keeps its position with the larger thunderstorm cell (Fig 4.21). The gust front signature on the divergence field begins to take a new track starting at the 2108 UTC scan. The front moves further due north on a direct path towards MZZU while the parent thunderstorm keeps moving on its northeast track (Fig 4.22). So, it is likely that at this point the gust front has broken away from the parent storm. As the gust front signature crosses over MZZU at 2113 to 2121 UTC it has a well-defined system of divergence-convergence pairing, this can be seen in a conv-div-conv formation from north to south (Fig 4.22).

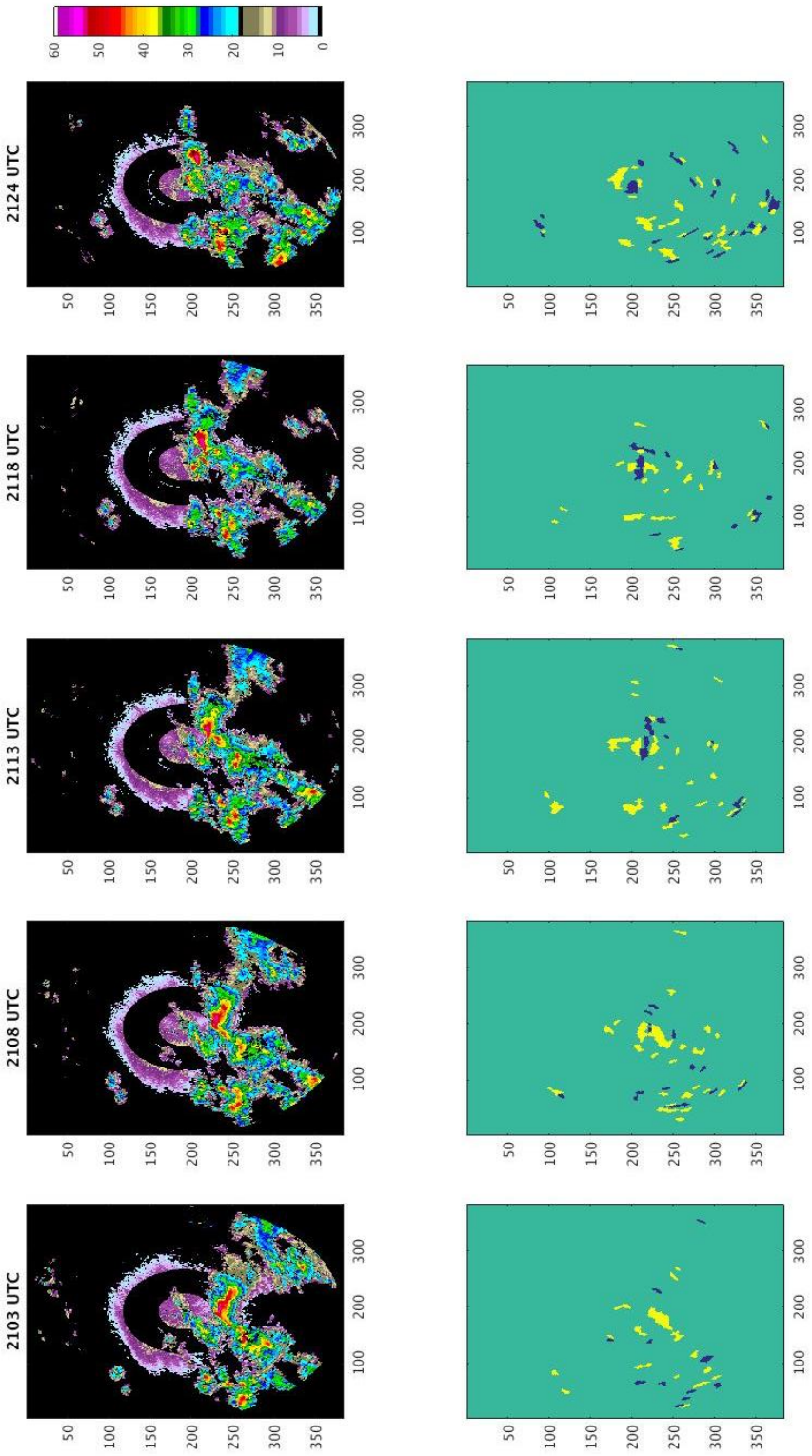

Figure 4.22: MZZU reflectivity and divergence on 2016 10 19 from 2103 to 2124 UTC.

After crossing the radar, the gust front signature shifts into a convergence line on the 2124 UTC scan. This form of the gust front is relatively consistent over the next few scans until the signal is lost at around 2139-2144 UTC (Fig 4.23). The gust front seems to have also spurred the development of some cells as it moved ahead of its parent thunderstorm during the period of 2113-2129 UTC, which can be seen in Figures 4.22 and 4.23.

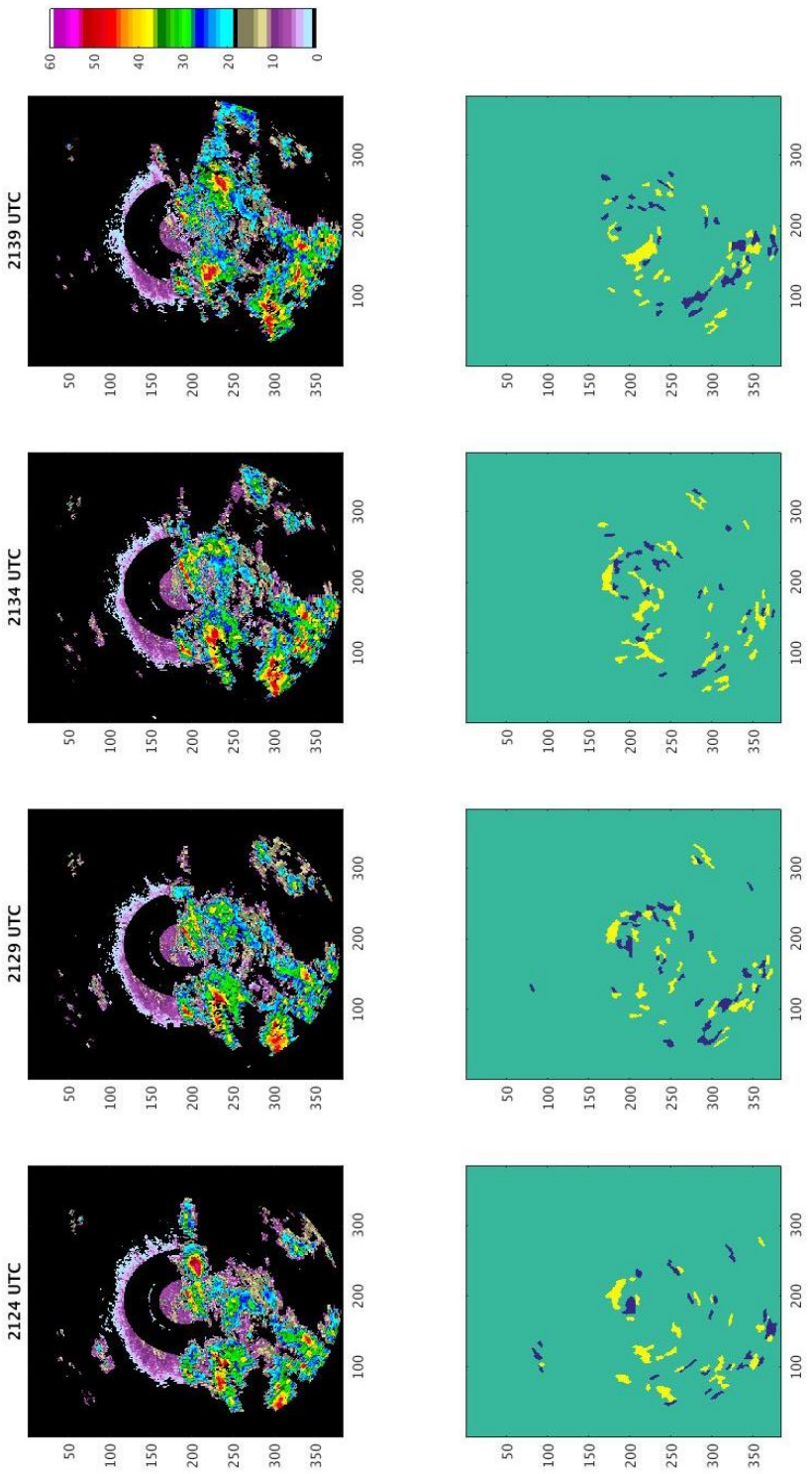

Figure 4.23: MZZU reflectivity and divergence on 2016 10 19 from 2124 UTC to 2139 UTC.

While the gust front signal did not cross over MOFLUX or the Centralia sites during the more defined stages of its visible life cycle, the suspected parent storm did cross over MOFLUX. This was during the period prior to the gust front outrunning the thunderstorm, early in the case period (2043-2108 UTC). Both MOFLUX primary and secondary data show a local peak in $\overline{w}$ at 2057 UTC, followed by the expected decreasing trend as the front passed and the precipitation moved in behind it. The data is presented in Figure 4.24 as well as Table 4.6. The data supports the idea that the leading edge of the storm crossing over at this time had an in-storm gust front, which can be correlated with the position of the convergence line on the 2058 UTC scan from Figure 4.21. This, in part with how the signal on the div product splits off from this storm ten minutes later, suggests that this was the gust front prior to outrunning the thunderstorm. TKE data for MOFLUX seen on the plot in Figure 4.25 shows that just prior to 2100 UTC the TKE was on a peak and is beginning to fall into a decreasing trend as the front moves away and precipitation sets in. As with the $\overline{w}$ plot, the peak in TKE that can be correlated with the convergence line is not clearly defined, with other peaks of similar value ahead of it in time. Though, given that there were multiple thunderstorm cells in the area, and the event is taking place in the late afternoon (1600 CDT), it is possible that the prior increase in TKE and $\overline{w}$ could be due to diabatic effects, or remnant outflows of other thunderstorms in the area.

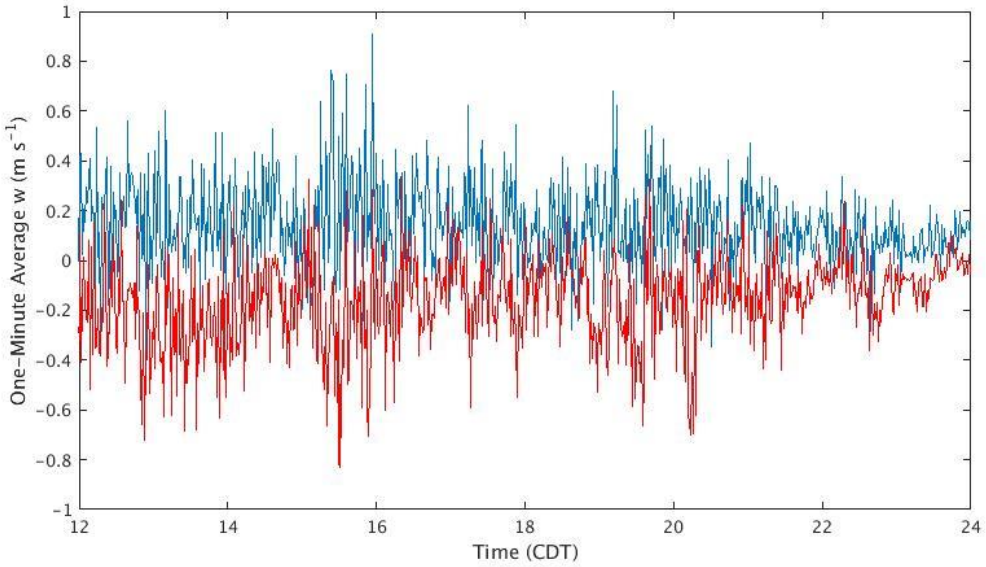

Figure 4.24: $\overline{w}$ plot for MOFLUX primary (red) and secondary (blue) on 2016 10 19. Suspected gust front crossing occurred at around 2057 UTC (15:57 CDT).

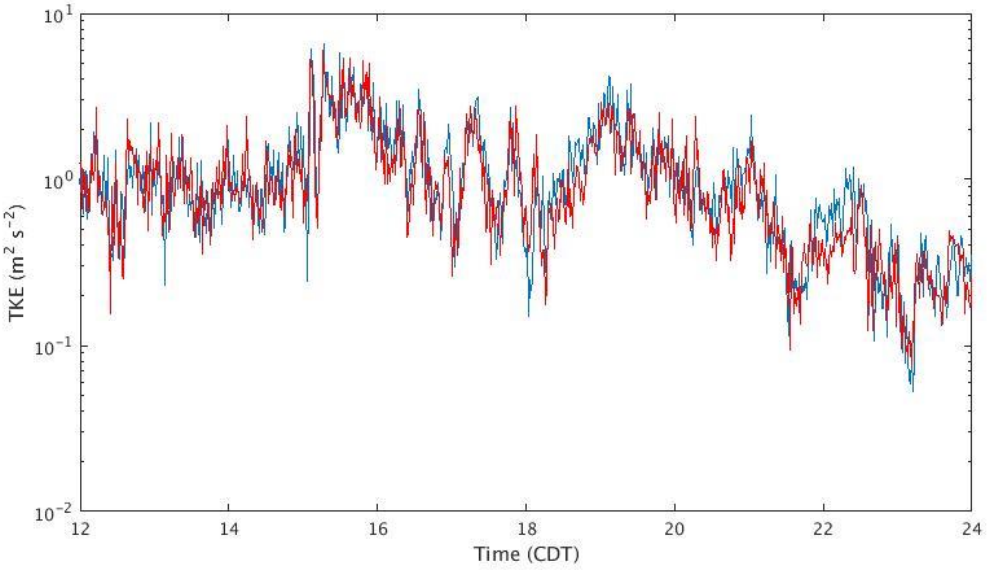

Figure 4.25: TKE plot for MOFLUX primary (red) and secondary (blue) on 2016 10 19. As with Figure 4.24 the suspected gust front crossing occurred at around 2057 UTC (15:57 CDT).

Table 4.6: Numerical $\overline{w}$ data for MOFLUX on 2016 10 19 from 2055 to 2100 UTC.

	Time (UTC)	**2055**	**2056**	**2057**	**2058**	**2059**	**2100**
MOFLUX Primary	$\overline{w}$ (m/s)	-0.4841	-0.3810	0.2818	-0.1926	-0.3175	0.0894
MOFLUX Secondary	$\overline{w}$ (m/s)	0.1892	0.0486	0.9064	0.3633	0.1507	0.4318

4.1.5 02 November 2016

November 2nd, 2016 saw multiple lines of thunderstorms develop in central Missouri. These storms initiated as individual cells and multi-cell storms, which merged over time into line formations. The storms discussed in this case initiated to the west of Columbia and moved into the region by 2140 UTC. There were two potential gust front signatures observed, each a separate section that would eventually merge into a line before crossing over MZZU. The potential gust front in the northern storms observed from 2140 to 2220UTC, and the southern portion from 2250-2320UTC. There was development ahead of the northern storms that was likely initiated by a gust front, though no thin line was observed on reflectivity. There was also no thin line observed later with the southern storm, so the MZZU in-storm settings were used for analysis. The lowest level of radar data available during this event was the 00.00 km level for both reflectivity and divergence products.

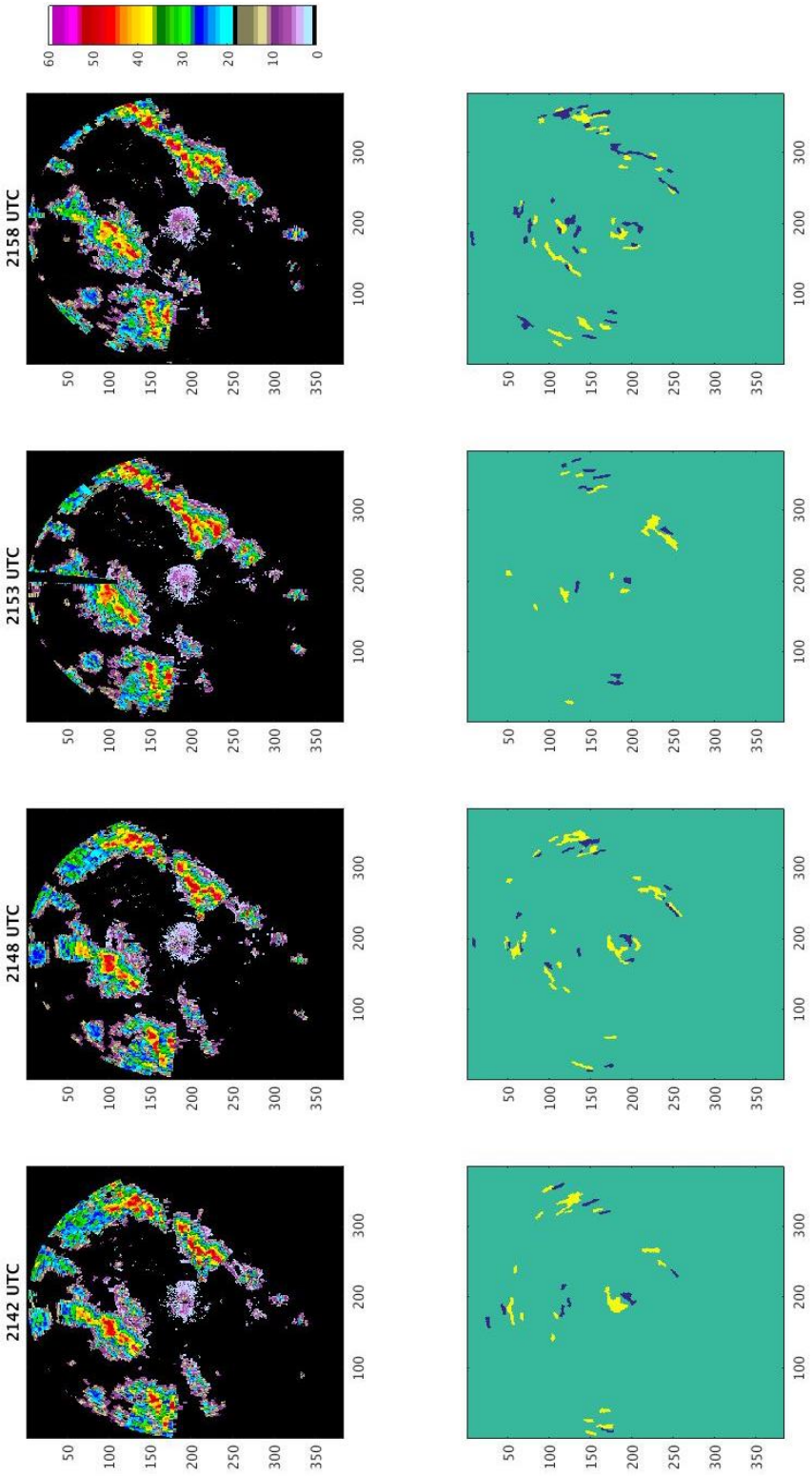

Figure 4.26: MZZU reflectivity and divergence on 2016 11 02 from 2142 to 2158 UTC.

The northern target was difficult to clearly observe on divergence during the period, due to the storm not moving directly towards MZZU. The CDAs (line features or div-conv pairs) were more north-south oriented than the east-west orientation for a storm moving from west to east, with a rather poor consistency over multiple radar scans (Fig 4.26). What signatures that are visible do line up relative to the leading edge of the northern storm, which can be seen on the 2158 UTC scan (Fig 4.26). The divergence scan at this time had a div-conv pair that was the optimal orientation, but this did not persist into the next scan (2203 UTC) as the newer precipitation feeds into the primary storm (Fig 4.27). This trend for more N-S orientation of div-conv signals is likely due to the movement of this storm. The storm is moving more parallel to the radar radials than perpendicular. This is consistent with what can be seen in Smith and Elmore (2004), and Uyeda and Znric (1985). Convergence on radar is apparent, best observed when a boundary is moving perpendicular to the radar radial, boundaries that move parallel to the radial do not display the signatures that normally can be attributed to them.

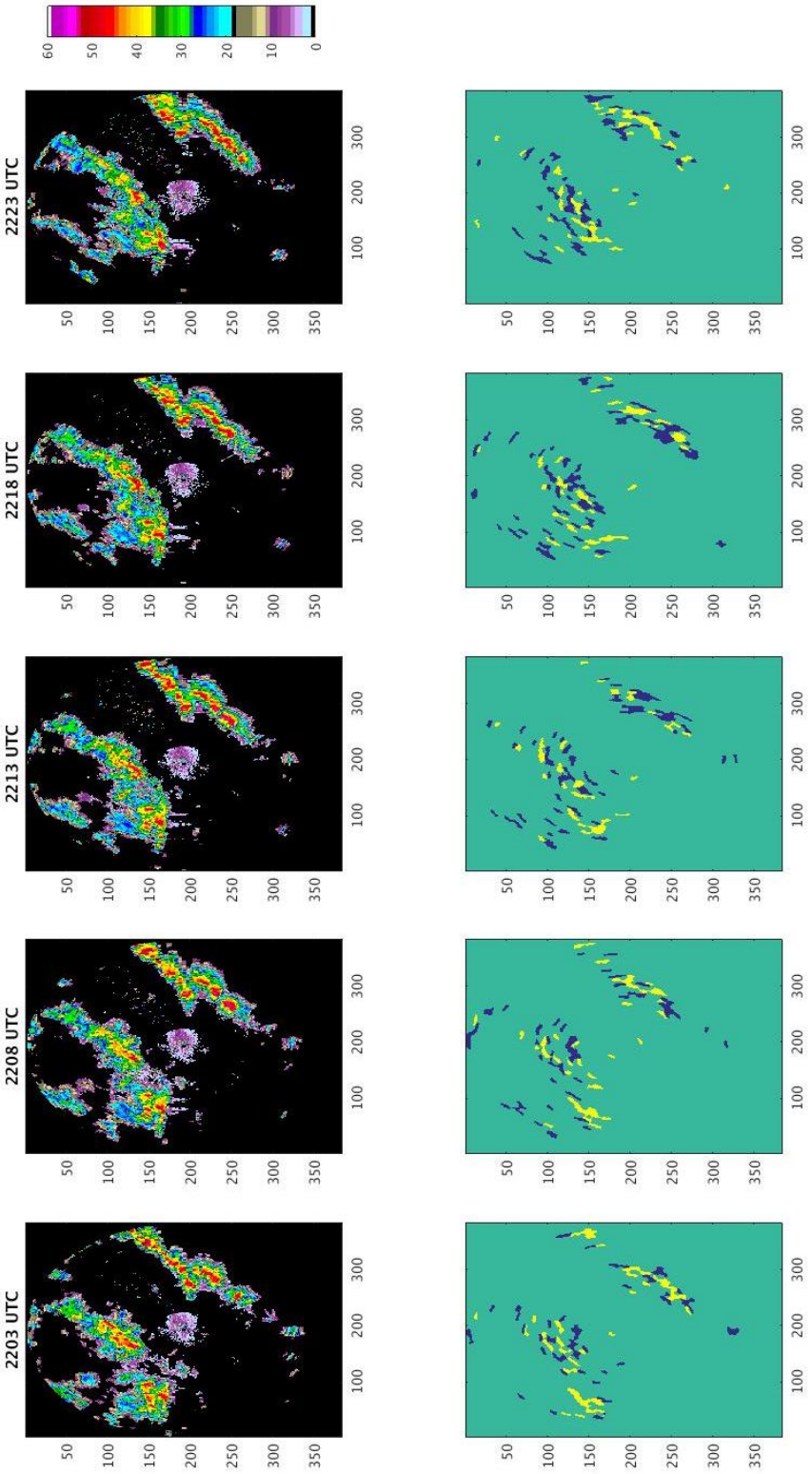

Figure 4.27: MZZU reflectivity and divergence on 2016 11 02 from 2203 to 2223 UTC.

This storm moved over Centralia ASP and BAU by 2220 UTC, when the precipitation echoes moved over the area to the north-northeast of Columbia. The time of interest of this site was twenty minutes earlier. Table 4.7, and Figure 4.28, depict the $\overline{w}$ trends during this time. The ASP sensor depicts the local peak at 2159 UTC, while BAU shows the peak at 2157 UTC. Both peaks are followed by the expected decreasing trend in $\overline{w}$. The peak in $\overline{w}$ is temporally aligned with the 2158 UTC divergence scan, suggesting that the CDAs forming a divergence-convergence pair seen on that scan is influencing the site, and is potentially a gust front despite the lack of consistency for this signal following the time period. TKE also suggests that the signature could possibly be a gust front. While it is on the lee side of a greater peak in TKE, there is a rise just prior to 2200 UTC, suggesting the turbulence is increasing due to the influence of a potential boundary (Fig 4.29). But also given that this increase is fairly low compared to the previous peak in TKE, the potential gust front is fairly weak. This in combination with the uncertainty of the signal due to lack of temporal consistency and the parallel movement to the radial, makes it difficult to determine if there is a real gust front at this time.

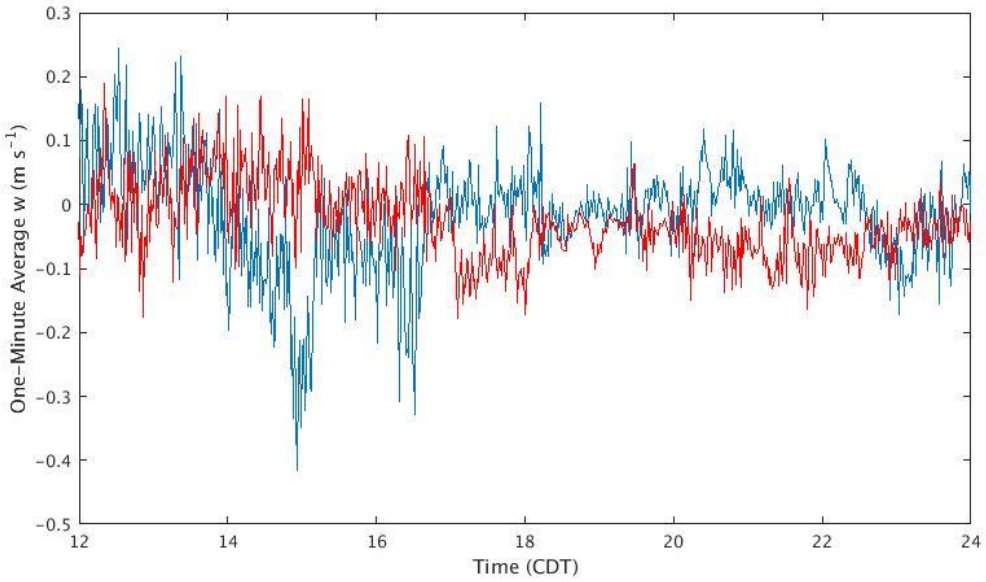

Figure 4.28: $\overline{w}$ plot for Centralia ASP (red) and BAU (blue) on 2016 11 02. Suspected gust front crossing occurred at around 2159 UTC (16:59 CDT).

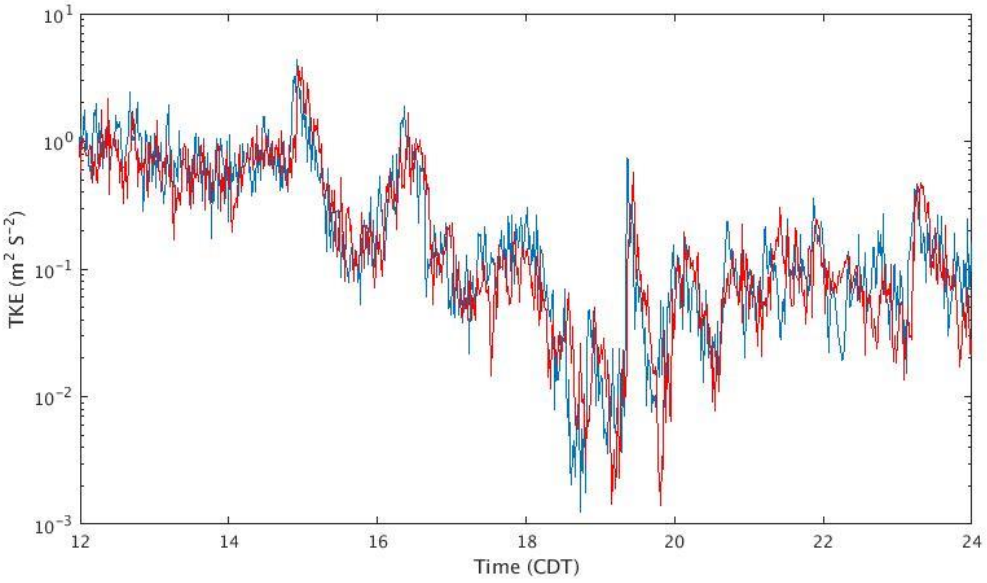

Figure 4.29: TKE plot for Centralia ASP (red) and BAU (blue) on 2016 11 02. As with Figure 4.28 the suspected gust front crossing occurred at around 2159 UTC (16:59 CDT).

Table 4.7: Numerical $\overline{w}$ data for Centralia ASP and BAU on 2016 11 02 from 2157 to 2203 UTC.

	Time (UTC)	**2157**	**2158**	**2159**	**2200**	**2201**	**2202**	**2203**
Centralia ASP	$\overline{w}$ (m/s)	-0.0094	0.0056	0.0153	0.0072	-0.0561	-0.0259	-0.0374
Centralia BAU	$\overline{w}$ (m/s)	0.0602	-0.0419	0.0242	-0.0433	0.0519	-0.0057	-0.0339

The southern of the two storms moves in a more favorable path relative to MZZU. Starting at 2233 UTC, the two storms at this time had now formed into a line, with showers filling the previous gap between the two storms. The target gust front signatures are associated with the leading edge of the storm, on the southern portion of the line (Fig 4.30). At 2254 the signal stabilizes into a div-conv pair, as well as the storm developing a hook-like echo visible on reflectivity (Fig 4.31). As the storm crosses over MZZU from 2259-2325 UTC, the pair remains consistent in time, even becoming more defined at 2304-2309 UTC (Fig 4.32). The gust front signature also remains consistent despite partial attenuation seen at 2319 UTC as the storm begins to overtake MZZU (Fig 4.32). The gust front signature changes to a convergence line after crossing over MZZU and heading away from the radar at 2325 UTC (Fig 4.32).

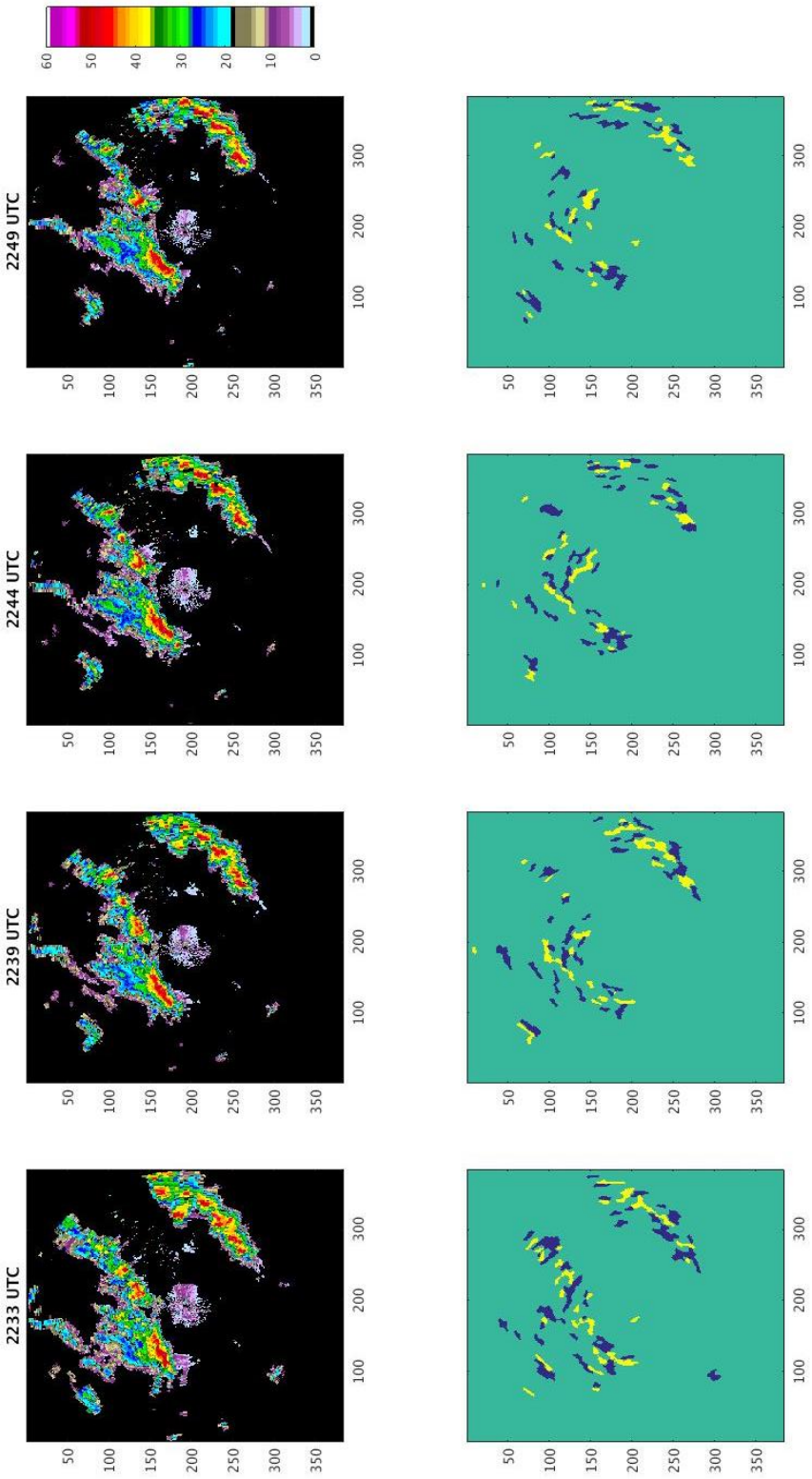

Figure 4.30: MZZU reflectivity and divergence on 2016 11 02 from 2233 to 2249 UTC.

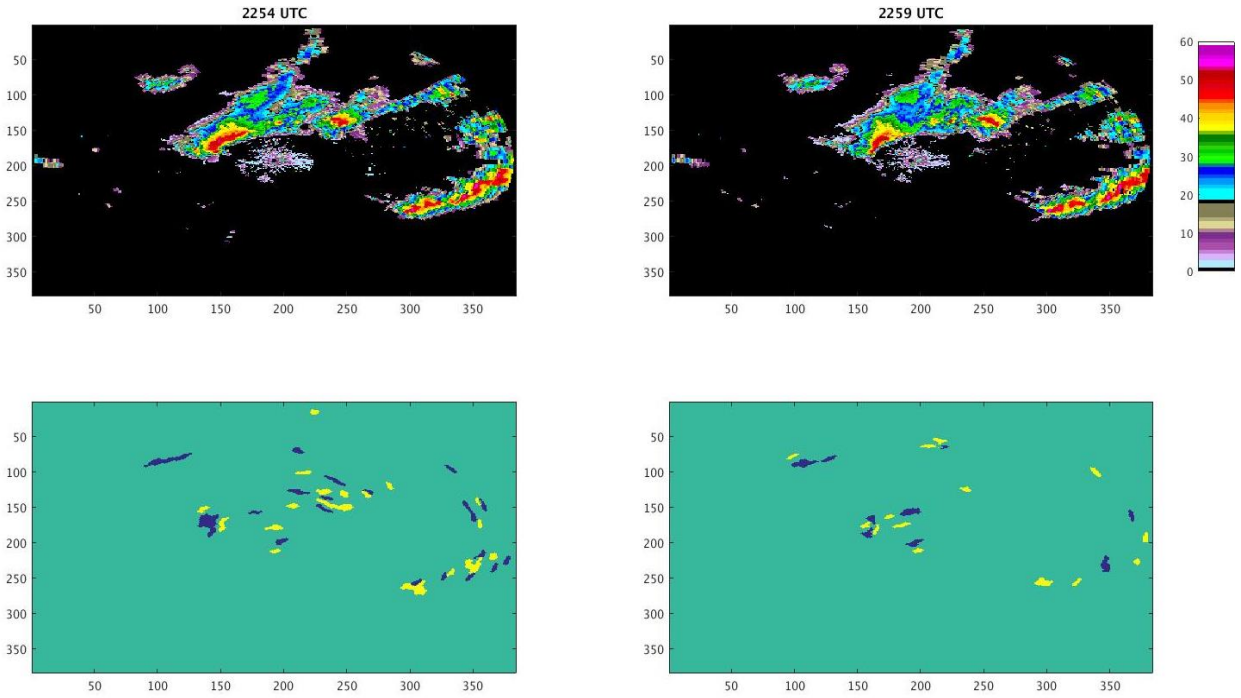

Figure 4.31: MZZU reflectivity and divergence on 2016 11 02 from 2254 to 2259 UTC.

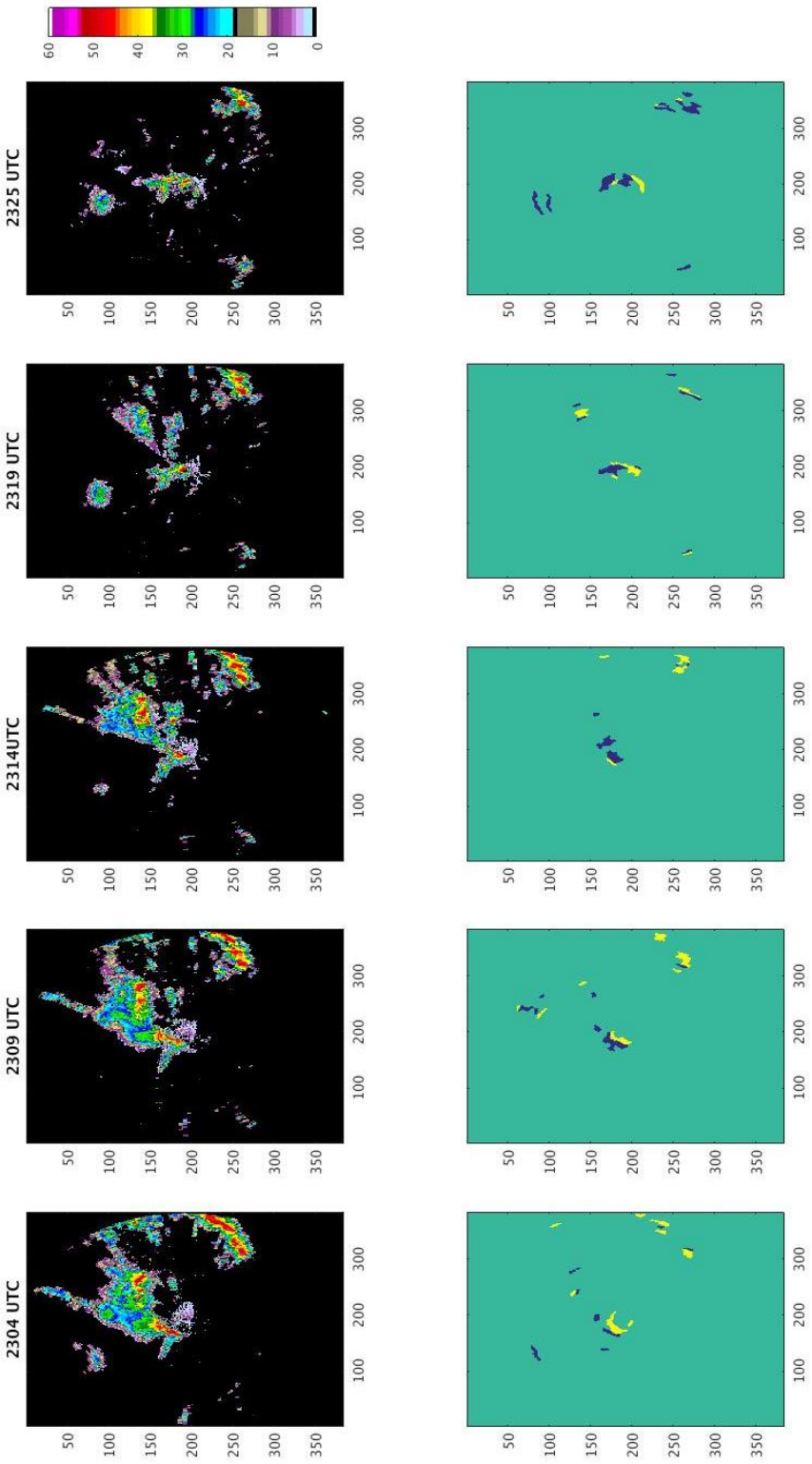

Figure 4.32: MZZU reflectivity and divergence on 2016 11 02 from 2304 to 2325 UTC.

Unfortunately, the gust front signature did not appear to cross over the MOFLUX site during the approach or following the crossing of MZZU. The suspected time of this interaction would have been around 2325-2335 UTC. According to MOFLUX primary and secondary $\overline{w}$, Figure 4.33 and Table 4.8, the local peak in $\overline{w}$ occurred at approximately 2300 UTC. TKE for MOFLUX (Fig 4.34) also heavily suggests that a gust front, or some form of outflow, crosses MOFLUX around that time given the prominent spike on the plot. But, since there are no gust front signatures in the approximate area of MOFLUX at the time, and there was no visible thin line to suggest the gust front was no longer in-storm, it cannot be concluded with certainty that these trends correlate to a gust front. In addition, due to the lack of support from $\overline{w}$ and TKE the signature seen with the southern storm on Figure 4.32, the gust front signature cannot be confirmed to be a successful detection of a gust front.

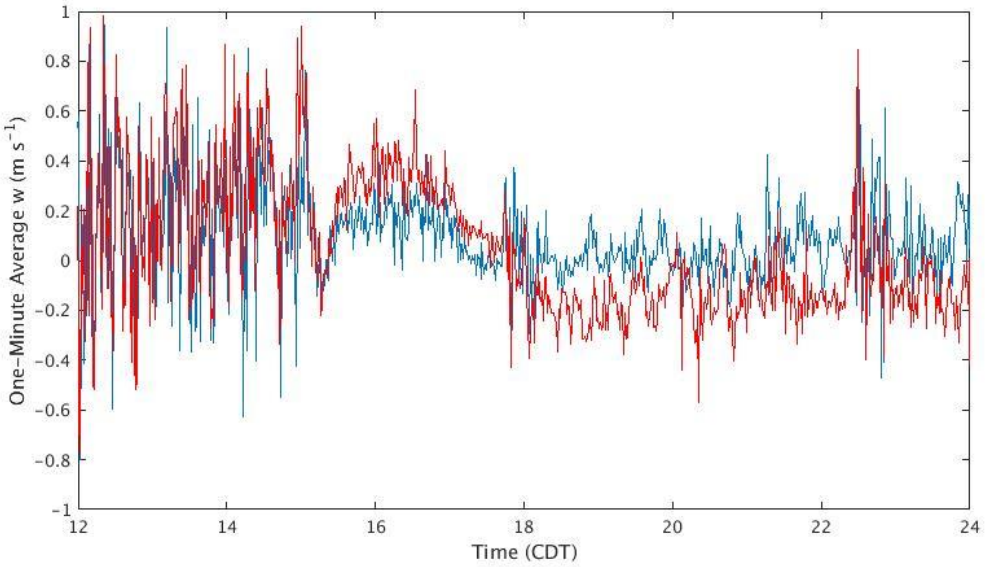

Figure 4.33: $\overline{w}$ plot for MOFLUX primary (red) and secondary (blue) on 2016 11 02.

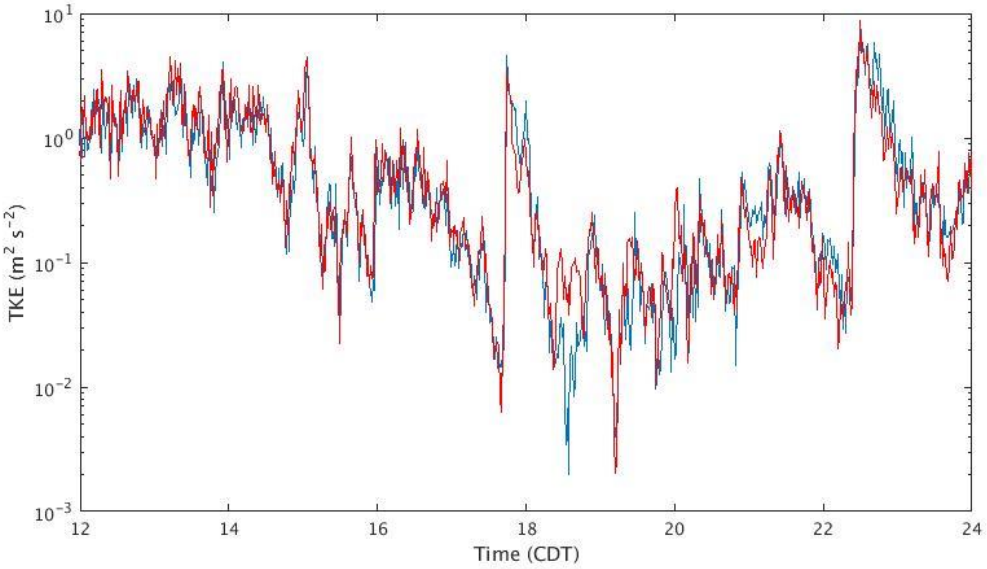

Figure 4.34: TKE plot for MOFLUX primary (red) and secondary (blue) on 2016 11 02.

Table 4.8: Numerical $\overline{w}$ data for MOFLUX on 2016 11 02 from 2257 to 2303 UTC.

	Time (UTC)	**2257**	**2258**	**2259**	**2300**	**2301**	**2302**	**2303**
MOFLUX Primary	$\overline{w}$ (m/s)	-0.111	-0.0801	0.0205	0.1715	0.0859	-0.1304	-0.2530
MOFLUX Secondary	$\overline{w}$ (m/s)	0.0193	0.1950	-0.1308	0.1671	0.0689	0.2208	0.0037

4.1.6 01 March 2017

During the evening of March 1st, 2017 (February 28th in CST), a QLCS moved through central Missouri. This storm system brought heavy rain, and some hail to the

Columbia area before breaking down into a line of cells before reaching the city limits. The storm moved in from the west, on a primarily east-southeast track as it slowly moved through central Missouri from 0300 to 0600 UTC. There was no thin line observed on reflectivity from MZZU during this event, so the in-storm settings were used for analysis. The lowest level of radar data available was the 00.00 km level for both reflectivity and divergence.

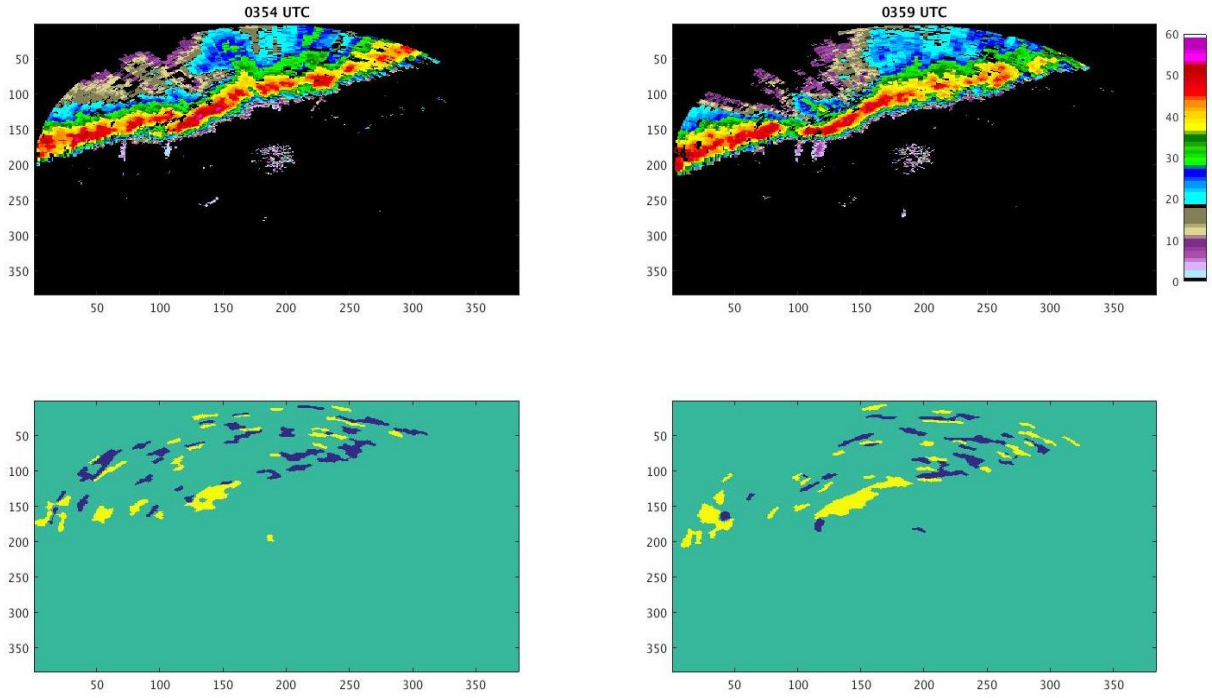

Figure 4.35: MZZU reflectivity and divergence on 2017 03 01 from 0354 to 0359 UTC.

The target for this event is the "central" section of the leading precipitation of the QLCS. This can be identified by the convergence line that correlates with the reflectivity. This can be seen with the reflectivity and divergence scans at 0359 UTC (Fig 4.35). As the line moves closer to Columbia over the 0404-0419 UTC period it remains consistent spatially and temporally, with some minor changes in the length and

thickness of the CDAs. At 0419 UTC, the northeastern length of the leading edge, that is due north and to the northeast of MZZU, show primarily divergence. In addition, this section of the line is also much more broken along the leading edge of the QLCS (Fig 4.36). This section persists along with the main target section over the next several scans. The broken arrangement in the line to the north and northeast of the radar is primarily caused by these sections of the line moving parallel to the radial. Despite this the shape of the front can still be inferred, at least by user observation. Moving into 0435 UTC the line breaks further and the line organization deteriorates, breaking apart by 0450 UTC (Fig 4.38).

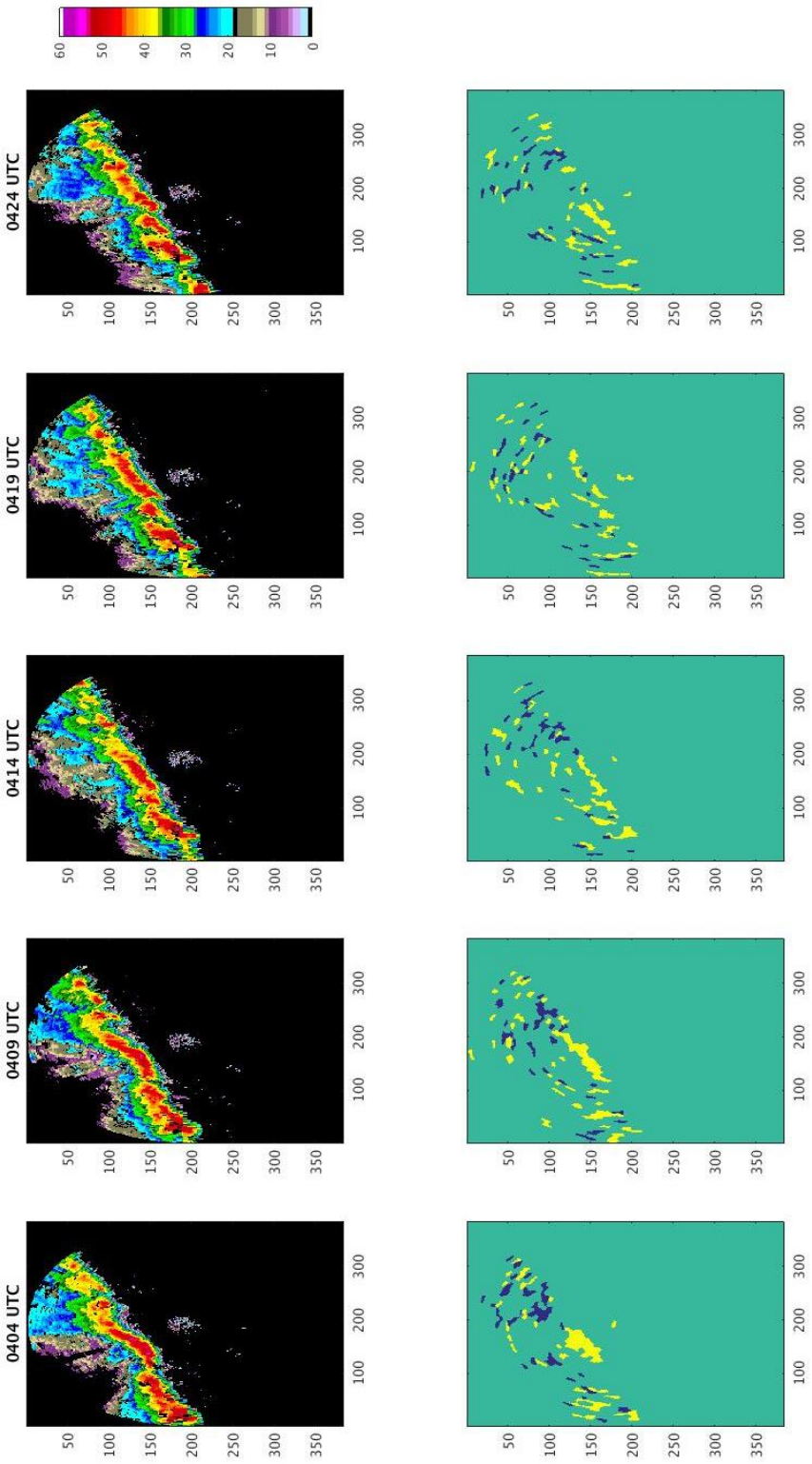

Figure 4.36: MZZU reflectivity and divergence on 2017 03 01 from 0404 to 0424 UTC.

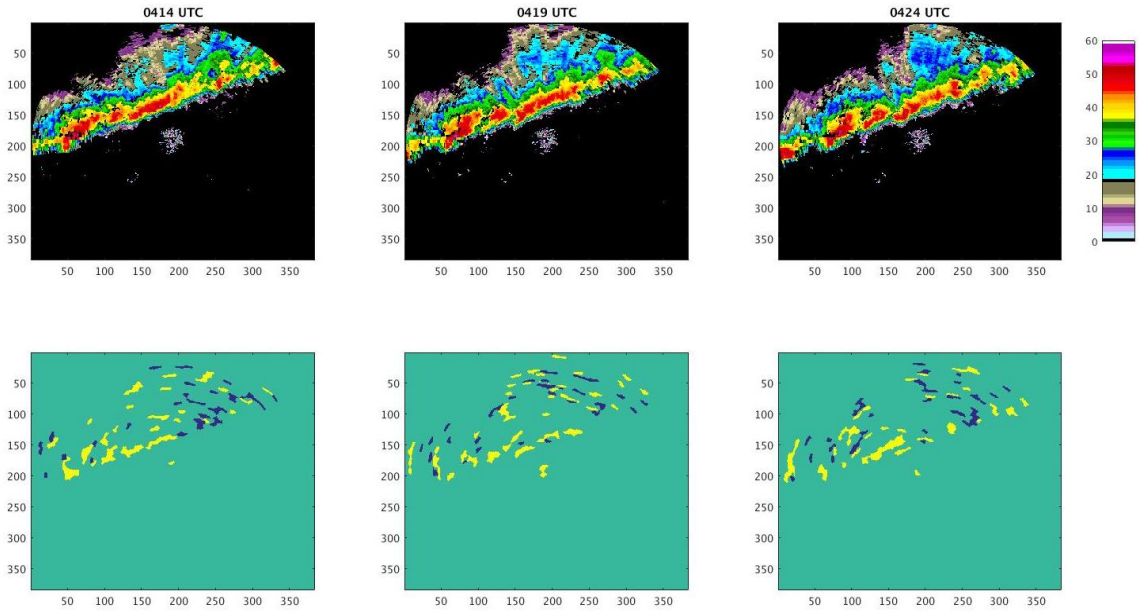

Figure 4.37: MZZU reflectivity and divergence on 2017 03 01 from 0414 to 0424 UTC.

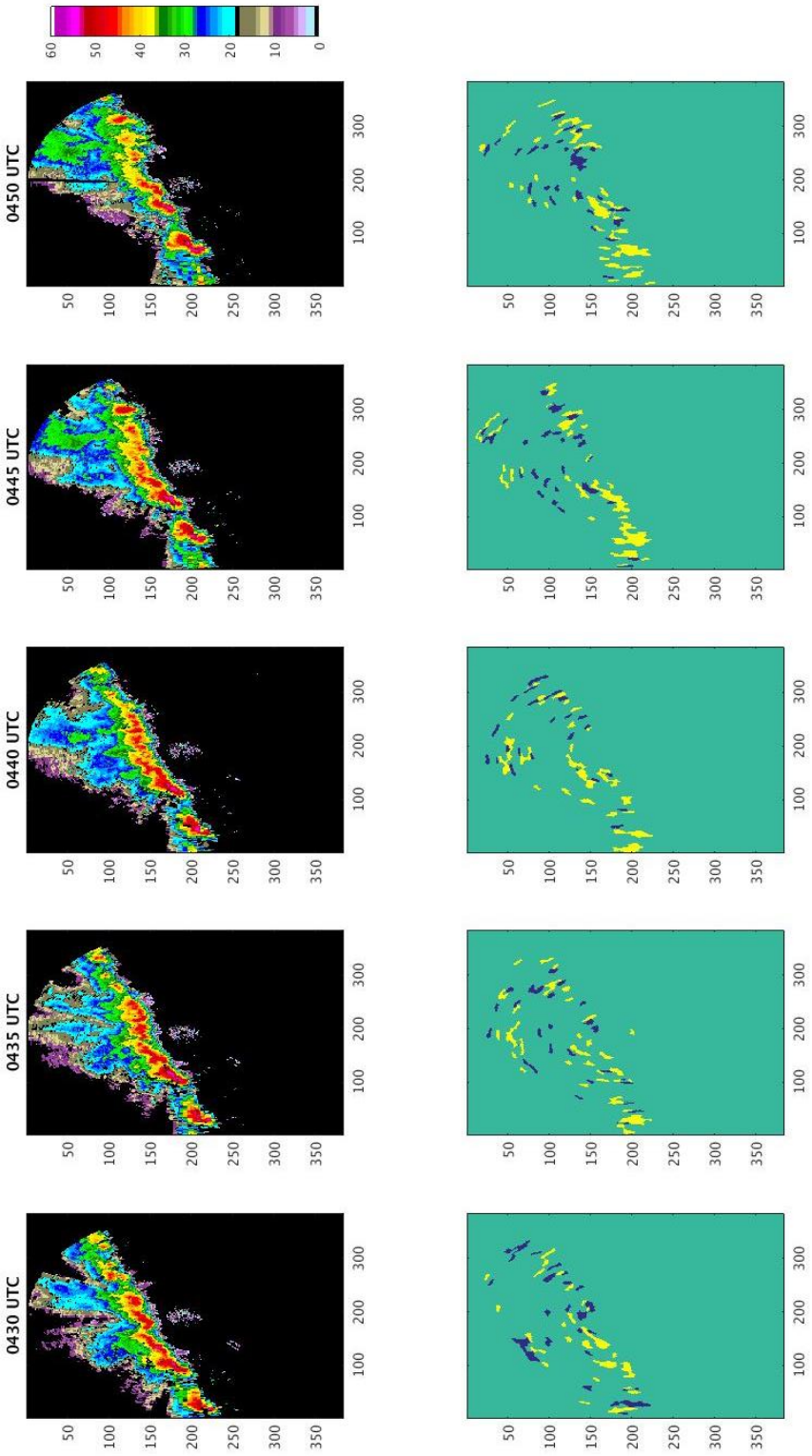

Figure 4.38: MZZU reflectivity and divergence on 2017 03 01 from 0430 to 0450 UTC.

The line does cross over the Centralia sites before it breaks at 0450 UTC. The time of the crossover is around 0410 – 0420 UTC, when the precipitation reaches ASP (Figure 4.37). The $\overline{w}$ data can be seen in Figure 4.39 And Table 4.9. There is a local peak in $\overline{w}$ just prior to the onset of precipitation at around 0415 UTC on both ASP and BAU, with expected decreasing $\overline{w}$ trend following, suggesting that the sensors are detecting a gust front at the leading edge of the precipitation. TKE, Figure 4.38, also shows a rise-peak that correlates with the $\overline{w}$ trends in time, also suggesting gust front passage. Suggesting that the convergence crossing over around 0415 UTC is a succesful gust front detection. However, the same trends can be seen approximately 30 minutes earlier on $\overline{w}$ and TKE, at just after 0350 UTC. Since this event occurs during the late evening (around 10:00pm CST), it is unlikely that this was caused by diabatic effects. It is possible that another gust front could have be ahead of the precipitation at that time and the $\overline{w}$ trend at 0415 UTC could be a secondary surge. The lack of a thin line on the reflectivity, or a signature on the divergence product, to correlate with the peaks means that a gust front cannot be confirmed with certainty for 0350 UTC. But, the correlating rises in $\overline{w}$ and TKE suggest the presence of a gust front at that time.

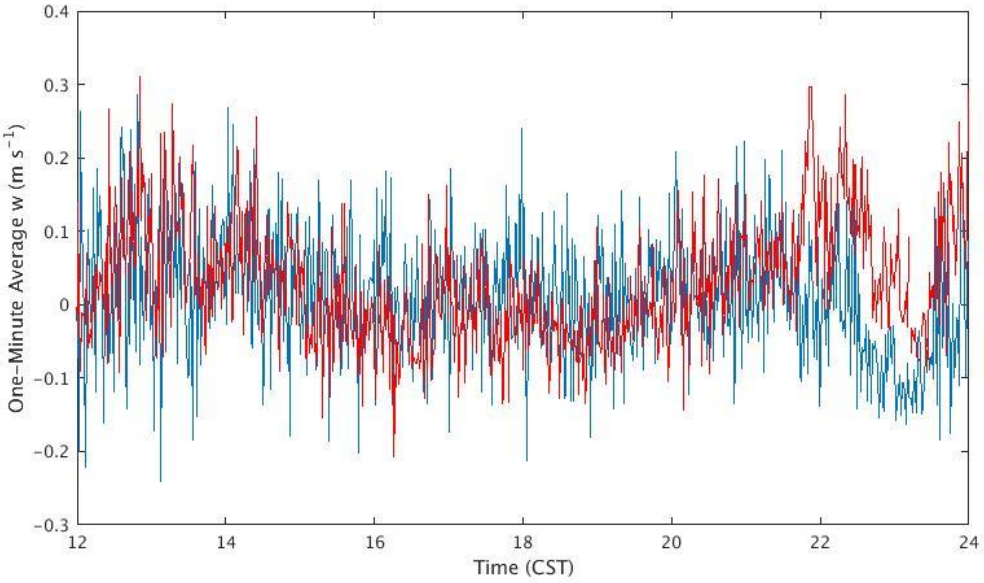

Figure 4.39: $\overline{w}$ plot for Centralia ASP (red) and BAU (blue) on 2017 03 01. Suspected gust front crossing occurred at 0416 UTC (22:16 CST 02/28). However, there is another peak 30-minutes earlier around 0350 UTC that could be another gust front.

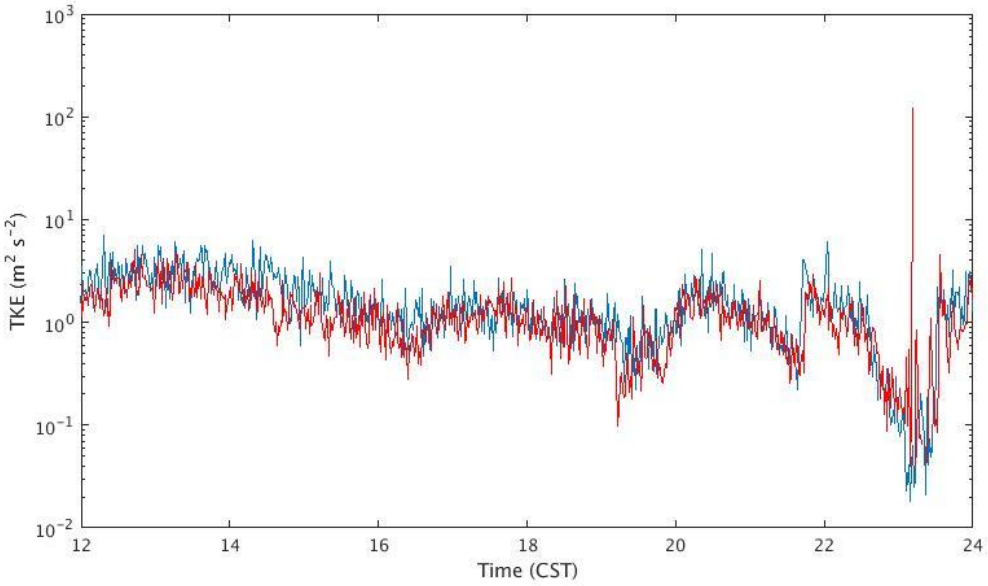

Figure 4.40: TKE plot for Centralia ASP (red) and BAU (blue) on 2017 03 01. As with Figure 4.39 the suspected gust front crossing occurred at around 0416 UTC (22:16 UTC 02/28). Another peak is seen around 30-minutes earlier at around 0350 UTC.

Table 4.9: Numerical $\overline{w}$ data for Centralia ASP and BAU on 2017 03 01 from 0412 to 0418 UTC.

	Time (UTC)	**0412**	**0413**	**0414**	**0415**	**0416**	**0417**	**0418**
Centralia ASP	$\overline{w}$ (m/s)	0.1720	0.1880	0.1720	0.1880	0.2413	0.1728	0.1766
Centralia BAU	$\overline{w}$ (m/s)	0.1253	-0.0013	0.1407	0.1363	-0.0237	-0.0056	-0.0038

4.1.7 07 March 2017

During early hours of March 7th, 2016 (March 6th in CST) another QLCS tracked through central Missouri and Columbia. The strong line brought heavy rain, severe winds, and some hail to the area. The storm moved rapidly through the Columbia area on an east-southeast track across the region. The rapid propagation and severe nature made this QLCS a prime candidate for an in-storm gust front, as the front would not easily be able to outrun the precipitation of the line. This idea was supported by the lack of an observed thin line on reflectivity during the event, so the MZZU in-storm settings were used for the analysis. The lowest level of radar data available was the 00.00 km level for both reflectivity and divergence.

The coverage of this event starts with the 0400 UTC scan. The target signature for this suspected gust front is the "central" section of the QLCS on the divergence field, represented by a large linear convergence line (CDA) (Fig 4.41). The leading edge of this feature lines up with the lower reflectivities that are just ahead of the heavier precipitation, which can also be seen in Figure 4.41.

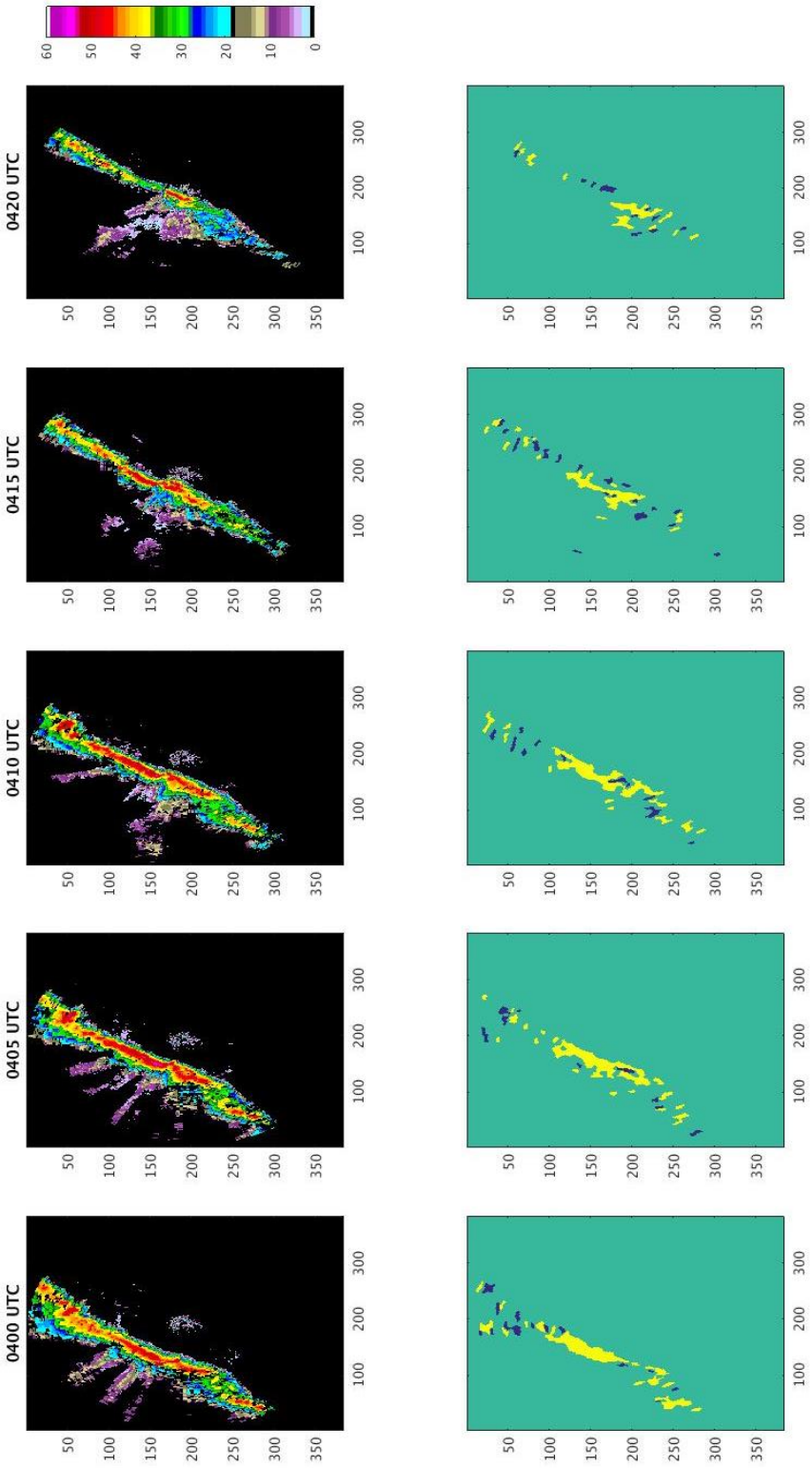

Figure 4.41: MZZU reflectivity and divergence on 2017 03 07 from 0400 to 0420 UTC.

Moving ahead to the 0415 UTC scan it can be seen that the line is fairly consistent over multiple scans, remaining spatially consistent with respect to the reflectivity field (Fig 4.41). Keeping its position just ahead of, and with, the heavy precipitation. Portions of the line that are moving parallel to the radials display the north-south oriented CDAs seen in some of the previous case days. As the QLCS begins to cross over MZZU at 0420 UTC more of the line is moving parallel to the radials and displays the N-S oriented div-conv patterns (Fig 4.41). In addition, the reflectivity field shows that as the QLCS gets closer to crossing over the radar the reflectivity signal begins to attenuate, this can also be seen in Figure 4.41. This attenuation increases as MZZU becomes subject to the heaviest precipitation from 0425-0435 UTC (Fig 4.42). The signal is obscured on both reflectivity and divergence fields as the radome wetness attenuation is in effect, meaning that the front cannot be clearly observed until the radar recovers. The recovery from wetness attenuation begins at around 0435 UTC, as reflectivity and divergence begin to resolve the leading edge of precipitation as it moves away from MZZU (Fig 4.42). There is still some obscurity caused by div-conv signal noise around the radar due to the increase in scatterers in motion with precipitation onset. Such as moving hydrometeors within the trailing stratiform section. The noisy signal persists through the remaining scans as the storm rapidly moves out of the area. Convergence signals, while not the most consistent in time following attenuation, can still be collocated with the leading edge during this period (0440-0456 UTC). Which can be seen in Figure 4.43.

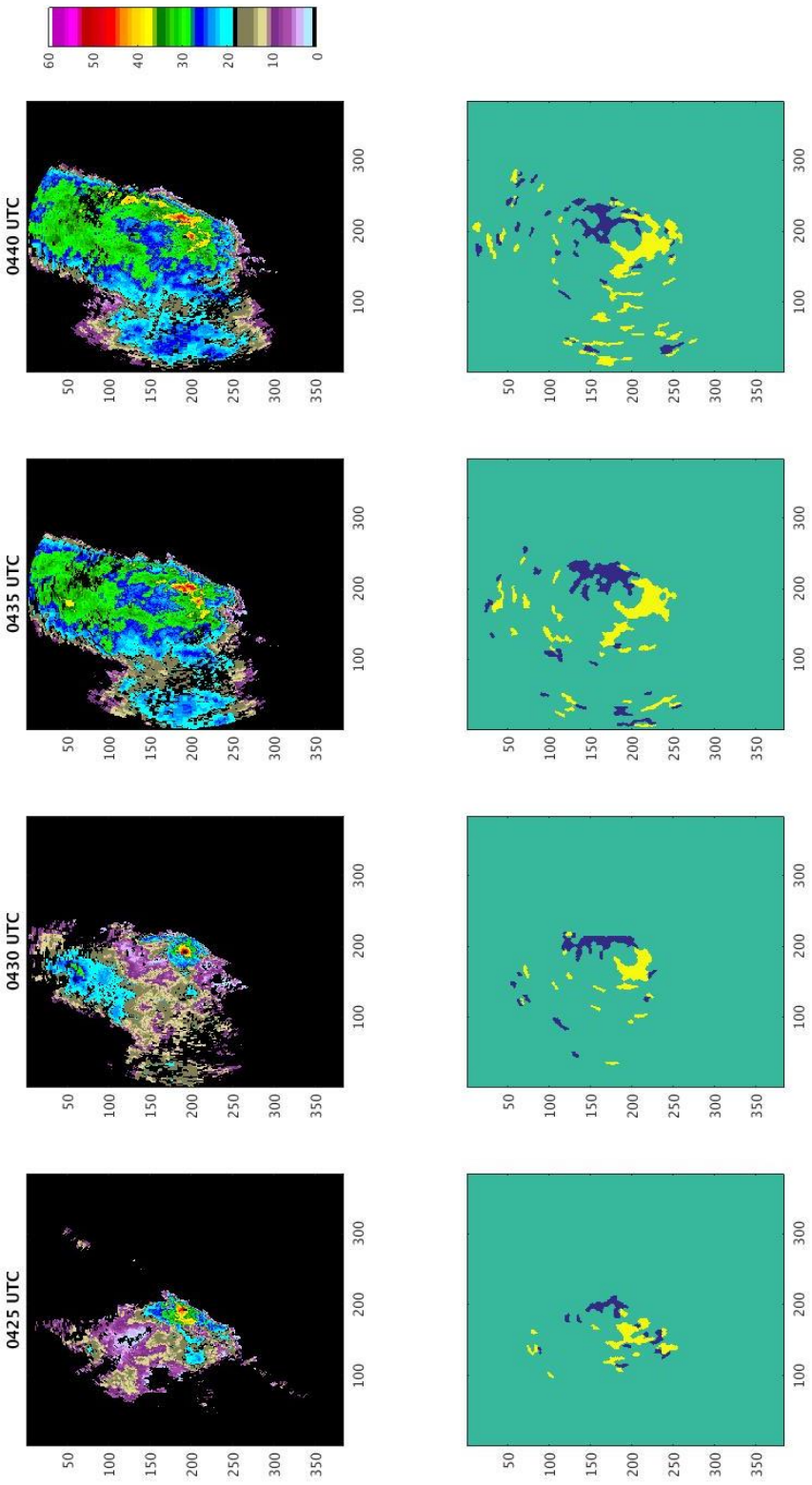

Figure 4.42: MZZU reflectivity and divergence on 2017 03 07 from 0425 to 0440 UTC.

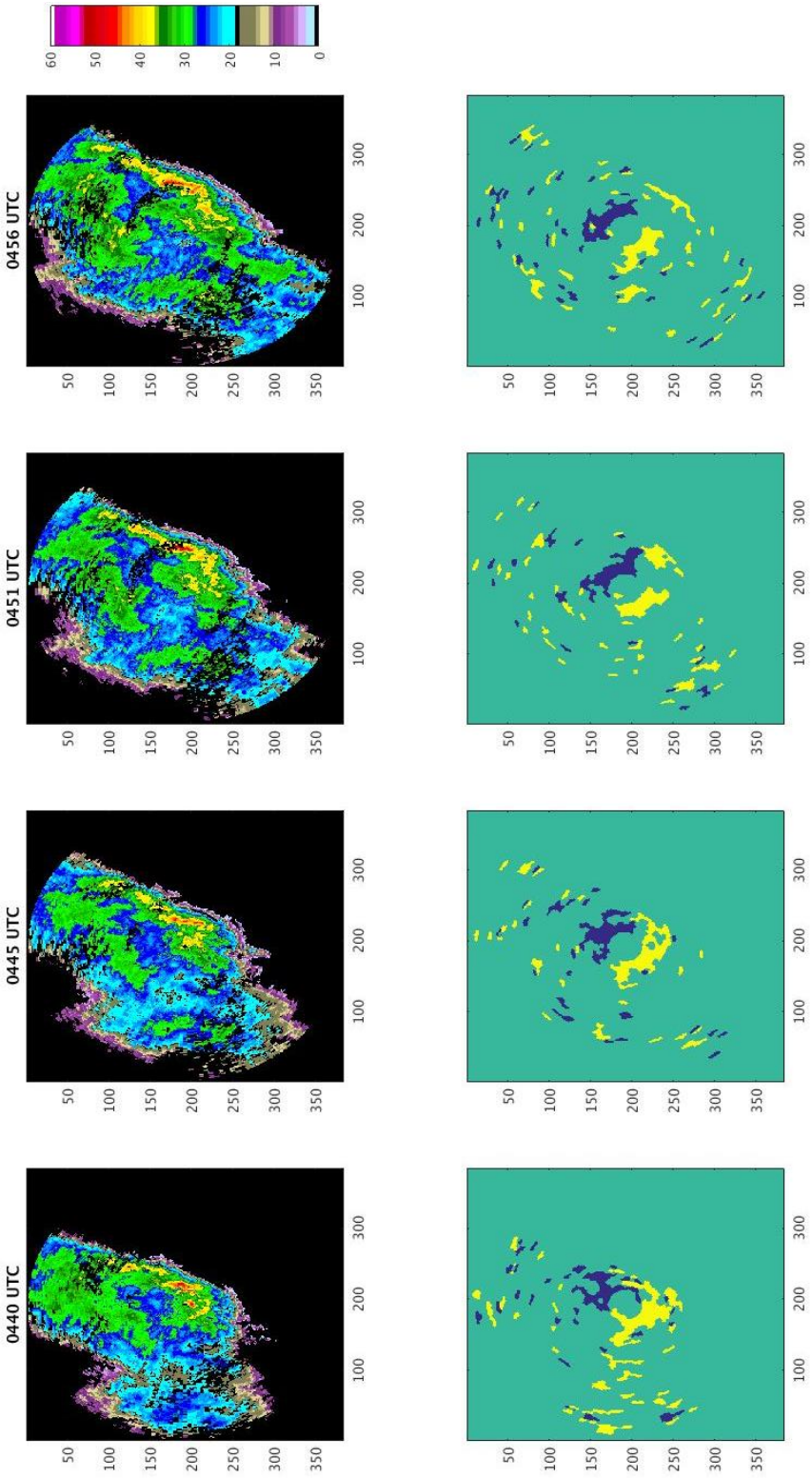

Figure 4.43: MZZU reflectivity and divergence on 2017 03 07 from 0440 to 0456 UTC.

The QLCS passed over both the Centralia sites and the MOFLUX site as it moved through the area. The QLCS passed over Centralia ASP and BAU by around 0420 UTC (Fig 4.41). $\overline{w}$ data from ASP and BAU can be seen in Figure 4.44 and table 4.10. Both sensors show the expected rise-fall trend in $\overline{w}$ for the frontal updraft passage. ASP has the local peak at 0416-0419 UTC, while BAU has the peak at 0415 UTC. The 0415 and 0420 UTC scans would put the Centralia sites at the northern side of the gust front signature (the convergence line). The 0420 UTC scan puts the sites under divergence as that section of the line moved parallel to the radar radial. Though the divergence would not be out of place at this time, since the updraft has passed both Centralia sites by this time. A well-defined peak in TKE for Centralia (Fig 4.45) correlates in time with the peak in $\overline{w}$ for ASP and BAU, supporting that the increase in turbulence was caused by the gust front reaching the sensors around 0415-020 UTC.

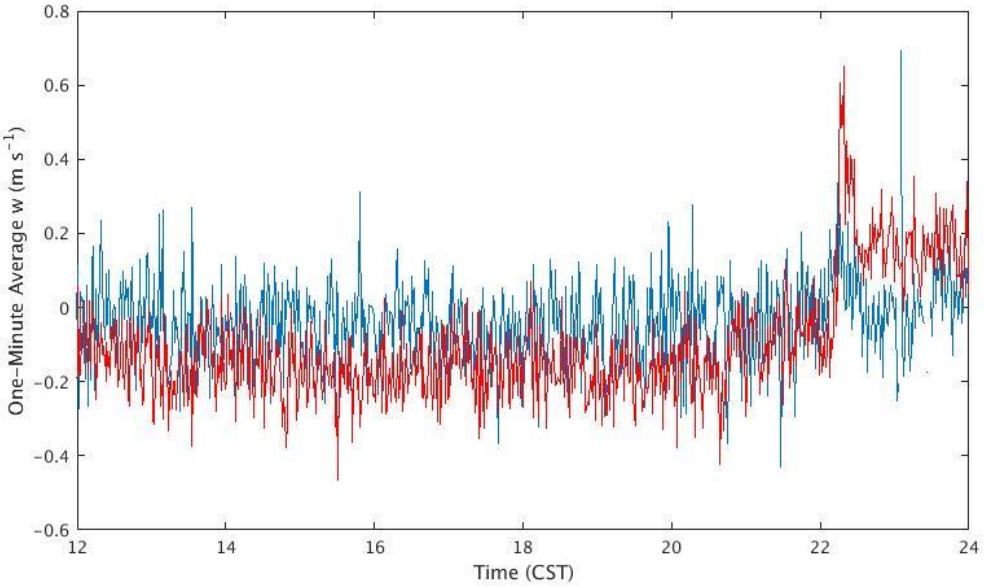

Figure 4.44: $\overline{w}$ plot for Centralia ASP (red) and BAU (blue) on 2017 03 07. Suspected gust front crossing occurred at 0419 UTC (22:19 CST 03/06).

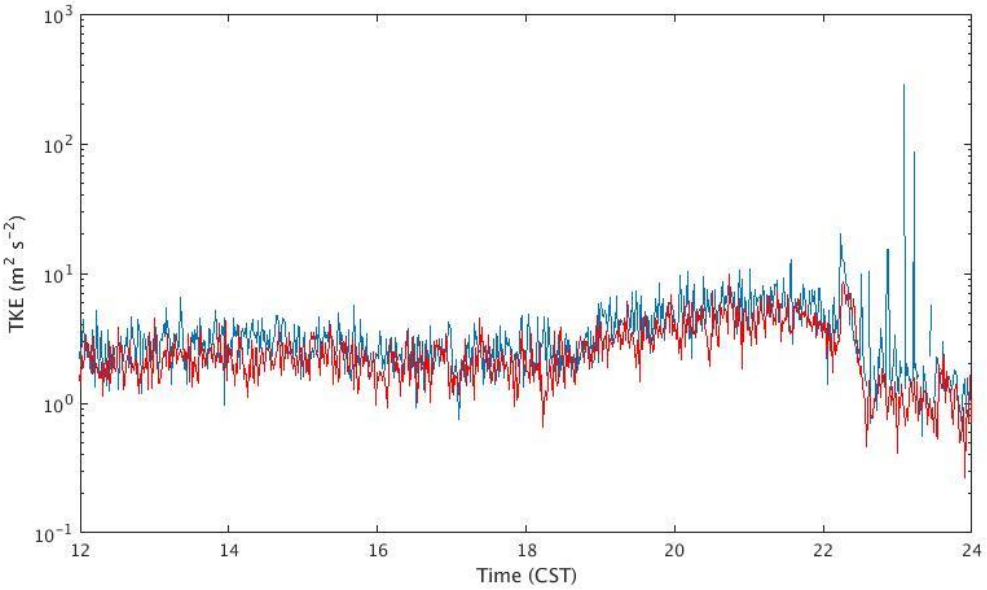

Figure 4.45: TKE plot for Centralia ASP (red) and BAU (blue) on 2017 03 07. As with Figure 4.44 the suspected gust front crossing occurred at around 0419 UTC (22:19 CST 03/06).

Table 4.10: Numerical $\overline{w}$ data for Centralia ASP and BAU on 2017 03 07 from 0416 to 0422 UTC.

	Time (UTC)	**0416**	**0417**	**0418**	**0419**	**0420**	**0421**	**0422**
Centralia ASP	$\overline{w}$ (m/s)	0.6075	0.4899	0.4910	0.6535	0.2280	0.4457	0.3541
Centralia BAU	$\overline{w}$ (m/s)	0.2511	0.0815	0.2041	0.0451	-0.0061	$1.38e^{-4}$	0.2301

MOFLUX was crossed over by the gust front during the attenuation recovery at 0435 UTC. MOFLUX $\overline{w}$ data shows the peak in the $\overline{w}$ trend at 0436 UTC on primary, and at 0434 UTC on secondary data. Figure 4.46 and Table 4.11. Both site groups showing the desired trend as the convergence crosses over MOFLUX suggests that the signature is an in-storm gust front. TKE for MOFLUX (Fig 4.47) supports the $\overline{w}$ data, showing a fairly well-defined peak around 0430 UTC, which is collocated in time with the $\overline{w}$ peak, also suggesting that the gust front is passing over at that time.

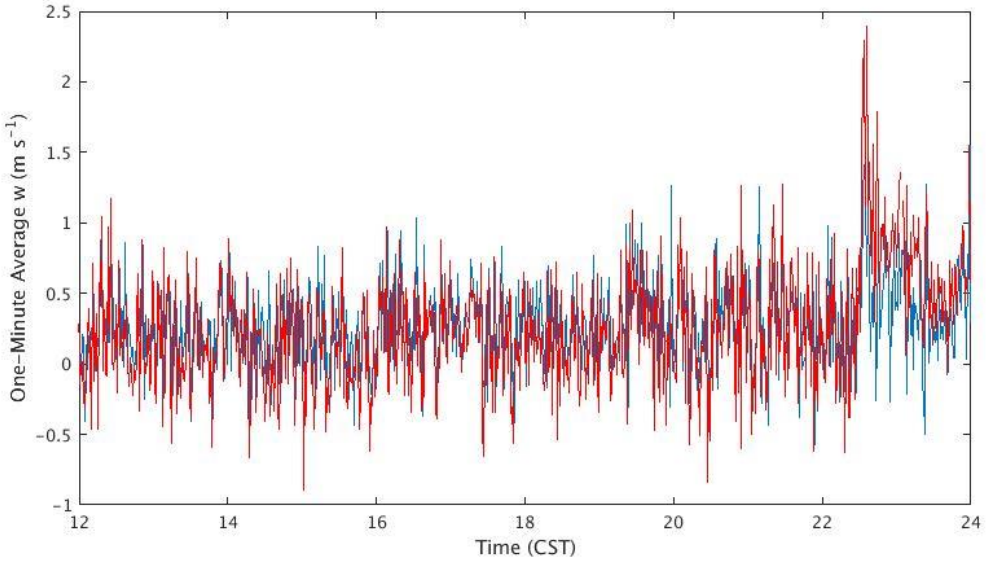

Figure 4.46: $\overline{w}$ plot for MOFLUX primary (red) and secondary (blue) on 2017 03 07. Suspected gust front crossing occurs at 0436 UTC (22:36 CST).

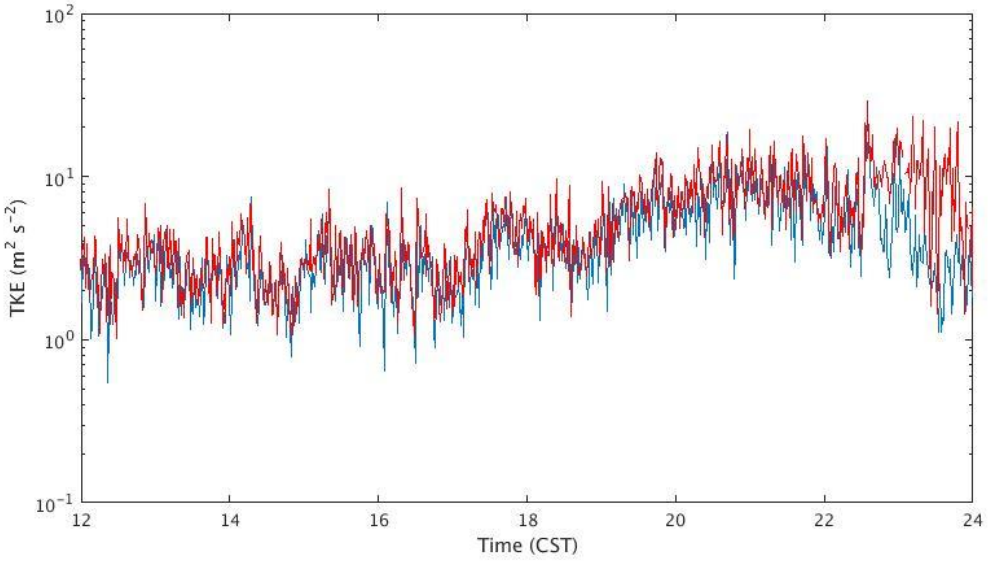

Figure 4.47: TKE plot for MOFLUX primary (red) and secondary (blue) on 2017 03 07. As with Figure 4.46 the suspected gust front crossing occurred at 0436 UTC (22:36 CST 03/06).

Table 4.11: Numerical $\overline{w}$ for MOFLUX on 2017 03 07 from 0432 to 0438 UTC.

	Time (UTC)	**0432**	**0433**	**0434**	**0435**	**0436**	**0437**	**0438**
MOFLUX Primary	$\overline{w}$ (m/s)	1.4406	2.0581	2.2906	1.1199	2.390	1.1294	1.4303
MOFLUX Secondary	$\overline{w}$ (m/s)	0.4334	1.2070	1.4688	1.2036	0.6245	1.2079	0.4864

4.1.8 19 May 2017

A QLCS moved through Columbia during the early hours of May 19th, 2017. This QLCS was a part of a larger system moving across the midwestern CONUS during the overnight hours. This storm was primarily a rain producer, with no reports of severe wind or hail during the time period. The lack of reports could have been due to the late-night hours that the storm moved through Columbia. As the storm approached Columbia and MZZU the fragments of a thin line could be seen on reflectivity, so the MZZU thin line settings were chosen for this case, with an area threshold of 2 pixels. The lowest level of radar data available during this case was the 00.00 km level for both reflectivity and divergence.

The thin line is first observed on the reflectivity product during the 0634 UTC scan, the fragment is seen ahead of the northern portion of the line. The echo is fairly weak as only pieces of the line resolve during this scan, likely due to the reflectivity display thresholds within WDSS processing that clean out data below 10 dBZ (Fig 4.48). Also, on Figure 4.48, the divergence product at this time show CDAs ahead of the QLCS, that can be attributed to this weak thin line. Lost signals due to the WDSS display thresholds also affect the divergence product.

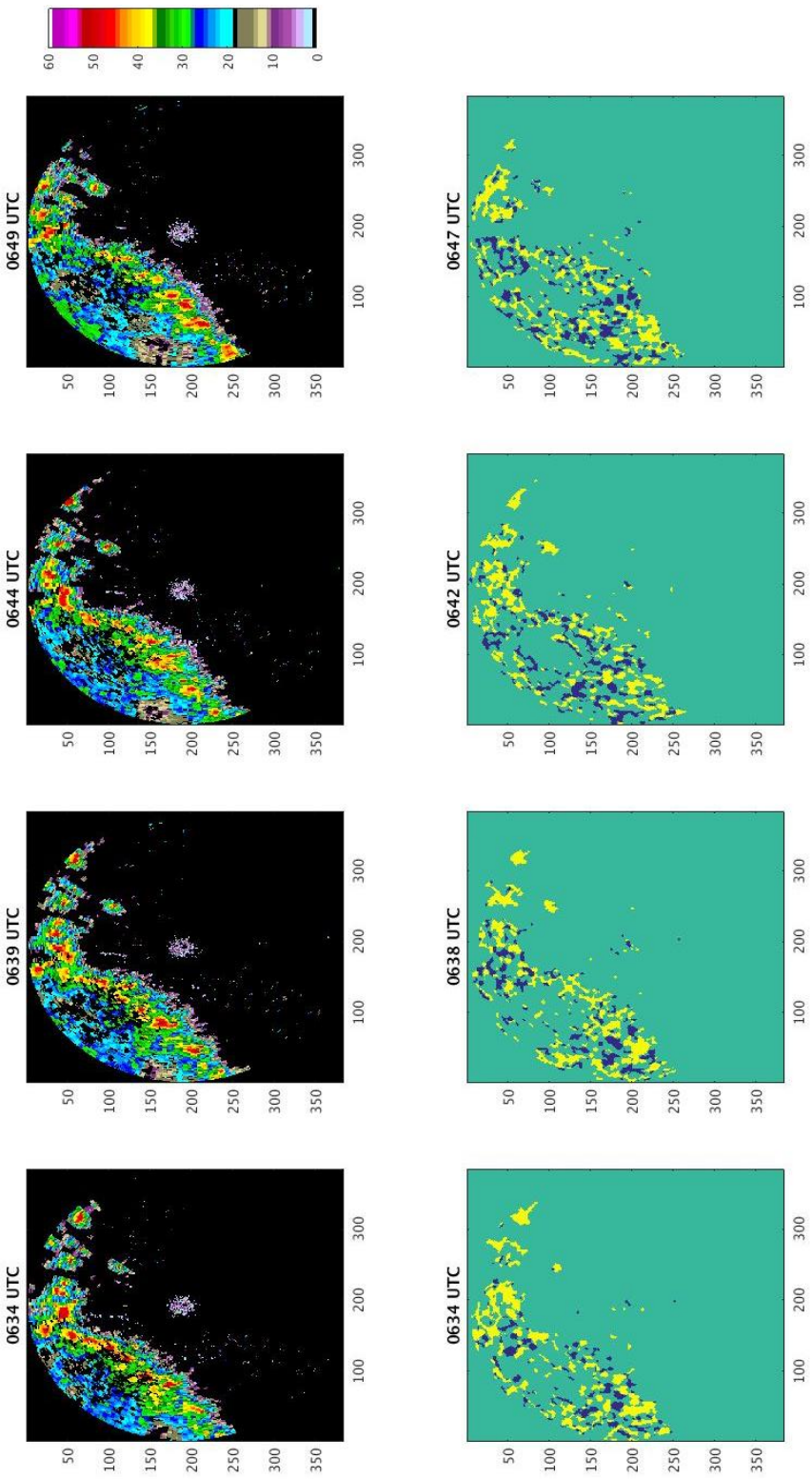

Figure 4.48: MZZU reflectivity and divergence on 2017 05 19 from 0634 to 0649 UTC.

Moving through the scans between 0630-0647 the thin line fragment remains consistent over time. Suggesting that the echo is not just noise on the initial observation on the 0630 UTC scan (Fig 4.48). Similarly, the divergence product during the same interval consistently shows a broken line of convergence blobs ahead of the precipitation across multiple scans (Fig 4.48). The number of CDAs in the line and the spacing between them, however, are not temporally consistent. The scans at 0644 UTC and 0647 UTC shows the convergence line with the highest clarity in the series of scans (Fig 4.48). The front then moves though the noisy signal in the immediate area surrounding MZZU, obscuring the signature on divergence, crossing over the radar by 0705 UTC. On reflectivity this can be seen as the line "pushing" through the noise (Fig 4.48 and 4.49). The gust front signature is more clearly defined as it crosses over MZZU (Fig 4.48). The consistency of the signature is still questionable during the period, as fewer CDAs resolve as the gust front crosses over MZZU, with the line practically disappearing on the 0705 UTC scan (Fig 4.49). The line is visible again on the 0715 UTC scan, seen as a linear formation of divergence blobs on the eastern side of the radar (Fig 4.49). The central portion of the gust front (thin line) is last seen on reflectivity at 0720 UTC, when the precipitation is about to cross over MZZU. On the divergence product the gust front is seen as a line of convergence blobs out ahead of the storm (Fig 4.49). The gust front ahead of the storm is no longer visible on reflectivity or divergence products following 0725 UTC scan as the precipitation overtakes MZZU (Fig 4.50).

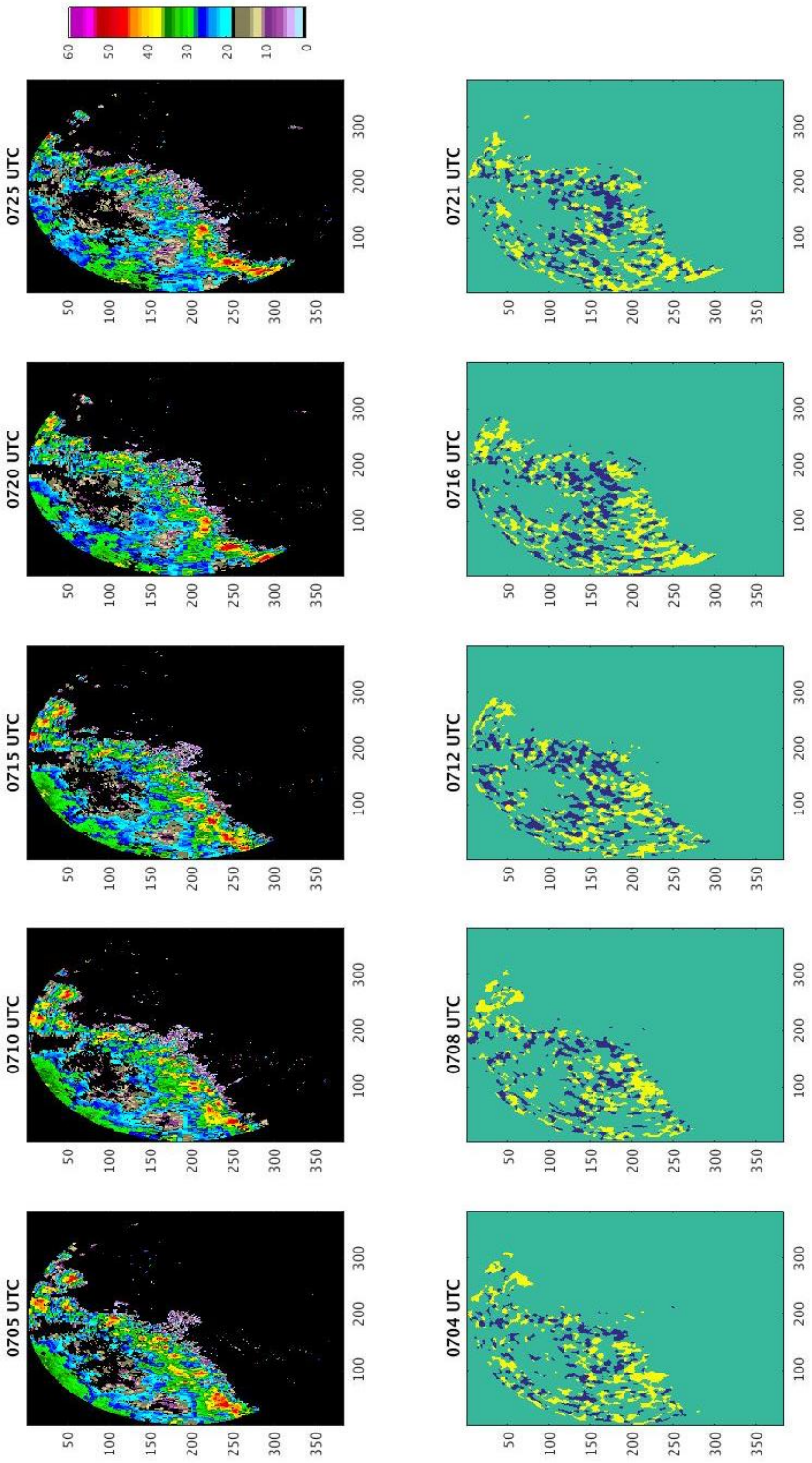

Figure 4.49: MZZU reflectivity and divergence on 2017 05 19 from 0705 to 0725 UTC.

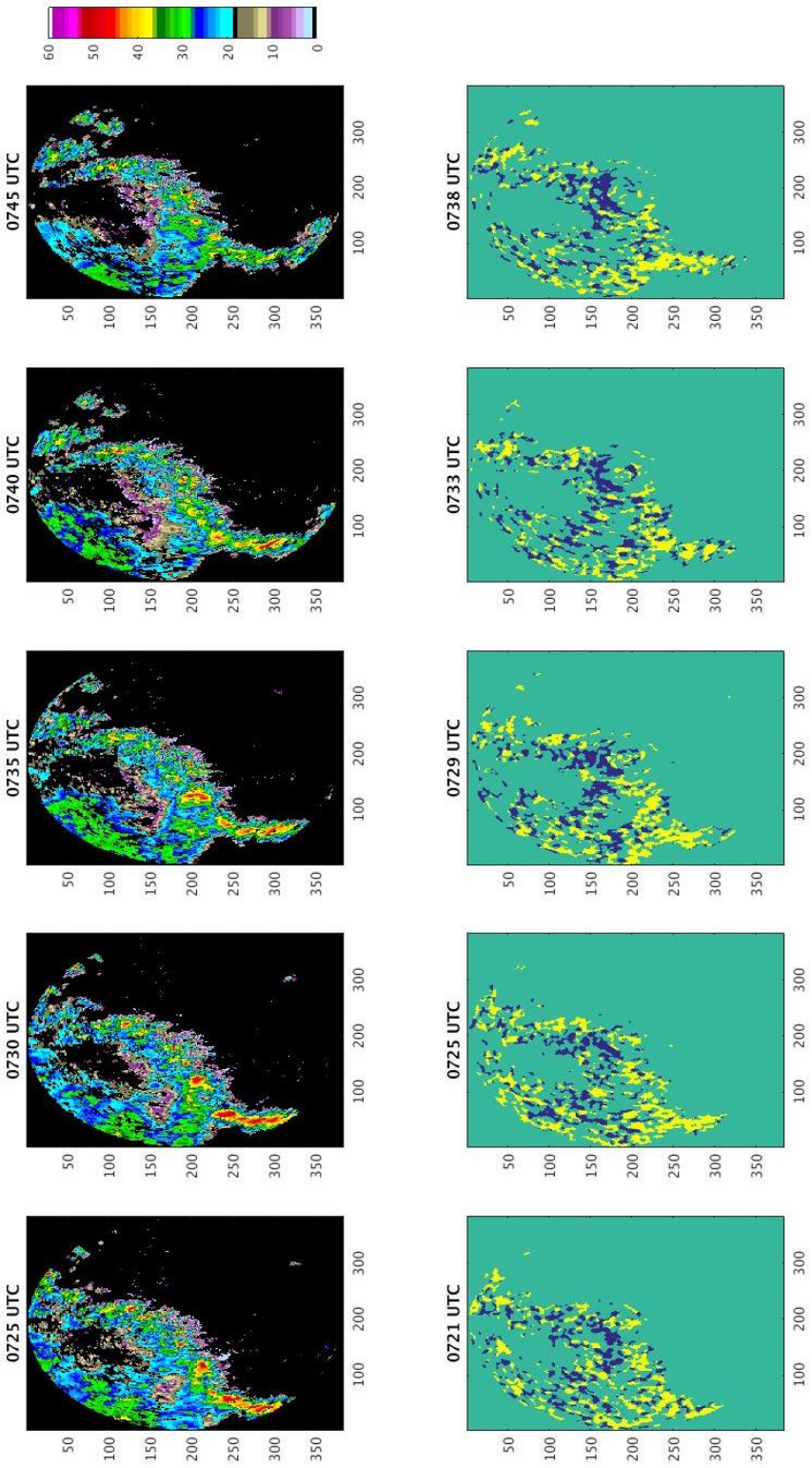

Figure 4.50: MZZU reflectivity and divergence on 2017 05 19 from 0720 to 0740 UTC.

As the thin line moved through the region it likely would have crossed over both the Centralia and MOFLUX sites. The time of the thin line crossing over Centralia ASP and BAU is around the time of the 0659 and 0705 UTC reflectivity scans. Centralia ASP shows the desired $\overline{w}$ trend at 0659 UTC (Fig 4.51, Table 4.12). BAU shows the trend occurring two minutes later, with the local peak at 0701 UTC. While the div scans were fairly inconsistent with CDAs, one can be seen in the northern portion on the 0704 UTC scan on Figure 4.49, just following the peak in $\overline{w}$ at ASP and one minute before the peak at BAU. However, the TKE for Centralia (Fig 4.52) is not supportive for the claim by the $\overline{w}$, as the TKE data at 0659 UTC shows that the turbulence is decreasing overall, with no local rises that suggest a gust front is causing increased turbulence. The line passage over MOFLUX occurred later at approximately 0720 UTC. Both primary and secondary data both show the peak of the $\overline{w}$ trend at 0718-0720 UTC (Fig 4.49 and 4.50, Table 4.13). The TKE data for MOFLUX shows a small peak following 0700 UTC (02:00 CDT), which 0720 UTC is within, supporting the $\overline{w}$ data with an increase in turbulence coinciding with the increase in vertical velocity.

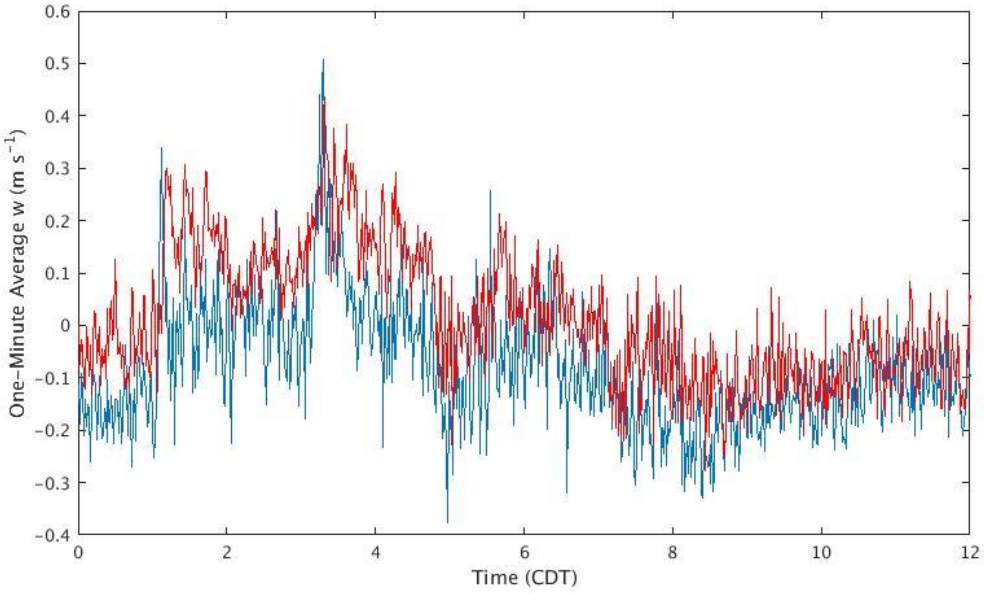

Figure 4.51: $\overline{w}$ plot for Centralia ASP (red) and BAU (blue) on 2017 05 19. Suspected gust front crossing occurred at around 0659 UTC (01:59 CDT).

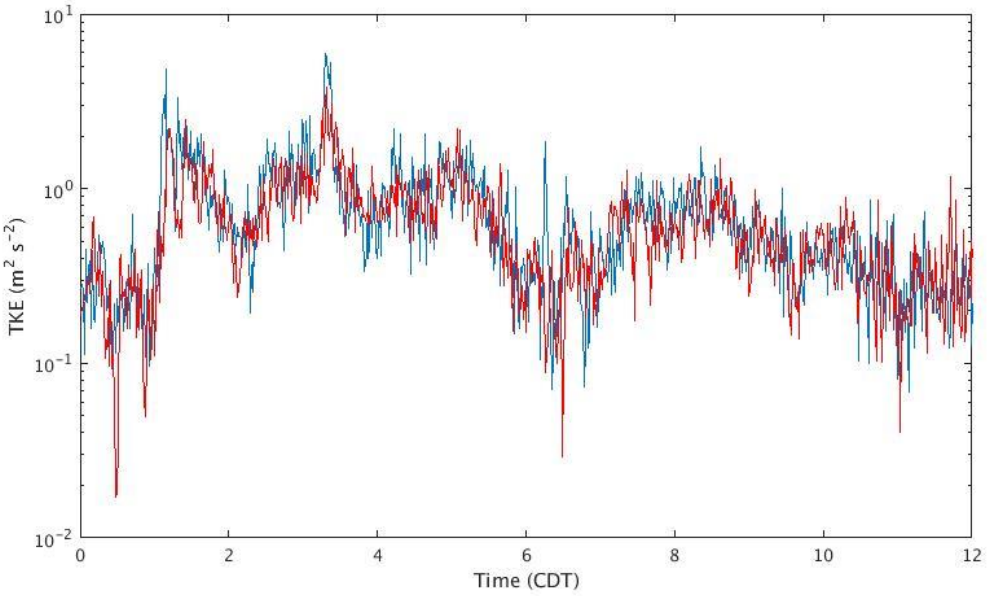

Figure 4.52: TKE plot for Centralia ASP (red) and BAU (blue) on 2017 05 19. As with Figure 4.51 the suspected gust front crossing occurred at around 0659 UTC (01:59 CDT).

Table 4.12: Numerical $\overline{w}$ data for Centralia ASP and BAU on 2017 05 19 from 0658 to 0703 UTC.

	Time (UTC)	**0658**	**0659**	**0700**	**0701**	**0702**	**0703**
Centralia ASP	$\overline{w}$ (m/s)	0.0805	0.2076	0.2002	0.1314	0.0821	0.1161
Centralia BAU	$\overline{w}$ (m/s)	-0.1475	-0.1530	0.0062	0.0953	0.0285	-0.1307

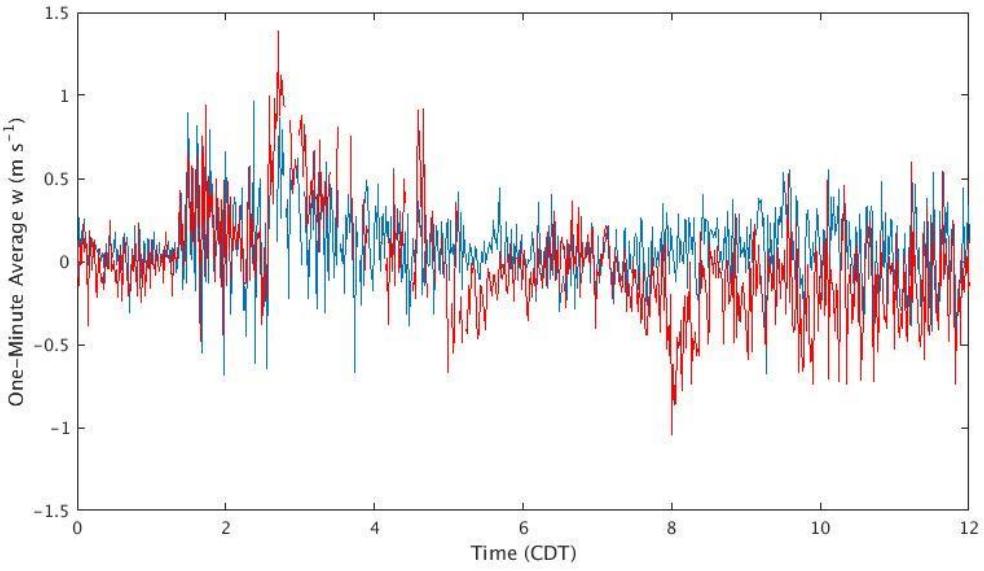

Figure 4.53: $\overline{w}$ plot for MOFLUX primary (red) and secondary (blue) on 2017 05 19. Suspected gust front crossing occurred at around 0718 UTC (02:18 CDT).

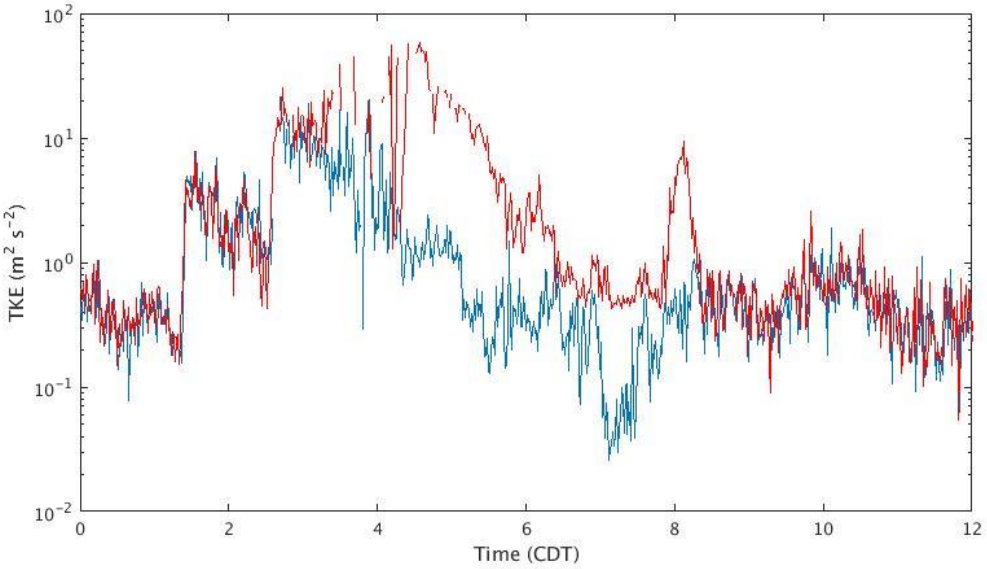

Figure 4.54: TKE plot for MOFLUX primary (red) and secondary (blue) on 2017 05 19. As with Figure 4.53 the suspected gust front crossing occurred at around 0718 UTC (02:18 CDT).

Table 4.13: Numerical $\overline{w}$ data for MOFLUX on 2017 05 19 from 0717 to 0723 UTC.

	Time (UTC)	**0717**	**0718**	**0719**	**0720**	**0721**	**0722**	**0723**
MOFLUX Primary	$\overline{w}$ (m/s)	0.1562	0.5652	0.0932	-0.113	0.2860	0.2140	-0.0132
MOFLUX Secondary	$\overline{w}$ (m/s)	0.1204	0.5069	0.5753	0.2048	0.1882	-0.0178	0.9669

4.1.9 15 October 2017

During the evening of October 15th, 2017 (October 14th in CST), a QLCS moved through Central Missouri, impacting the city of Columbia. While the section of the storm that impacted Columbia did not receive any storm reports during the early evening, the system received several severe wind reports during the course of the event. A thin line on reflectivity was observed by MZZU ahead of the main precipitation, so the thin line settings were used with an area threshold of 3 pixels. The lowest available radar data for this case was the 00.00 km level for both reflectivity and divergence.

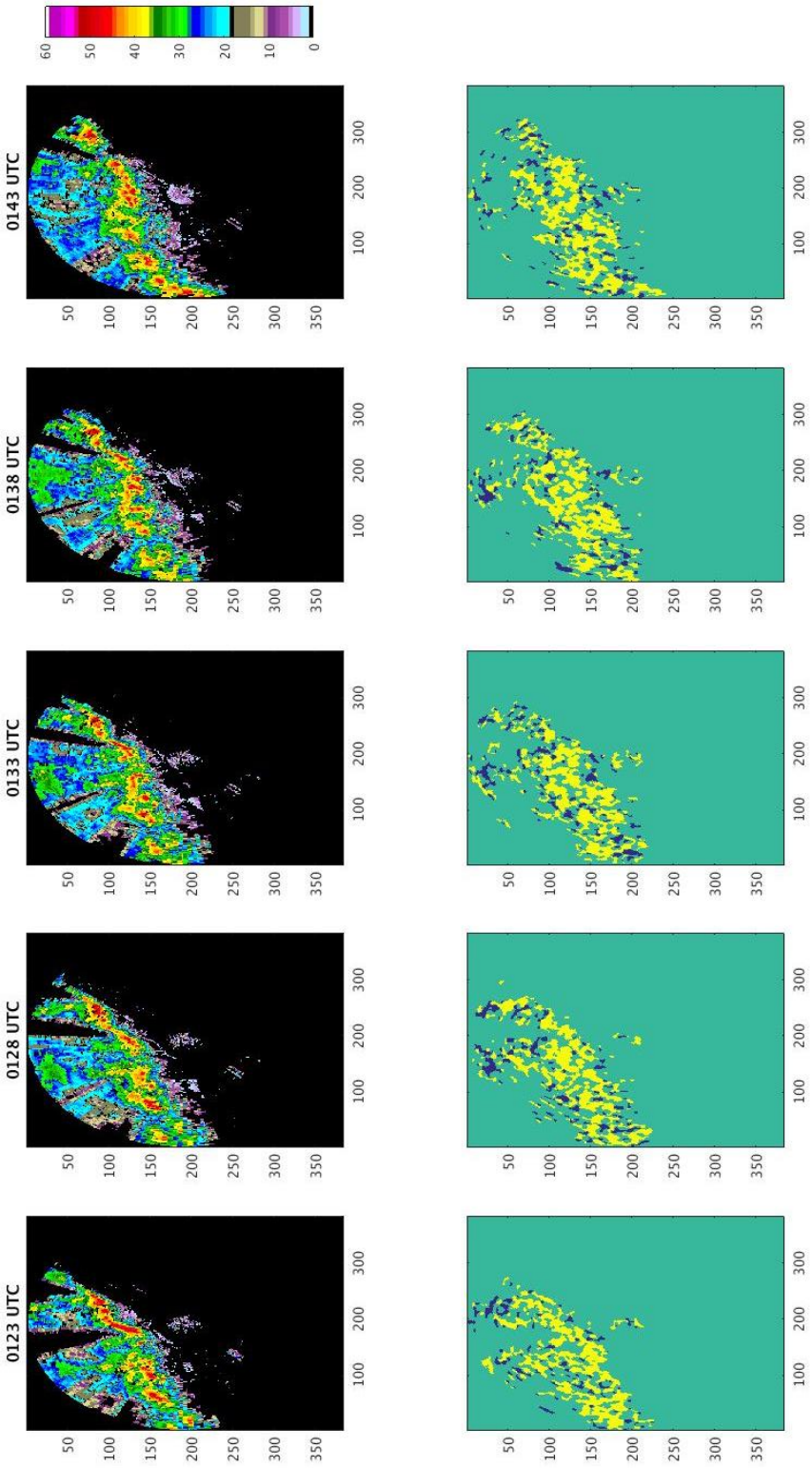

Figure 4.55: MZZU reflectivity and divergence on 2017 10 15 from 0123 to 0143 UTC.

The thin line is first visible on reflectivity during the 0123 UTC scan (Fig 4.55) as the gust front begins to outrun the precipitation echoes. This line is initially very short, but the signal grows in length over time as more scatterers are picked up by the frontal updraft. Due to the close proximity to the leading precipitation of the parent storm the convergence line that should be correlated with the line on reflectivity is not yet visible on the divergence scan (Fig 4.55). Moving through the next several timesteps (0123 UTC – 0148 UTC), as the QLCS moves to the east-northeast, the front moves southeast out from the QLCS and into the immediate area surrounding MZZU. The thin line has grown in length since the 0123 UTC scan, but it is not a continuous feature with breaks along its length where the reflectivity falls below he WDSS display threshold. Similarly, on the divergence product the thin line is not well resolved, reflectivity and divergence can be seen in Figure 4.55. The gust front can be inferred on the divergence product as it begins to pass through the noisy signal surrounding MZZU.

In the 0133 UTC scan the gust front is marked by a divergence-convergence pair on the northwest side of the noise surrounding MZZU (Fig 4.55). The div-con signal is by the noise as the front crosses MZZU during the 0143 UTC and 0148 UTC scans but is visible on reflectivity (Fig 4.55). The signature on divergence is visible again following the 0153 UTC scan. As the gust front continues to advance past MZZU to the southeast, the front maintains a convergence line, but the size and shape of the line are not very consistent over multiple scans (Fig 4.56). During the 0204 UTC and 0209 UTC scans, however, the convergence line is paired with divergence, forming the “optimal” div-conv pair signature (Fig 4.57). Following the 0209 UTC scan the gust front is moving out

of the area near MZZU. The last divergence scan that can be associated with certainty to the gust front is 0214 UTC (Fig 4.57), where the signature is on the southeast side of MZZU radar noise. A small line of convergence followed by a divergence line and another convergence line in a conv-div-conv arrangement.

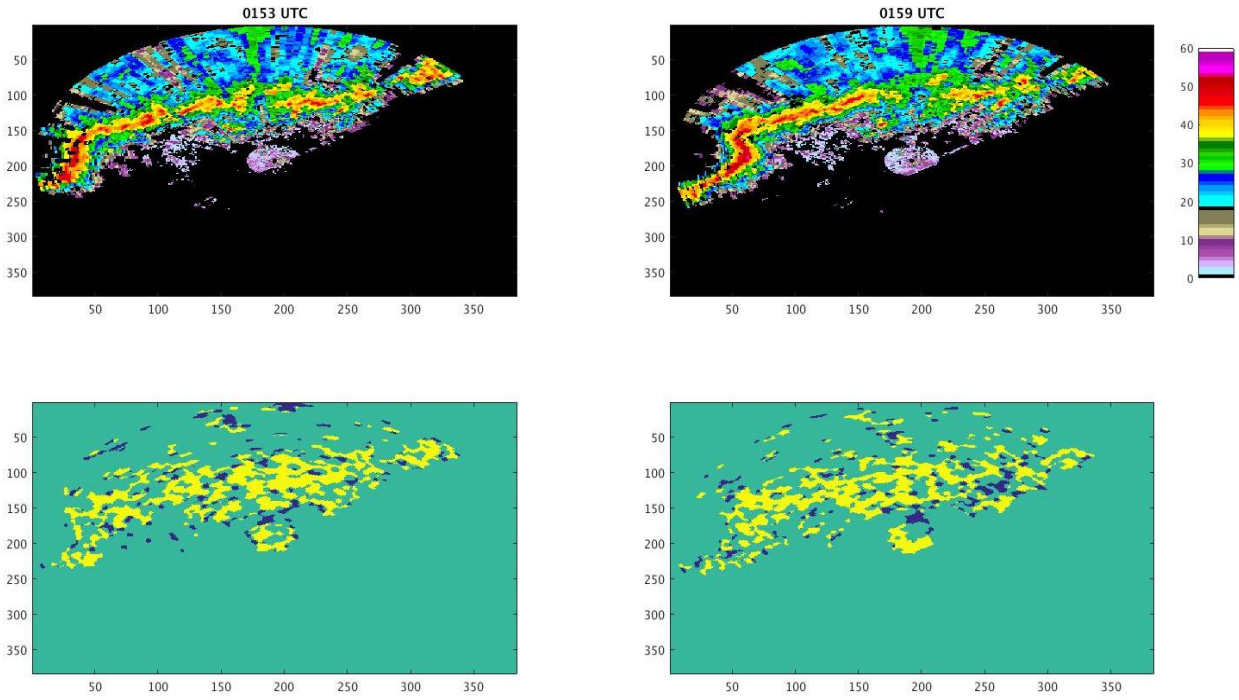

Figure 4.56: MZZU reflectivity and divergence on 2017 10 15 from 0153 to 159 UTC.

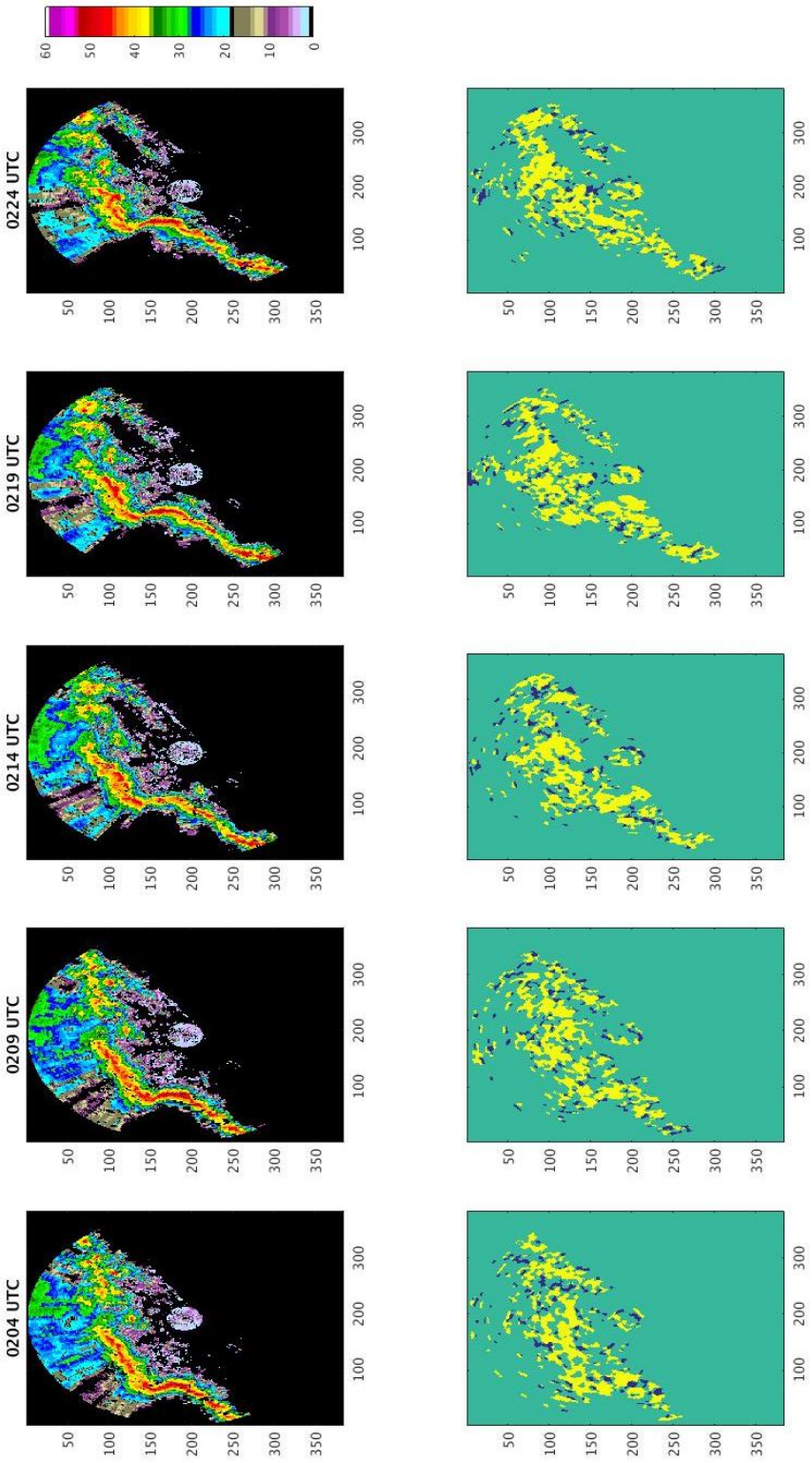

Figure 4.57: MZZU reflectivity and divergence on 2017 10 15 from 0204 to 0224 UTC.

The gust front would have crossed both the Centralia and MOFLUX sites as it moved through Columbia. Since the front moved from northeast to southeast, Centralia ASP and BAU would have detected the frontal updraft first. By the first appearance of the thin line on reflectivity at 0123 UTC, the front had already crossed over the two sensors. $\overline{w}$ for both ASP and BAU show that the gust front passage occurred at around 0117-0118 UTC, with the detection of the local peak in $\overline{w}$ (Fig 4.58, Table 4.14). TKE for Centralia (Fig 4.59) also shows an increase around the same time. But, given that the conv signature that was associated with the thin line was not visible until later, its likely that the sensors detected the front as it was still in-storm. Both w and TKE also show a larger peak prior to the suspected time of gust front crossing. Implying that the sensors detected an earlier outflow from the thunderstorm.

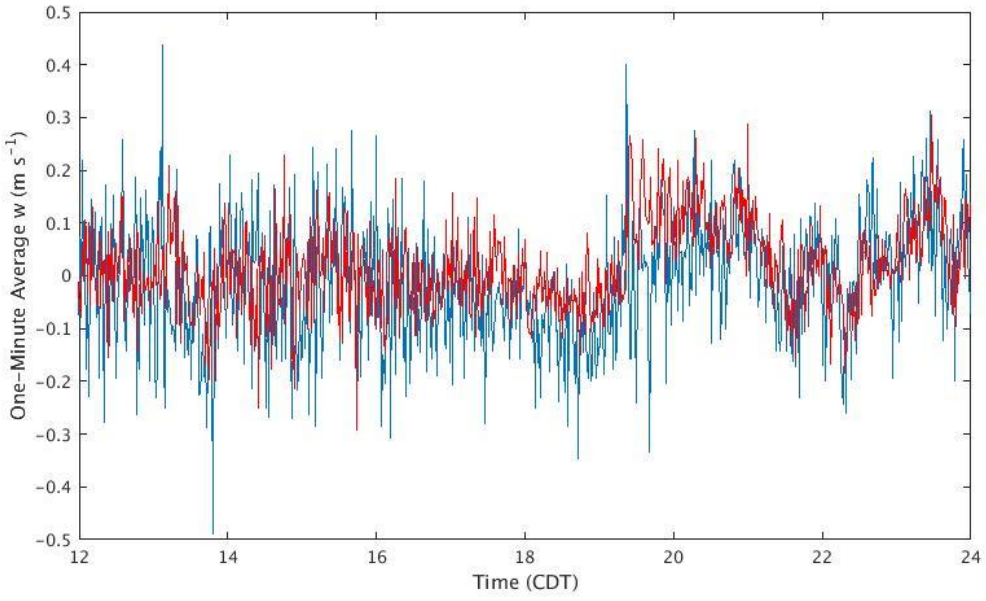

Figure 4.58: $\overline{w}$ plot for Centralia ASP (red) and BAU (blue) on 2017 10 15. Suspected gust front crossing occurred at around 0118 UTC (20:18 UTC 10/14).

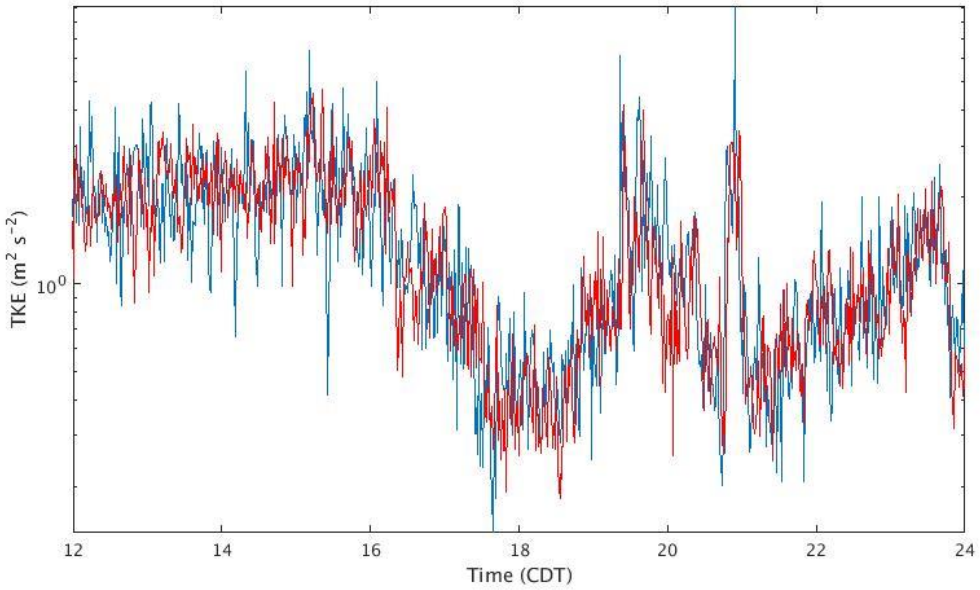

Figure 4.59: TKE plot for Centralia ASP (red) and BAU (blue) on 2017 10 15. As with Figure 4.58 the suspected gust front crossing occurred at around 0118 UTC (20:18 CDT 10/14).

Table 4.14: Numerical $\overline{w}$ data for Centralia ASP and BAU on 2017 10 15 from 0117 to 0123 UTC.

	Time (UTC)	**0117**	**0118**	**0119**	**0120**	**0121**	**0122**	**0123**
Centralia ASP	$\overline{w}$ (m/s)	0.0893	0.2597	0.1137	0.1451	0.0930	0.1791	0.1467
Centralia BAU	$\overline{w}$ (m/s)	0.2751	-0.0353	0.1929	0.1114	0.0016	0.0862	0.0755

MOFLUX was crossed over as the gust front begins to move away from MZZU by 0204 UTC. $\overline{w}$ data for MOFLUX was only available with the primary dataset during this case. The data can be seen in Figure 4.60 and Table 4.15. The updraft passes through at around 0157 UTC, with the peak in $\overline{w}$ at that time. TKE (Fig 4.61) also shows an increasing trend at the same time, suggesting that there is increasing turbulence that as the gust front is crossing over MOFLUX, which is expected. This would correlate best with the scans at 0159 UTC (Fig 4.56), with the CDAs on the southeast of the radar, as the convergence line on that scan would have likely just crossed over MOFLUX.

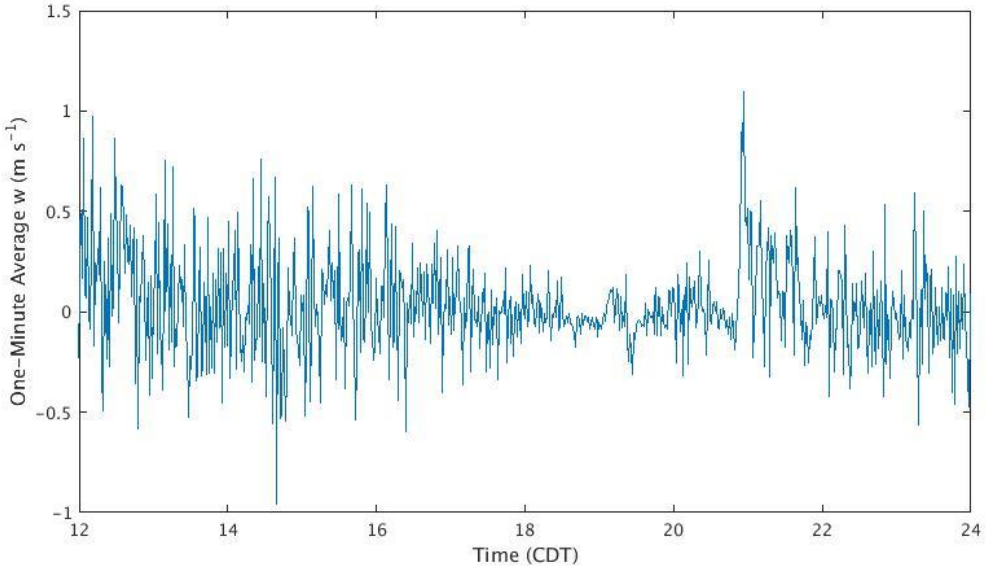

Figure 4.60: $\overline{w}$ plot for MOFLUX primary (blue) on 2017 10 15. Suspected gust front crossing occurred at around 0157 UTC (20:57 CDT 10/14).

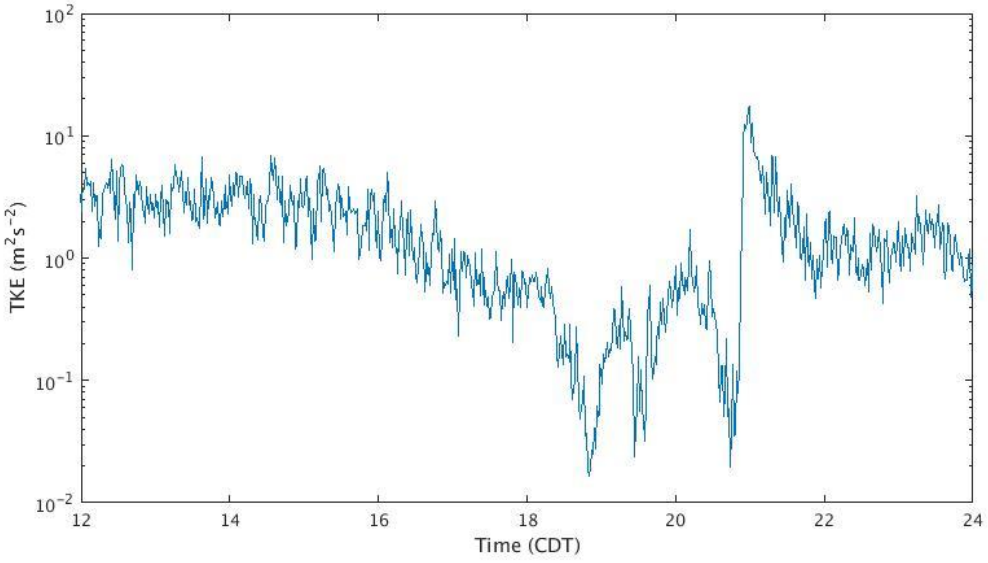

Figure 4.61: TKE plot for MOFLUX primary (blue) on 2017 10 15. As with Figure 4.60 the suspected gust front crossing occurred at around 0157 UTC (20:57 CDT 10/14).

Table 4.15: Minute average w for MOFLUX on 2017 10 15 from 0156 to 0202 UTC. As mentioned earlier, secondary data was unavailable during this case.

	Time (UTC)	**0156**	**0157**	**0158**	**0159**	**0200**	**0201**	**0202**
MOFLUX Primary	$\overline{w}$ (m/s)	0.8002	1.0945	0.4550	0.5144	0.1625	0.5007	0.4878
MOFLUX Secondary	$\overline{w}$ (m/s)			N/A				

4.2 KLSX Gust Front Cases

4.2.1 19 July 2006

The evening of July 19th, 2006 hosted a powerful Mesoscale Convective System (MCS), classified as a derecho, that tore across the Saint Louis area. This storm brought severe straight-line winds, hail, as well as some spin up tornadoes. As the storm moved through the KLSX operating area from the northeast in Illinois to the southwest, a distinct thin line echo was seen on reflectivity ahead of the MCS. This case and the other two KLSX cases analyzed in this study used the KLSX settings to analyze gust fronts. The lowest level of radar data available was the 01.00 km level for both reflectivity and divergence. In addition, the radar data for this case had scans available every ten minutes instead of the standard five-minute interval between scans.

Starting with the 2316 UTC reflectivity scan, the thin line and MCS are clearly seen in the northeast quadrant of KLSX's visible range. At this time the gust front is not well defined on the divergence field (Fig 4.62), as only a couple of blobs reside ahead of the MCS where the thin line is located on reflectivity. Moving to the 2327 UTC scan, the gust front is now more defined on the divergence field, the "central" section of the boundary showing the optimal div-conv pair (Fig 4.62). Moving through the next few time steps from 2337 UTC to 2357 UTC, the MCS continues to track southeastward. The gust front signature on divergence maintains its position ahead of the precipitation, correlated with the thin line on reflectivity (Fig 4.62). The explicit shape of the gust

front is not very consistent across multiple divergence scans, with variations in the blobs that make up the line. While this is not a problem for user observation, it could be difficult for automated detection.

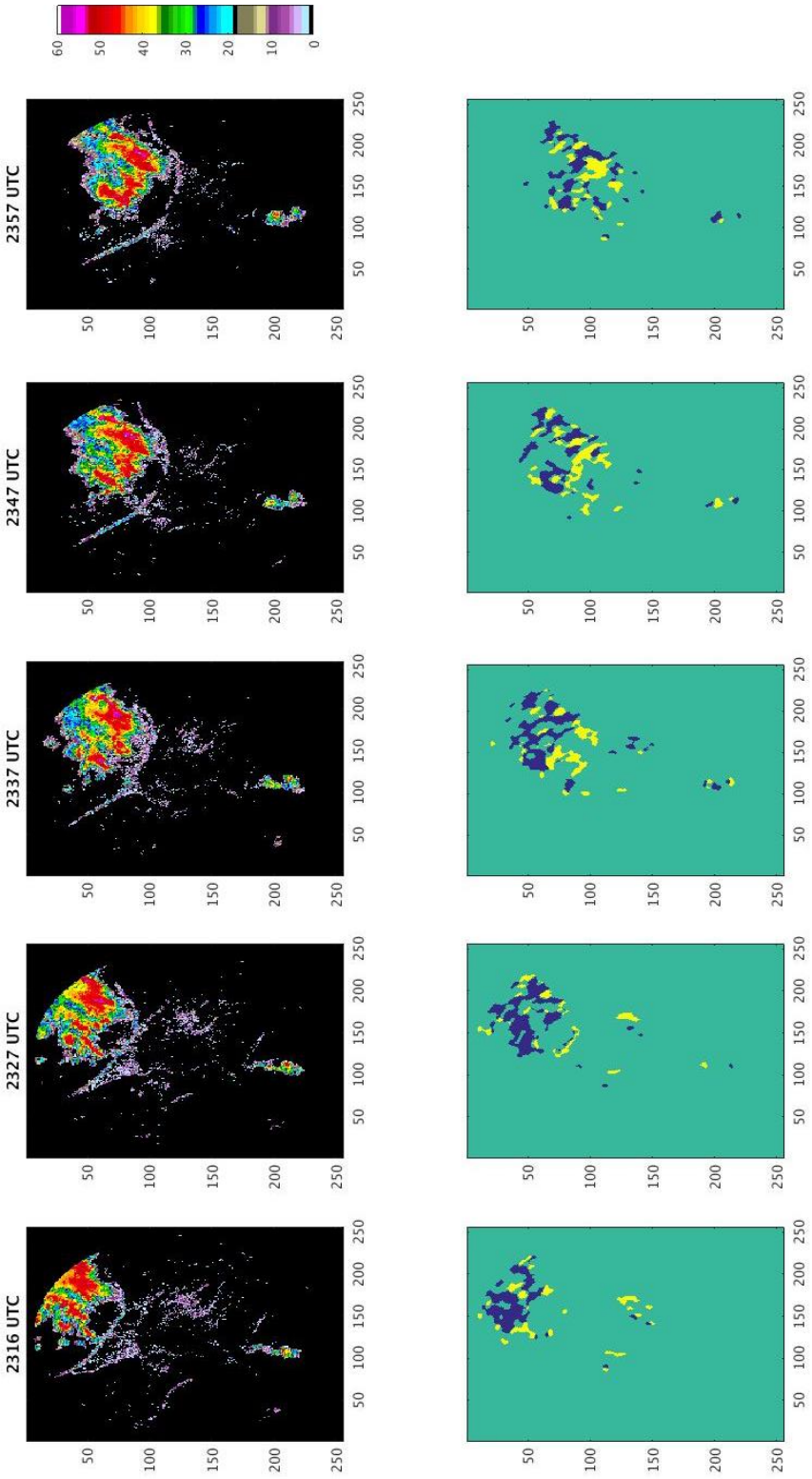

Figure 4.62: KLSX reflectivity and divergence on 2006 07 19 from 2316 to 2357 UUTC.

As the front crosses over KLSX between approximately 0007 UTC to 0018 UTC (07/20), the clear air section between the gust front thin line and the MCS begins to "fill in" on the divergence product (Fig 4.63). This is likely due to the KLSX radar beginning to sample the turbulent region behind the frontal boundary. As precipitation begins to move over KLSX on the 0028 UTC scan the gust front can still be correlated to the lead of the divergence signals, when referenced with the reflectivity scans, which still show the clear air between the thin line and the storm (Fig 4.64). However, as the heavier precipitation moves over KLSX the signal on both reflectivity and divergence becomes increasingly obscured by the attenuation (Fig 4.64). Though, the div-conv signals related to the updrafts and downdrafts in the storm are still clearly visible. As KLSX exits from the backside of the thunderstorm on the 0118 UTC and 0129 UTC scans, portions of the thin line ahead of the storm become visible again on divergence (Fig 4.65). As the MCS continues to the southwest during the 0139 UTC and 0149 UTC scans the signals around KLSX become increasingly noisy over time due to the particle scattering (Fig 4.66). The storm proceeds to move out of the KLSX operating range on 01.00 km.

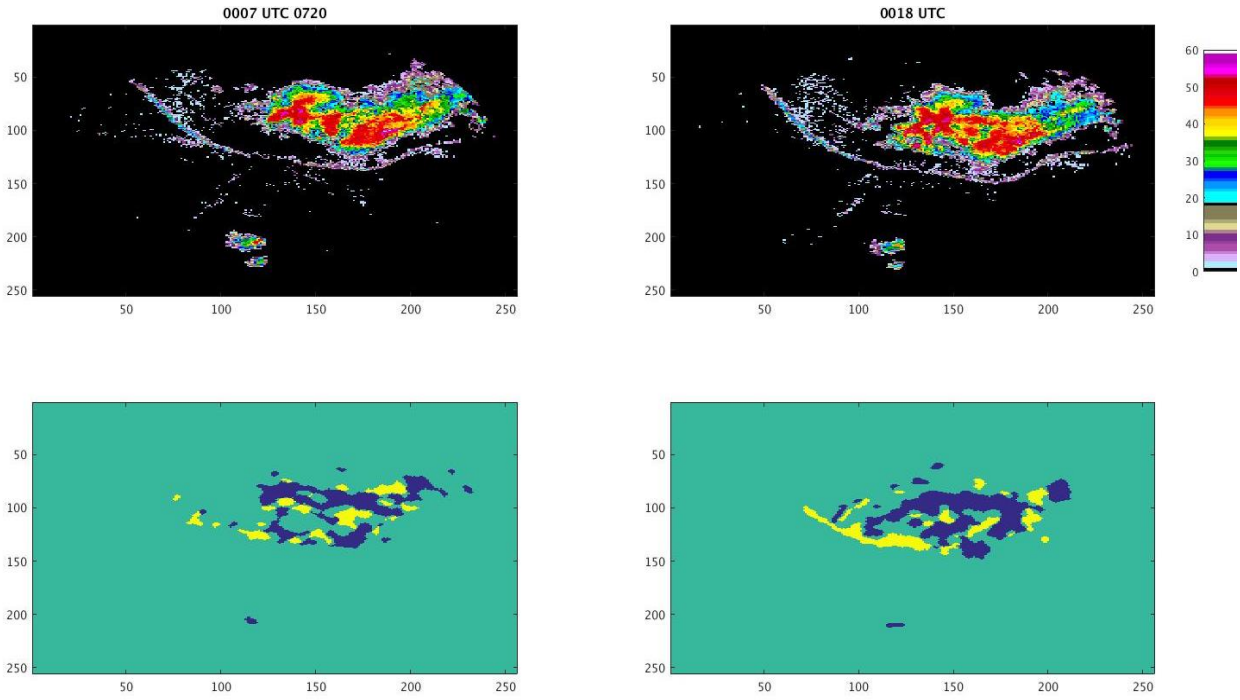

Figure 4.63: KLSX reflectivity and divergence on 2006 07 19 from 0007 to 0018 UTC.

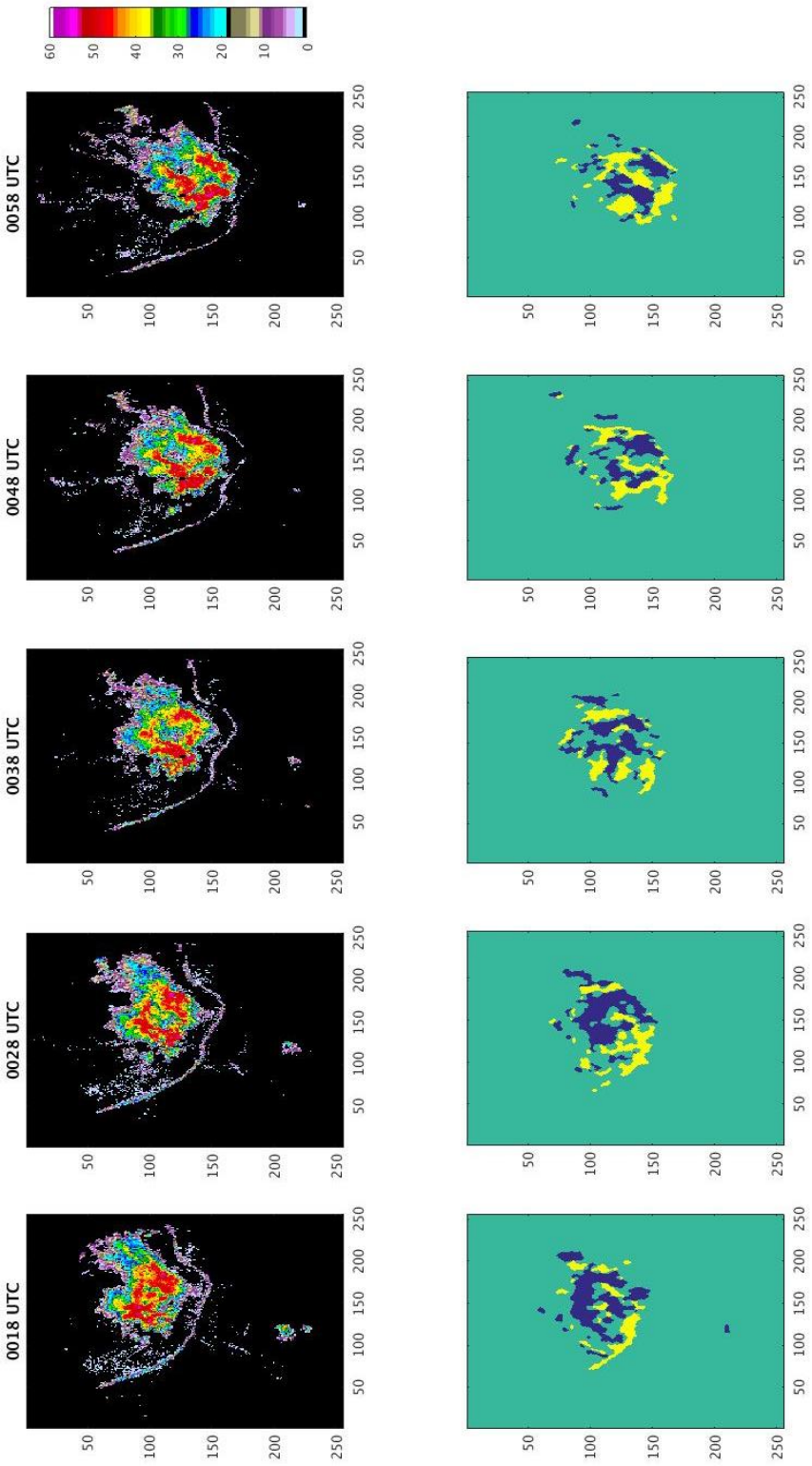

Figure 4.64: KLSX reflectivity and divergence on 2006 07 20 from 0018 to 0058 UTC.

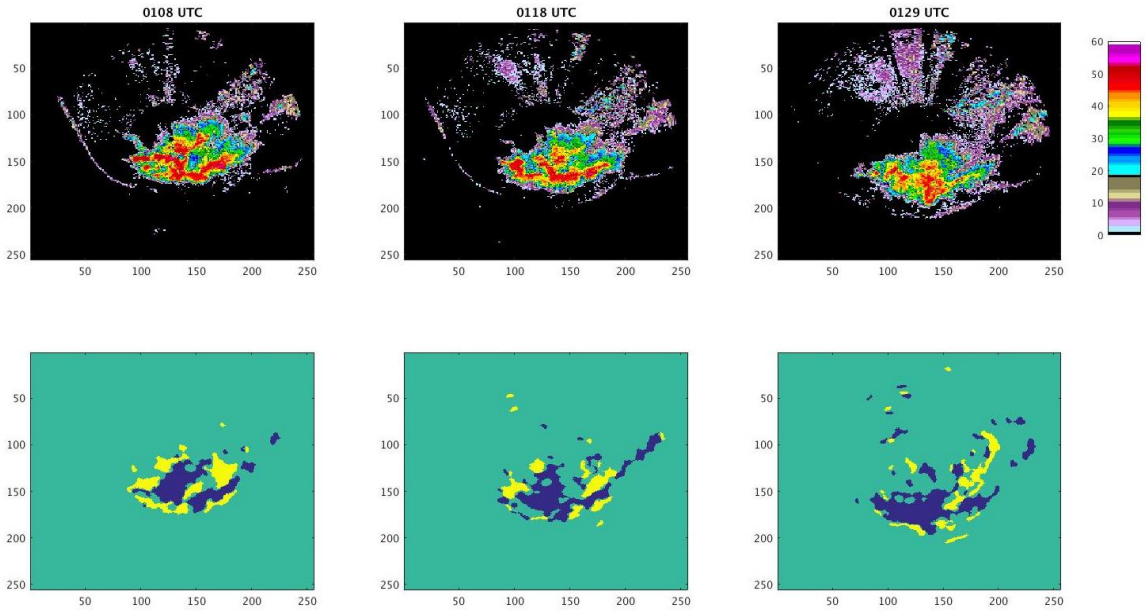

Figure 4.65: KLSX reflectivity and divergence on 2006 07 20 from 0108 to 0129 UTC.

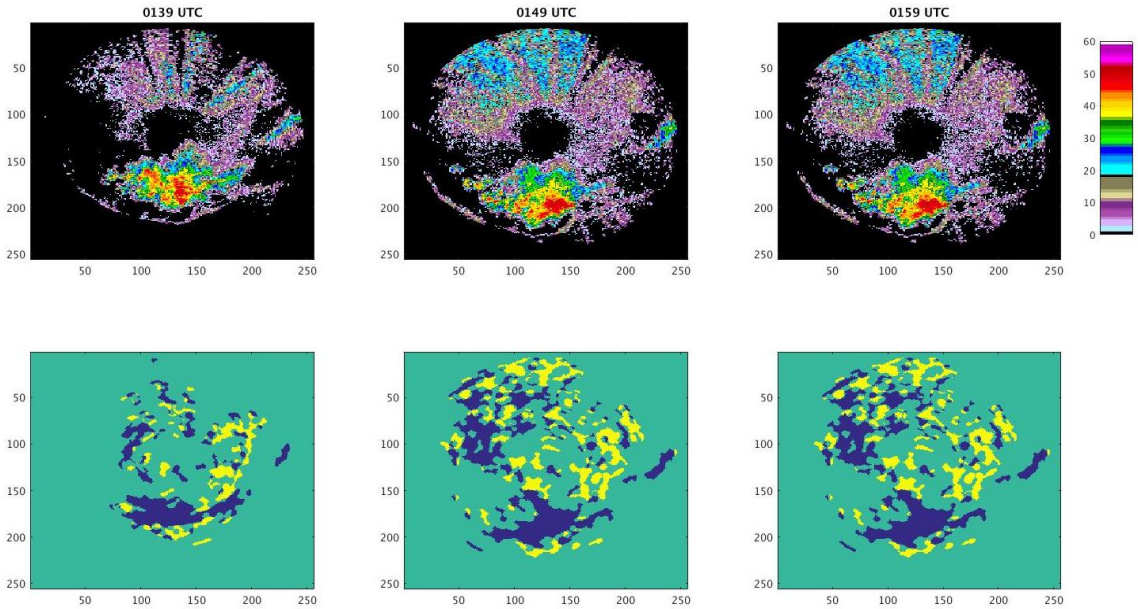

Figure 4.66: KLSX reflectivity and divergence on 2006 07 20 from 0139 to 0159 UTC.

4.2.2 07 September 2012

During the late-afternoon of September 7th, 2012 a line of severe thunderstorms impacted the Saint Louis (KLSX) operating area as a frontal system tracked across the central CONUS. Ahead of the line, unorganized cellular thunderstorms were already active in the area, though were scattered within the unstable region ahead of the line. As the frontal system approached from the north-northwest, outflows from the line and the scattered storms were observed on reflectivity. The outflows eventually collided and "merged", the new outflow boundary then adopting an east-southeast track as it moved ahead of the frontal system. The radar data available for this case was the 01.00 km level for both divergence and reflectivity. Additionally, it is important to note that the reflectivity imagery for this case shows a number of "rings" where the data is obscured on most of the scans. This is likely an artifact from data processing, as it only affects the reflectivity and was unable to be fixed by changing levels or reprocessing the data.

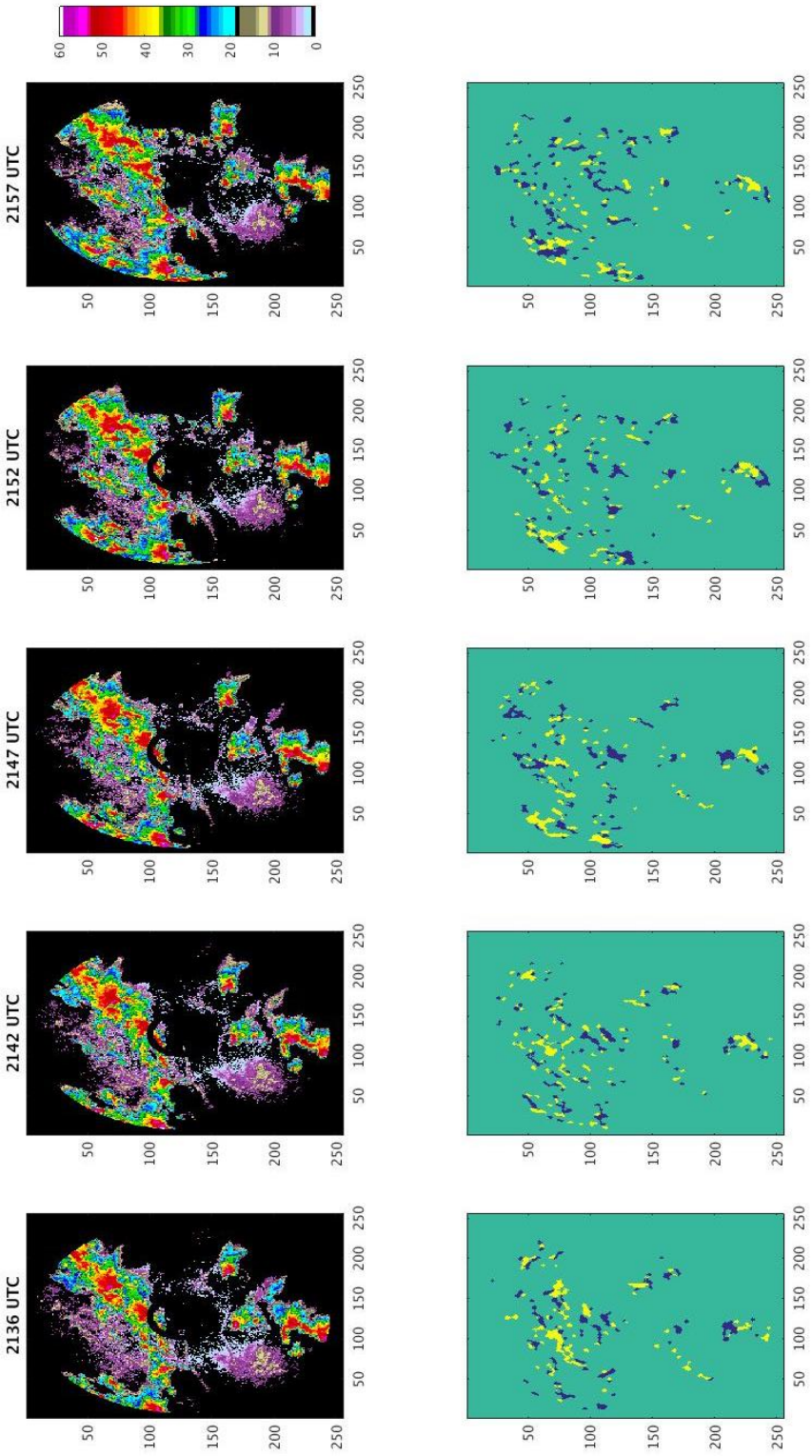

Figure 4.67: KLSX reflectivity and divergence on 2012 09 07 from 2136 to 2157 UTC.

The collision and merger of the two gust fronts occurred during the time period of 2121 UTC to 2209 UTC. While it was possible to track to track this interaction, by user observation, the signals were fairly weak and individual blobs in the line had very small areas which kept the line broken and poorly defined on the divergence field. An example of these gust fronts can be seen in Figure 4.67. What did not help the signal was that that much of the divergence and convergence was like values between both the storms and the thin lines before image processing, leading to noisy images.

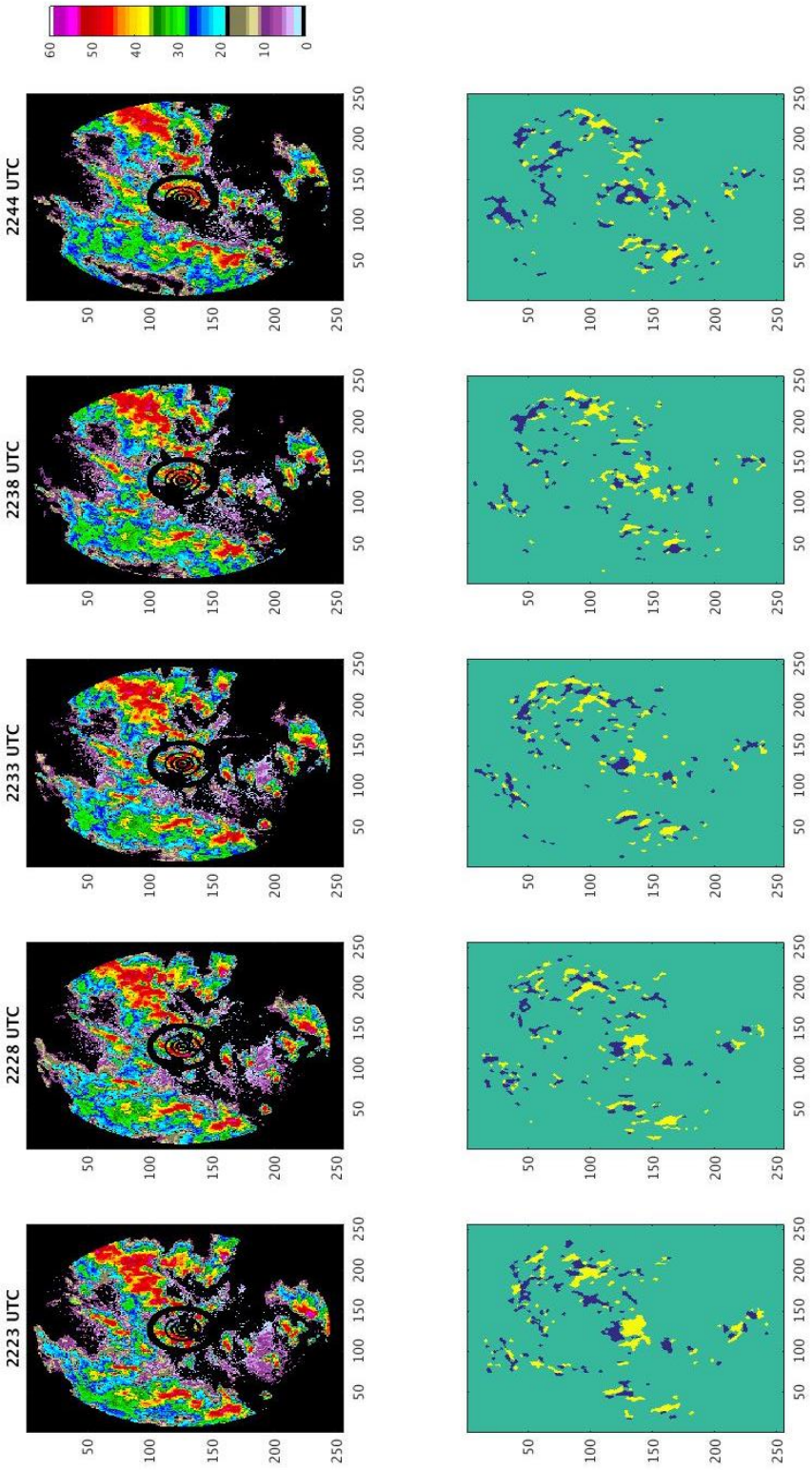

Figure 4.68: KLSX reflectivity and divergence on 2012 09 07 from 2223 to 2244 UTC.

While the noise problem persisted through the rest of the event, tracking the "merged" gust front was less difficult from a user viewpoint. The merged gust front was a more defined feature than the earlier gust fronts. Starting at 2235 UTC the gust front can be seen just south of the radar on divergence and on reflectivity (partly, due to the artifacting), in between the scattered cells and the frontal system (Fig 4.68). The signal on the eastern half due to the proximity of the system and the scattered convection. Over the next several scans the line begins to move to southeast. As it moves, the front enhances some of the scattered convection along its path (Fig 4.69). The shape of the line is fairly defined and consistent over time, despite the scattered composition of CDAs throughout. Sections with larger CDAs are collocated with thunderstorms developing along the gust front, which can be seen in the 2244/2246 UTC scan seen in Figure 4.69. Moving on to the 2250-2300 intervals, the gust front begins to be obscured on reflectivity by the developing convection (Fig 4.69). But, the sections that forced the convection can still be seen in the divergence field, which means that awareness of the feature is not lost on the divergence product. The gust front shifts to the head of the local precipitation as the convection builds into the main line of the system (Fig 4.70). The new gust front then moves east as the storm system moves towards the outer ranges of the KLSX visual range after 2321 UTC.

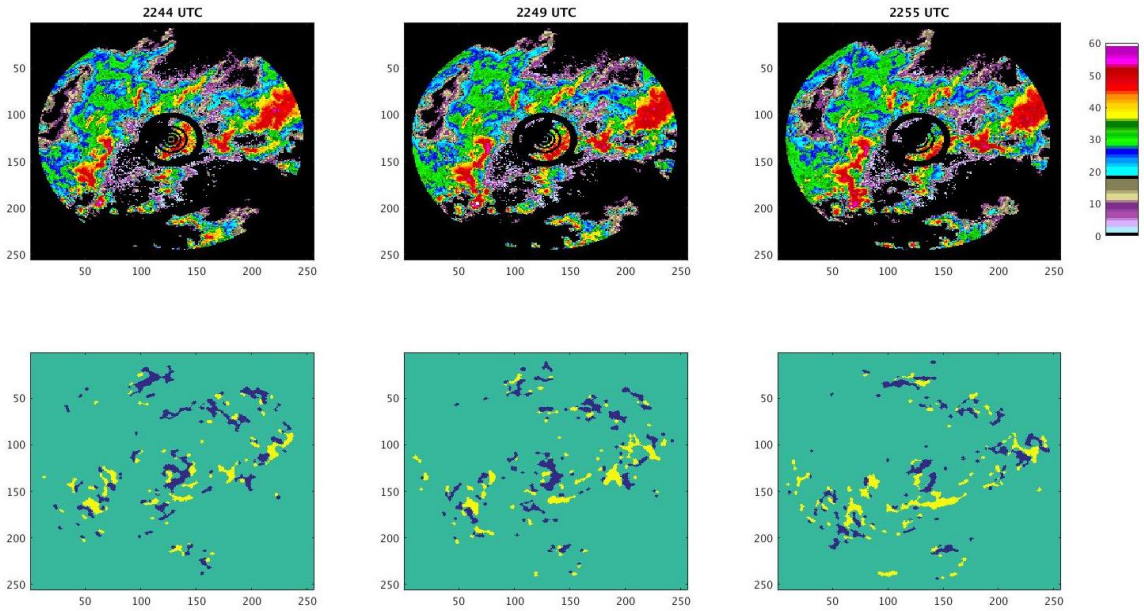

Figure 4.69: KLSX reflectivity and divergence on 2012 09 07 from 2244 to 2255 UTC.

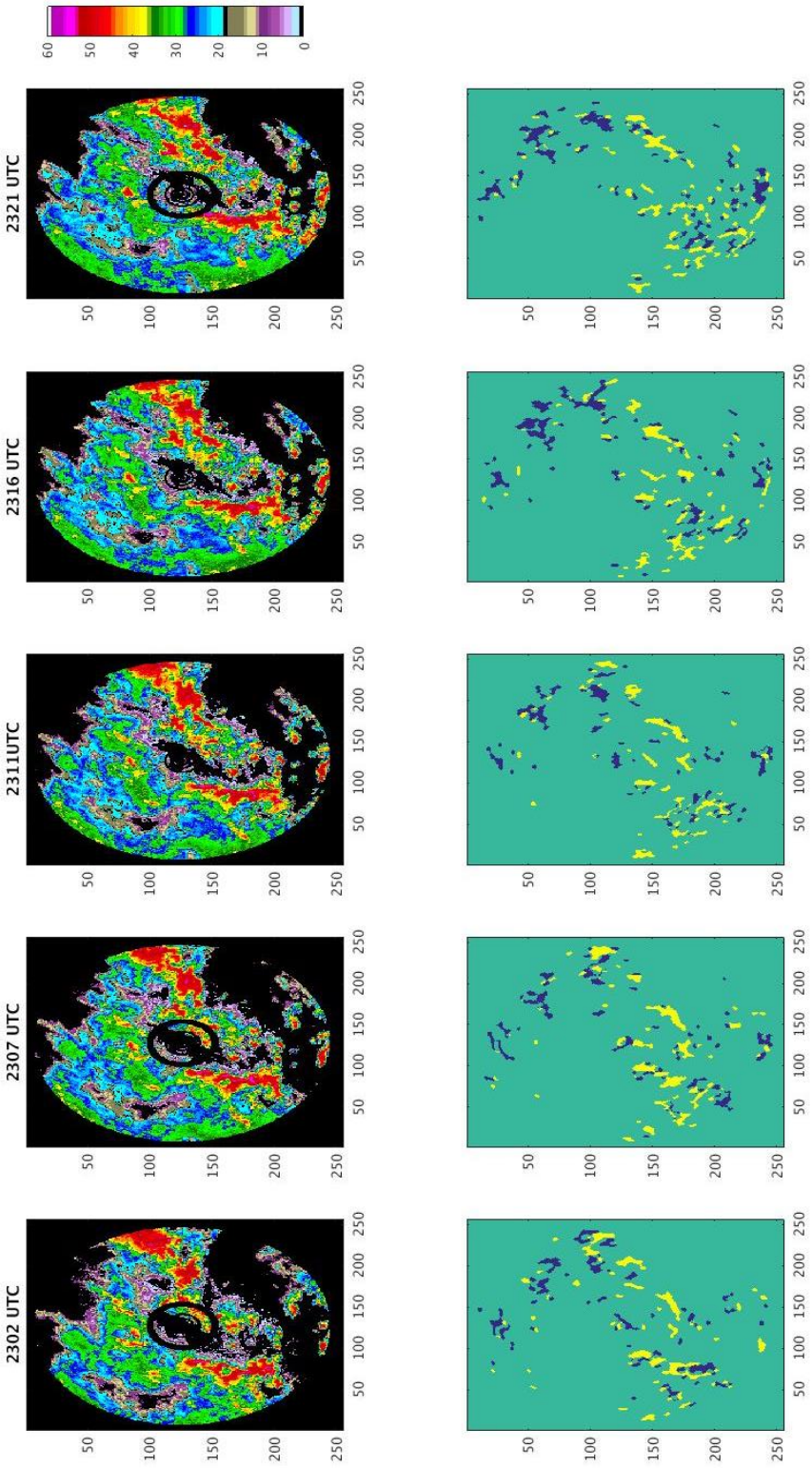

Figure 4.70: KLSX reflectivity and divergence on 2012 09 07 from 2302 to 2321 UTC.

4.2.3 07 March 2017

Following the QLCS crossing MZZU (discussed earlier), the same line of storms moved into the KLSX area during the evening of March 7th, 2017. The storm moved through with the same pace as it did when moving through Columbia earlier in the evening, with the same threat of high winds, heavy rains, and hail. The QLCS still did not produce a visible thin line echo on reflectivity, so the objective was still to find the gust front within the leading edge of the precipitation. The available radar data was the 01.00 km level for both reflectivity and divergence.

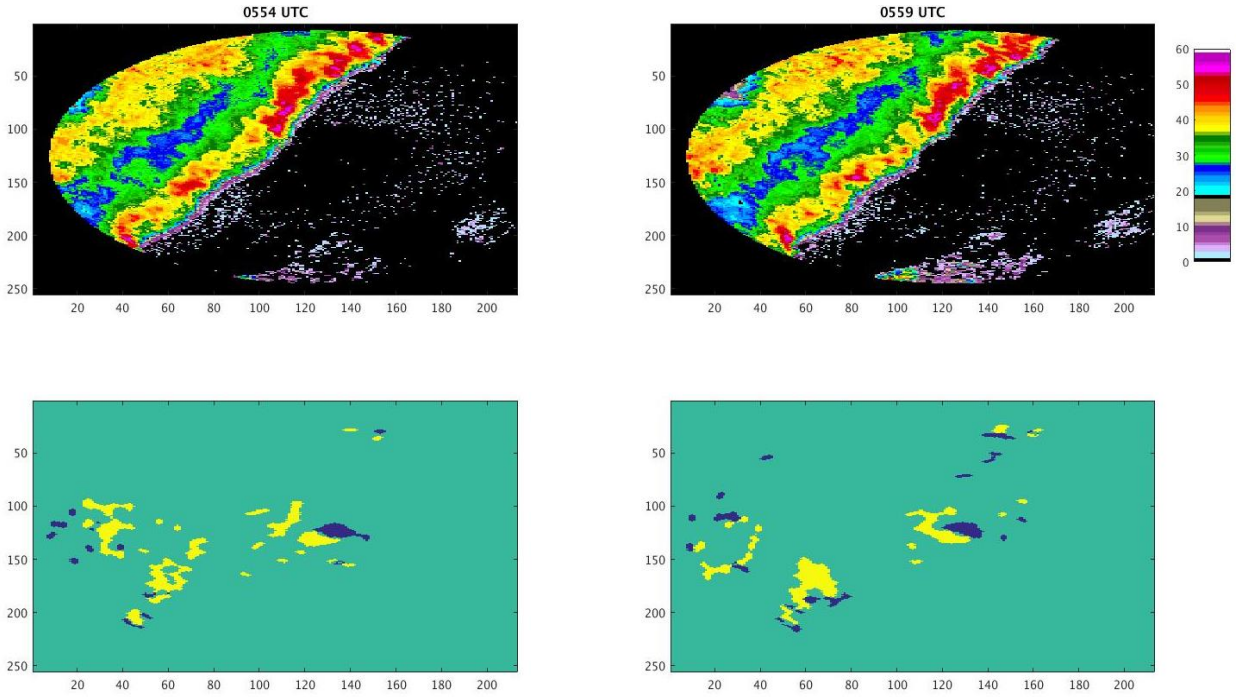

Figure 4.71: KLSX reflectivity and divergence on 2017 03 07 from 0554 to 0559 UTC.

Starting with the 0554 UTC scan as the QLCS closes in on KLSX. The target gust front can be seen on the divergence field as the convergence line at the relative center

of the QLCS with respect to the storm (Fig 4.71). Comparing to the reflectivity at this time it is located on the leading edge as expected of an in-storm gust front. The signature is also consistent with the location of the convergence seen during the MZZU case earlier in the evening. Although, due to the capabilities of the S-Band KLSX and differences in processing, the CDA composing the convergence line is not as large as what was seen during the MZZU time of this case. The CDA does not extend as far into the precipitation as it did on the MZZU imagery.

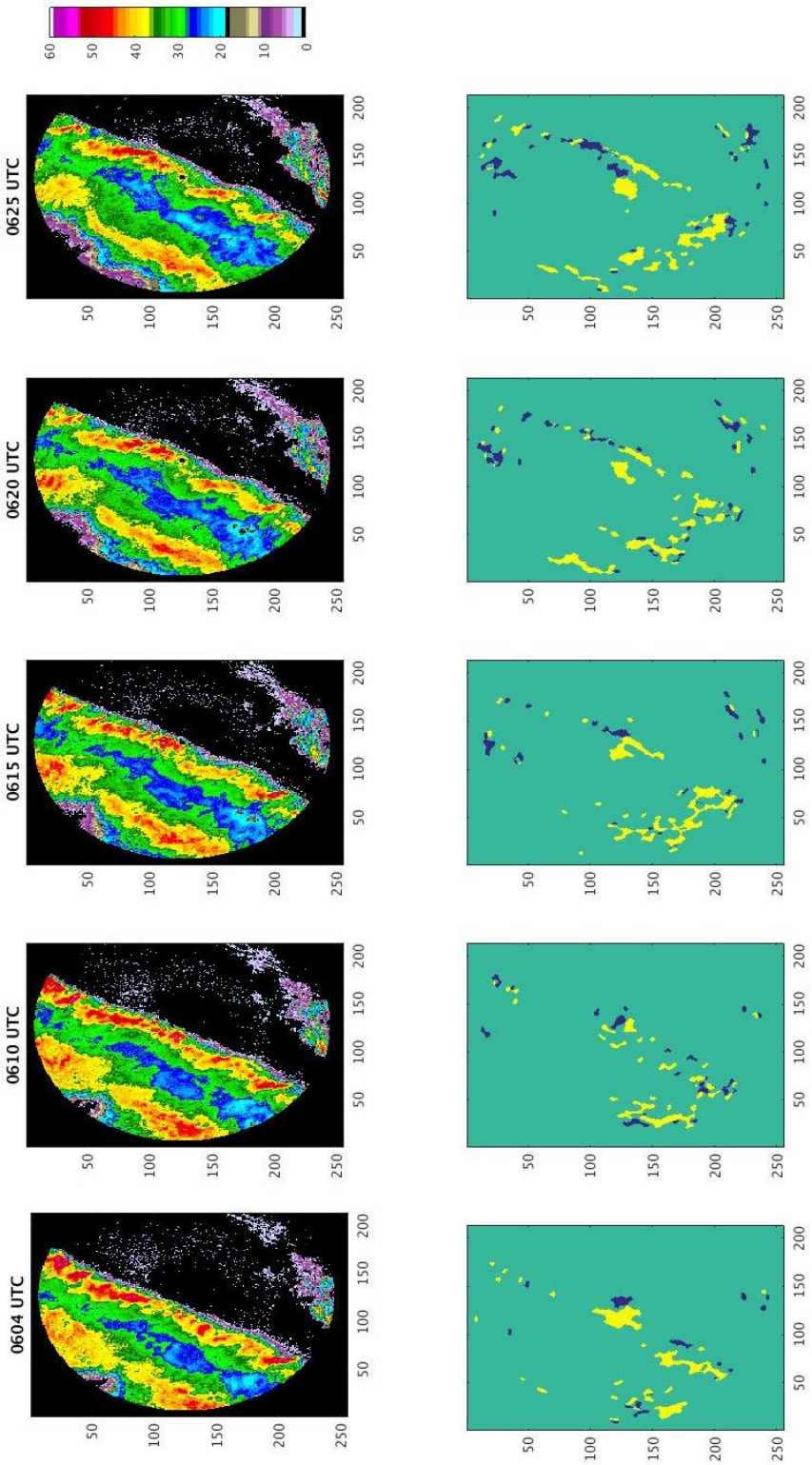

Figure 4.72: KLSX reflectivity and divergence on 2017 03 07 from 0604 to 0625 UTC.

As the storm moves closer to KLSX, the gust front signature interacts with the noisy signal surrounding the radar, obscuring it for several scans (0559 UTC – 0610 UTC). This is especially the case during the 0610 UTC scan (Fig 4.72), where the target line segment disappears, leaving the front to be inferred by the blobs moving parallel to the radial that are to the south-southwest. The signal recovers after crossing out to the eastern side of KLSX on the 0615 UTC scan (Fig 4.72), once again taking the linear convergence shape. As the QLCS moves away to the east-southeast, the gust front (convergence line) at the leading edge stays temporally and spatially consistent during the 0615 – 0620 UTC scans. This can also be seen on Figure 4.72. As the QLCS moves farther from the radar in the KLSX operating range the front retains consistency in shape and position with respect to the reflectivity seen in previous scans. This can be seen in the 0625-0630 scans in Figure 4.73. The last scans covered in this case show that the shape consistency degrades as the front moves into the outer regions of the radar operating area at 0641 UTC (Fig 4.73 and 4.74). While the gust front signature is still fairly well defined, breaks in the line appear more common and becomes noisy, as seen in the 0651 and 0656 UTC scans. The leading edge of the QLCS begins to move out of the observable range of KLSX following the 0656 UTC scan (Fig 4.74).

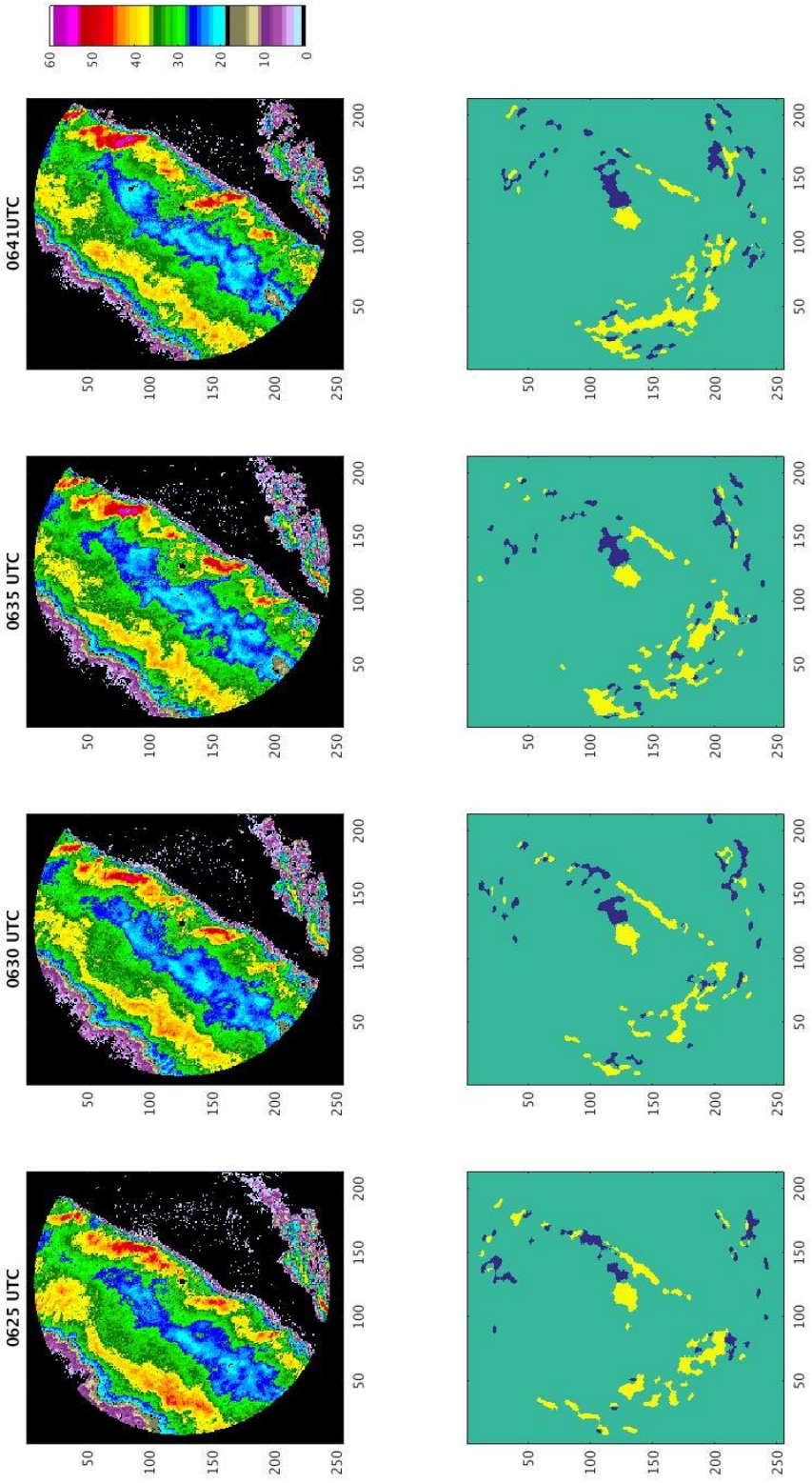

Figure 4.73: KLSX reflectivity and divergence on 2017 03 07 from 0625 to 0641 UTC.

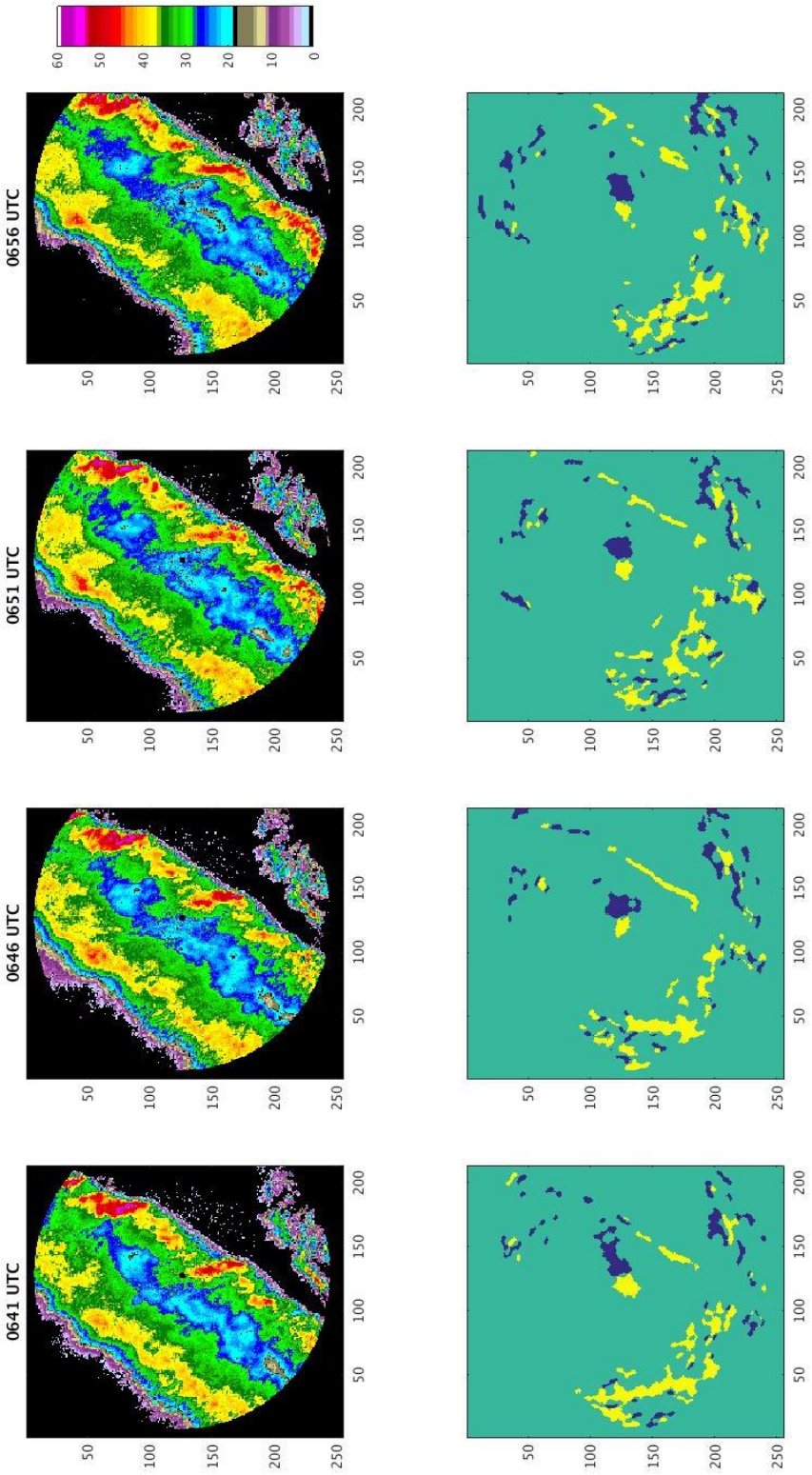

Figure 4.74: KLSX reflectivity and divergence on 2017 03 07 from 0641 to 0656 UTC.

Chapter 5: Conclusion

This study was performed to determine if the WDSS derived divergence product can be used to observe and track gust fronts. Through the twelve cases covered it can be concluded that the radar product can be used in this way. The signatures that can be used to identify and track boundaries, divergence-convergence pairs and convergence lines, were observed in both in-storm and out-of-storm (thin line) gust front cases. These features were generally consistent in time over multiple radar scans as the features tracked, consistent with the minimum of two consecutive scans that was used to evaluate temporal continuity in the automated gust front tracking algorithm seen in Uyeda and Zrnic (1985). Gust front cases in MZZU were compared to vertical velocity data obtained from eddy-covariance sites in the region that were traversed during the events. The vertical velocity data was used to determine if the signatures correlated with an increase in vertical motion expected with a frontal updraft. It was found that local peaks in positive $\overline{w}$ were present when a gust front signature was crossing over during the cases covered, these peaks were followed by an expected decreasing trend as the signatures passed and the sensor was within the turbulent region behind the suspected front. Pairing the divergence and $\overline{w}$ data suggests that the divergence product was in fact detecting gust fronts successfully during most of the cases near MZZU. While this method was successful, it was not consistently clear that a peak in vertical velocity was associated with a gust front. Often being surrounded by other peaks, which sometimes had greater positive $\overline{w}$ or more defined trends, that are likely

caused by diurnal effects or other local turbulence. TKE was used to supplement $\overline{w}$ data by identifying increases of turbulence at the time of suspected gust front passage. TKE helped in clearing up the obscurity, but there was still some uncertainty with daytime events during the summer cases which possibly had turbulence caused by non-thunderstorm sources.

Gust front signatures were trackable over time by user observation, but it was determined that automation was out of reach for this study. This was decided due to the significant amount of left-over noisy signal following image processing. Large numbers of individual blobs make it difficult to single out the target signature(s) that are attributed to the gust fronts. Also, there was uncertainty encountered by the obscuring of gust front signatures by ground clutter, noise, and attenuation. These sources of uncertainty were expected going in to the analysis, as these were problems that did not have a correction that could be implemented prior to study, as the causes for these problems exist naturally (especially in the case of ground clutter). The erosion-dilation scheme is used to mitigate this, but it was only partially successful. One possible solution would be to filter radar data using a ρhv threshold.

Three parameter sets were developed to generate gust front signatures as seen in chapter 4.1, two for MZZU and one for use with KLSX (S-Band radar). These settings were overall very capable in resolving gust front signatures during the cases covered in this study, but the troubles with weaker thin line cases highlighted a major source of uncertainty. Thin line (out-of-storm) gust fronts were subject to breaks in their signatures or signal loss, believed to at least partially be caused by filtering systems

within the WDSS processing tools. The thresholds remove signatures on reflectivity below 10dBZ, which removes the lower reflectivity bounds for gust fronts, which then removes signal on the divergence field. This error could potentially be corrected by adjusting the display thresholds within the WDSS processing. However, since the purpose of these thresholds is to filter out "non-weather" targets (Lakshmanan et al., 2006), adjustment could also mean adding more noise to the already noisy divergence field. As mentioned, thresholds within WDSS could not be adjusted during this study, so the practicality of this change is unknown.

Another prominent, but expected, source of uncertainty encountered during this study was the changing or loss of gust front signatures due to the boundaries moving parallel to the radar radial. A possible solution to this uncertainty is to include azimuthal shear (rotation) similar to the concept seen in Smith and Elmore (2004), from Figure 3.6. The rotational product works better at resolving boundary signatures that move parallel to the radial than the divergence, so using the two products together would make observing the whole length of gust fronts easier than using divergence alone.

While this study did conclude that the divergence product can be used to detect gust fronts, this study could be refined or expanded on with future work. While the parameter sets were effective in generating gust front signatures in generalized situations (out of storm, in-storm, S-Band use), there is still potential to refine the parameters. As mentioned above, additional steps could be implemented into image processing to filter out more unwanted signals and cut down on noise. In theory, cleaning up the image further would also make it easier to implement into automated

methods such as centroid based nowcasting, since it would be easier to single out the target in the data. Also, if determined to be practical, more specialized parameters could be developed to account of convective mode, or other radar types beyond X-band (MZZU) and S-Band (KLSX). Lastly, using instruments that are purpose built for measuring vertical velocities would likely aid in observing the $\overline{w}$ trends more clearly and better correlate with the radar data.

Appendix

MatLab Code used to Analyze Reflectivity and Divergence Data

This code was designed to read in radar data from archive directories as input for image processing, where Divergence data was processed to look for gust front signatures.

```
areathreshold=4;
dilation=4;
erosion=3;
divthresh1= 0.00075;
divthresh2= 0.002;
convthresh1=-0.00075;
convthresh2=-0.004;
%divthresh=0.0002;
%convthresh=-0.0002;
%divthresh=20;
%convthresh=-0.002;

dz=dir('/usr/local/wdss/20170301/netcdf/ReflectivityAtLowestAltitude
/00.00/20060720-01*.netcdf');
pathz={dz.name};
pathhead='/usr/local/wdss/20170301/netcdf/ReflectivityAtLowestAltitu
de/00.00/';

dd=dir('/usr/local/wdss/Brewster/netcdf/DivergenceAtLowestAltitude/0
1.00/20060720-01*.netcdf');
pathd={dd.name};
pathhead2='/usr/local/wdss/20170301/netcdf/DivergenceAtLowestAltitud
e/01.00/';

  a=0;

for b=4:6
  pathz2=strcat(pathhead,pathz);
  pathd2=strcat(pathhead2,pathd);
load('/home/students/clemins/Desktop/Colormaps/Reflectivity.mat');
  clin = [-32,75];
  units = 'dBZ';
  zmap = cmap;
  a=a+1;

% redo for convergence (same subplot)
%structure to store cellprops
ncid = netcdf.open(pathz2{b},'NC_NOWRITE');
[varname, xtype, varDimIDs, varAtts] = netcdf.inqVar(ncid,0);
varid = netcdf.inqVarID(ncid,varname);
z=netcdf.getVar(ncid,varid);
z=z';

ncid = netcdf.open(pathd2{b},'NC_NOWRITE');
[varname, xtype, varDimIDs, varAtts] = netcdf.inqVar(ncid,0);
varid = netcdf.inqVarID(ncid,varname);
div=netcdf.getVar(ncid,varid);
```

```
div=div';

[m n]=size(div);
for i=1:m
    for j=1:n
        if (z(i,j)<=-10)
            z(i,j)=0;
        end
    end
end

for i=1:m
    for j=1:n
        if (div(i,j)<=-10)
            div(i,j)=0;
        end
    end
end

%figure

ax1=subplot(2,3,a);
imagesc(z),

colormap(ax1,zmap),
caxis([0 60]),

dcell=div>divthresh1 & div<divthresh2;
%subplot(222),imagesc(dcell)
%hold
cellprop = regionprops(dcell,'Area','Centroid',...

'Eccentricity','MajorAxisLength','MinorAxisLength',...
                        'Orientation');
dcell2 = bwlabel(dcell);
cellprop = struct2table(cellprop);
I = find(cellprop.Area>=areathreshold);
newBW = zeros(size(dcell2));
    for z = 1:length(I)
            temp = dcell2==I(z);
            newBW(temp) = 1;
    end
dcell3 = logical(newBW);
    SE = strel('disk',dilation,0);
    dcell3 = imdilate(logical(newBW),SE);
%subplot(223),imagesc(dcell3)
%hold
dcell4 = dcell3;
    SE = strel('disk',erosion,0);
    dcell4 = imerode(dcell4,SE);
%subplot(224),imagesc(dcell4)
%hold
cellprop2 = regionprops(dcell4,'Area','Centroid',...
```

```
'Eccentricity','MajorAxisLength','MinorAxisLength',...
                        'Orientation');


ccell=div<convthresh1 & div>convthresh2;
subplot(222),imagesc(ccell-dcell)
cellprop3 = regionprops(ccell,'Area','Centroid',...

'Eccentricity','MajorAxisLength','MinorAxisLength',...
                        'Orientation');
ccell2 = bwlabel(ccell);
cellprop3 = struct2table(cellprop3);
K = find(cellprop3.Area>=areathreshold);
newWB = zeros(size(ccell2));
    for z = 1:length(K)
            temp = ccell2==K(z);
            newWB(temp) = 1;
    end
ccell3 = logical(newWB);
    SE2 = strel('disk',dilation,0);
    ccell3 = imdilate(logical(newWB),SE2);
subplot(223),imagesc(ccell3-dcell3)
ccell4 = ccell3;
    SE2 = strel('disk',erosion,0);
    ccell4 = imerode(ccell4,SE2);
ax2=subplot(2,3,a+3);
imagesc(ccell4-dcell4),colormap(ax2,parula)
cellprop4 = regionprops(ccell4,'Area','Centroid',...

'Eccentricity','MajorAxisLength','MinorAxisLength',...
                        'Orientation');
end
```

References

American Meteorolocial Society, cited 2018: Gust Front. Glossary of Meteorology. [Available online at: http://glossary.ametsoc.org/wiki/Gust_front].

Campbell Scientific, Inc., 2017: CSAT3 three-dimensional sonic anemometer instruction manual. pp 74. [Available online at: https://s.campbellsci.com/documents/us/manuals/csat3.pdf].

Campbell Scientific, Inc., 2017: IGRASON integrated CO2 / H20 open-path gas analyzer and 3d sonic anemometer instruction manual. pp 80. [Available online at: https://s.campbellsci.com/documents/us/manuals/irgason.pdf].

Charba, J., 1974: Application of Gravity Current Model to Analysis of Squall-Line Gust Front. *Mon. Wea. Rev.*, **102**, 140-156.

Frank J. M., W. J. Massman, and B. E. Ewers, 2013: Underestimates of Sensible Heat Flux Due to Vertical Velocity Measurement Errors in Non-orthogonal Sonic Anemometers. *Agricultural and Forest Meteorology*. **171-172**, 72-81.

Frasier S. J., F. Kabeche, J. F. I. Ventura, H. Al-Sakka, P. Tabary, J. Beck, and O. Bousquet, 2013: In-Place Estimation of Wet Radome Attenuation at X Band. *J. Atmos. Oceanic Technol.*, **30**, 917-928.

Goff, R. C., 1976: Vertical Structure of Thunderstorm Outflows. *Mon. Wea. Rev.*, **104**, 1429-1440.

Hwang Y., T. Yu, V. Lakshmanan, D. M. Kingfield, D. Lee, and C. You, 2017: Neuro-Fuzzy Gust Front Detection Algorithm With S-Band Polarimetric Radar. *IEEE Trans. Geosci. Remote Sens*., **vol. 55**, **no. 3**, 1618-1628.

Jarvi L., A. J. Punkka, D. M. Schultz, T. Petaja, H. Hohti, J. Rinne, T. Pohja, M. Kulmala, P. Hari, T. Vesala, 2007: Micrometeorological Observations of a Microburst in Southern Finland. *Bound.-Layer Meteor.*, **125**, 343-359.

Klingle D. L., D. R. Smith, and M. M. Wolfson, 1987: Gust Front Characteristics as Detected by Doppler Radar. *Mon. Wea. Rev.*, 115, 905-918.

Kochendorfer J., T. P. Meyers, J. Frank, W. J. Massman, M. W. Heuer, 2012: How Well Can We Measure the Vertical Wind Speed? Implications for Fluxes of Energy and Mass. *Bound.-Layer Meteor.*, **145**, 383-398.

Lack S., and N. Fox, 2012: Development of an Automated Approach for Identifying Convective Storm Type Using Reflectivity-Derived and Near Storm Environment Data. *Atmospheric Research*, **116**, 67-81.

Lakshmanan V., T. Smith, K. Hondl, G. J. Stumpf, and A. Witt, 2006: A Real-Time, Three-Dimensional, Rapidly Updating, Heterogeneous Radar Merger Technique for Reflectivity, Velocity, and Derived Products. *Wea. Forecasting*, **21**, 802-823.

--, T. Smith, G. Stumpf, and K. Hondl, 2007: The Warning Decision Support System-Integrated Information. *Wea. Forecasting*, **22**, 596-612.

Micheas, A., N.I. Fox, S.A. Lack and C.K. Wikle, 2007: Cell Identification and Verification of QPF Ensembles Using Shape Analysis Techniques. *Journal of Hydrology*, **344,** 105-116.

Mauder M., S. P. Oncley, R. Vogt, T. Weidinger, L. Ribeiro, C. Bernhofer, T. Foken, W. Kohsiek, H. A. R. De Bruin, H. Liu, 2007: The Energy Balance Experiment EBEX-2000. Part II: Intercomparison of Eddy-Covariance Sensors and Post-Field Data Processing Methods. *Bound.-Layer Meteor.*, **123**, 29-54.

Purdom J. F. W., 1976: Some Uses of High-Resolution GOES Imagery in the Mesoscale Forecasting of Convection and its Behavior. *Mon. Wea. Rev.*, **104**, 1474- 1483.

Ray P. S., 1976: Vorticity and Divergence Fields within Tornadic Storms from Dual-Doppler Observations. *J. Appl. Meteor.*, **15**, 879-890.

Rinehart R. E., 2010: Radar for Meteorologists. 5th ed. Rinehart, 482 pp.

Roberts R., and S. Rutledge, 2003: Nowcasting Storm Initiation and Growth Using GOES-8 and WSR-88D Data. *Wea. Forecasting*, **18**, 562 -584.

Sills, D., J. Wilson, P. Joe, D. Burgess, R. Webb and N.I. Fox, 2004: The 3 November tornadic event during S2000: Storm evolution and the role of low-level boundaries. *Wea. Forecasting,* **19 (1),** 22-42.

Schreiber W. E., 1986: Notes and Correspondence Case Studies of Thunderstorms Initiated by Radar-Observed Convergence Lines. *Mon. Wea. Rev.*, **114**, 2256-2266.

Smith T. M., and K. L. Elmore, 2004: The Use of Radial Velocity Derivative to Diagnose Rotation and Divergence. Preprints, *11th Conf. on Aviation, Range, and Aerospace*, Hyannis, MA. Amer. Meteor. Soc., CD-ROM, P5.6.

Uyeda H., and D. S. Zrnic, 1986: Automatic Detection of Gust Fronts. *J. Atmos. Oceanic Technol.*, **3**, 36-50.

Wakimoto R. M., 1982: The Life Cycle of Thunderstorm Gust Fronts as Viewed with Doppler Radar and Rawinsonde Data. *Mon. Wea. Rev.*, **110**, 1060-1082.

Weaver J. F., and S. P. Nelson, 1982: Multiscale Aspects of Thunderstorm Gust Fronts and Their Effects on Subsequent Storm Development. *Mon. Wea. Rev.*, **110**, 707-7118.

Wilson J., R. Carbone, H. Baynton, and R. Serafin, 1980: Operational Application of Meteorological Doppler Radar. *Bull. Am. Meteorol. Soc.*, vol. **61**, 1154-1168.

Wilson J. W., and W. E. Schreiber, 1986: Initiation of Convective Storms at Radar-Observed Boundary-Layer Convergence Lines. *Mon. Wea. Rev.*, **114**, 2516-2536.

--, and C. K. Mueller, 1993: Nowcasts of Thunderstorm Initiation and Evolution. *Wea. Forecasting*, **8**, 113-131.

--, T. M. Weckwerth, J. Vivekanandan, R. M. Wakimoto, and R. W. Russell, 1994: Boundary Layer Clear-Air Radar Echoes: Origin of Echoes and Accuracy of Derived Winds. *J. Atmos. Oceanic Technol.*, **11**, 1184-1206.

--, and D. L. Megenhardt, 1997: Thunderstorm Initiation, Organization, and Lifetime Associated with Florida Boundary Layer Convergence Lines. *Mon. Wea. Rev.*, **125**, 1507-1525